City Research Online

City, University of London Institutional Repository

COMPUTATIONAL MODELING OF CAVITATION-TISSUE INTERACTIONS

*Thesis submitted for the fulfillment of the requirements
for the Degree of Doctor of Philosophy*

by

Evangelos Koukas

CITY, UNIVERSITY OF LONDON

School of Mathematics, Computer Science Engineering

Department of Mechanical Engineering Aeronautics

February 2024

To my family, friends, and loved ones.

Acknowledgements

I am profoundly grateful for all the support and encouragement I have received throughout the course of my doctoral studies.

I extend my heartfelt gratitude to my supervisor, Prof Manolis Gavaises, whose unwavering faith in me and my work significantly shaped this journey. He not only provided me with the chance to embark on this fascinating research but also skillfully steered the direction of my project toward groundbreaking applications. Under his insightful leadership, I was privileged to engage in stimulating scientific endeavors and push my boundaries in novel settings.

Additionally, my sincere appreciation goes to Dr. Andreas Papoutsakis for his invaluable assistance throughout the development of my solver. His extensive knowledge in Computational Fluid Dynamics (CFD) consistently provided me with insightful feedback on the evolution of my work. Our collaboration blossomed into a life-long friendship.

I must also express my gratitude to my colleagues and friends in the A306 office. Their companionship and shared moments of joy greatly enhanced the enjoyment of my PhD journey, creating memories I will always treasure.

Lastly, I extend my deepest gratitude to my parents for their unwavering support throughout this journey. A special mention to my brother, whose support over these years has been invaluable.

Evangelos Koukas,
London, February 2024

Abstract

The present thesis introduces a novel numerical framework for the study of bubble-tissue interactions, crucial for understanding the mechanics behind tissue-induced damage in medical therapies where cavitation is apparent, such as shock-wave lithotripsy, high-intensity focused ultrasound, and needle-free injections. To tackle these scenarios, we have developed solver employs the 6-equation required by the Diffuse Interface Method (DIM), with its extension for isotropic elastic solids, accounting for the interaction across fluid-solid-gas interfaces, able to accurately resolve bubble dynamics, shock wave propagation, large solid deformations and dynamic appearance of cavitation regions. For the resolution of the extended variety of length scales, due to the dynamic and fine interfacial structures, an Adaptive Mesh Refinement (AMR) framework for unstructured grids was incorporated. This multi-material multi-scale approach aims to reduce numerical diffusion and preserve sharp interfaces, providing a novel computational approach for accurately capturing the complex dynamics of bubble collapse near biological tissues and the ensuing interactions. Due to the inertial nature of the bubble collapse dynamics surface tension, mass transfer, phase change, visco-elastic, and strain-stiffening effects are neglected.

The primary findings of this work include the elucidation of a previously undocumented tension-driven tissue injury mechanism during shock-wave lithotripsy, offering insights into the secondary collapse phase of gas bubbles near soft tissues and their potential for tissue damage. The gas bubble collapse dynamics near soft tissues are discussed in detail, including the shock wave emissions, liquid jet formation, and secondary collapses. Additionally, a comprehensive parametric study elucidates the influence of various factors on bubble behavior and tissue interaction, offering valuable insights into the various parameters affecting the bubble dynamics, during shock wave lithotripsy. Finally, the investigation into needle-free jet injectors demonstrates the framework's capability to simulate liquid-jet and skin interactions, highlighting its potential use to investigate the penetration depth and drag delivery for various skin types.

This work significantly advances the computational modeling of bubble dynamics in medical applications, providing a robust tool for the development and optimization of ultrasound-based therapies and devices.

Present Contribution

The innovative aspects and significant contributions of this thesis are encapsulated in the following key points:

- **Synergizing Adaptive Mesh Refinement and Multi-Material Diffuse Interface Model for Multiscale Fluid-Structure Interaction simulations**

  This work introduces a novel computational framework that synergises Adaptive Mesh Refinement (AMR) with a multi-material Diffuse Interface Model for fluid-structure interaction (FSI), shock capturing, and accurate bubble dynamics. Utilizing a dynamic AMR strategy, for unstructured grids, the framework permits on-the-fly grid refinement to an arbitrary level of self-similar cells, leveraging a tree data structure with linked lists of pointers for seamless mesh manipulation including splitting, merging, and repartitioning. This enables efficient handling of the required resolution to capture the diverse spatial scales inherent in compressible, dispersed, multiphase flows, using higher computational resources on areas of intricate flow structures for enhanced local resolution. The specific implementation of the Diffuse Interface Model is derived from the 7-equation model of Baer and Nunziato [7] by assuming kinematic equilibrium, thus reaching the 6-equation model. The mechanical equilibrium is imposed explicitly by a relaxation procedure. Furthermore, the 6-equation model of Saurel et al. [148] was extended to account for Fluid-Structure Interaction (FSI) [44]. The mechanical properties of the solid continuum are integrated by incorporating 9 additional equations for the deformation Jacobian matrix. The deformation matrix is used for the evaluation of the full three-dimensional stress tensor for the solid. The Equation of State (EoS) for the solid and liquid materials is also extended with the addition of the elastic energy.

- **A numerical study of bubble-tissue interaction unveiling a mechanism for tissue injury during shock-wave lithotripsy.**

  The shock-induced collapse of gas bubbles close to soft tissue was investigated, for three different configurations. The obtained results reveal the detailed collapse dynamics, jet formation, solid deformation, rebound, primary and secondary shock wave emissions, and secondary collapse that govern the near-solid collapse and penetration mechanisms. Significant correlations of the problem configuration to the overall collapse mechanisms were found, stemming from the contact angle/attachment of the bubble and from the properties of solid material. The tissue penetration is examined for these cases and a tension-driven tissue damage mechanism is proposed, derived by from the complex

interaction of the bubble/tissue interaction during the secondary collapse phase of an entrapped bubble in an induced crevice with the liquid jet.

- **An extended study of various parameters on bubble collapse dynamics near bio-materials.**

  Following the previous study, a wider range of configurations were examined. The parametric studies conducted reveal the influence of various factors, on the bubble dynamics including the stand-off distance and attachment to the solid boundary, the initial size of bubble nuclei, and the characteristics of the lithotripter's pulse. This research significantly advances our knowledge in the field, particularly in lithotripsy, by providing a deeper insight into the behavior and effects of shock-induced bubble collapse near bio-materials.

- **The first numerical study of needle-free jet injectors coupled with jet-skin fluid-solid interaction.**

  Needle-free jet injectors were simulated, to elucidate the liquid-jet skin interactions. Validation cases were presented and the formation of the liquid-jet was presented. Following several types of skin-type solids were examined. This type of study has not been documented in the existing literature before.

Declaration

I hereby declare that the content of this dissertation is original and has not been submitted in whole or in part for consideration for any other degree or qualification in this, or any other university. This dissertation is my own work, except where specific reference is made to a joint effort in the text and acknowledged accordingly.

I grant powers of discretion to the University Librarian to allow the thesis to be copied in whole or in part without further reference to me. This permission covers only single copies made for study purposes, subject to normal conditions of acknowledgment.

Evangelos Koukas,
London, February 2023

TABLE OF CONTENTS

List of Figures

x

xiii

List of Tables

1 Introduction

This chapter offers an overview of the scientific background and the motivation behind this thesis. It also delineates the aims of this research and provides a structured summary of the thesis.

1.1 Background and Motivation

Cavitation represents a significant challenge in physics, intersecting numerous engineering and scientific disciplines. The first mention of the phenomenon dates back to 1885 when during sea trials of HMS Daring, vapour bubbles were observed in the water, at high propeller speeds, followed by erosion and pitting in the propeller blades [22]. Later in 1917, Lord Rayleigh was the first to produce a simplified explanation of the mechanism by which bubbles oscillate, collapse and produce the subsequent high-pressure shock wave [142]. In general, cavitation is the phenomenon in which low hydrostatic pressure leads to the rapid growth and collapse of a void or bubble within a liquid or solid. This phenomenon is widely observed in numerous engineering applications, from the automotive industry, in internal combustion engines, to naval engineering for propeller design, the energy sector in turbines and pumps, and the biomedical field from procedures like lithotripsy to drug delivery [184]

Cavitation can manifest in biological systems under a broad spectrum of conditions, including ultrasound treatments, abrupt impacts from accidents or head injuries, shock wave propagation in medical interventions, or alterations in pressure [53, 3, 11]. In specific medical contexts [153, 84], stable or inertial cavitation is harnessed for therapeutic objectives, deliberately induced under regulated circumstances.

Stable cavitation is characterized by sustained small amplitude oscillations of the bubble about its equilibrium. The bubble's oscillations radiate pressure to the surrounding fluid, which generates flow around the bubble termed microstreaming [5]. Conversely, inertial cavitation is generally a transient phenomenon marked by the rapid collapse of a bubble, which can generate shock waves, induce high-velocity liquid jetting, and lead to the erosion of materials [137].

Thus, exploring cavitation in biological flows is crucial for improving and innovating medical procedures, including drug delivery systems and therapeutic strategies. By precisely controlling cavitation, new treatment methodologies can be developed. This investigation into

cavitation dynamics paves the way for breakthroughs in medical technology, providing novel approaches to tackle some health conditions.

Ultrasound imaging has become a widely used diagnostic tool in modern medicine, driven by the need to enhance image clarity. This necessity fostered the development of contrast agents, which have been integrated into routine diagnostic practices to augment image quality. Initial explorations into the utility of contrast agents for ultrasound diagnostics highlighted the potential of gas-bubble-based agents for superior imaging outcomes, as reported by Ziskin et al. [108]. These agents are administered intravenously to enhance the distinction between blood flow and surrounding tissues during ultrasound scans, thereby elevating the diagnostic accuracy and image resolution through the mechanism of cavitation, which produces distinct, bright echoes [157]. Further research has shown that bubble-based contrast agents not only intensify cavitation effects during ultrasound exposure but also raise questions about the potential bio-effects of cavitation on soft tissues, despite the detection of both stable and inertial cavitation with the use of these agents in clinical settings.

Cavitation in artificial heart valves has garnered significant attention and scrutiny and has been a problem that only became evident after widespread installation [172]. In vitro studies have visualized the formation and collapse of bubbles at mechanical heart valves [135]. While damage to the valve due to cavitation is problematic, the main concerns are the cavitation-induced rupture of red blood cells (hemolysis) and the risk of thromboembolic complications. Contributing factors to cavitation are the squeeze flow through the valve and the water hammer phenomenon [22]. Finally, the presence of nuclei in the blood flow coupled with the valve design and the flow conditions have a synergetic effect in inducing cavitation [136].

Extracorporeal Shock-Wave Lithotripsy (ESWL), is a widely used medical treatment for kidney and gall stones disease. Cavitation in this procedure plays a pivotal role, as a contributing factor in the comminution of stones and as a side effect by damaging the surrounding tissue. Kidney stone formation is common, with a lifetime risk of 12% for men and 6% for women [35]. For kidney stones larger than $5mm$, surgical intervention is considered the best treatment option [109], rendering ESWL the sole non-invasive surgical technique available.

Lithotripsy treatment pulverizes kidney stones by generating a number of high-intensity pressure waves with a maximum peak amplitude of $30 - 110\ MPa$ and a minimum of -5 to $-15\ MPa$. Although the exact mechanism of stone fragmentation remains unclear, two main mechanisms have been recognized [146].

The first lies in the shock impact to the stone, which initiates longitudinal P waves and

shear S waves to propagate within its structure, while also generating surface waves at the stone's edge. This wave superposition leads the stress beyond the material's yield point, thereby initiating internal fractures [180, 179]. The stone is also subjected to dynamic stress and fatigue due to the repetitive nature of the shocks, which occur from the continuous tension cycles.

The second mechanism contributing to the stone's disintegration is the erosion of the stone's exterior caused by inertial cavitation [129, 66, 190]. The tensile part of the generated waveform induces cavitation, at the interface of the surrounding liquid and the kidney stone [51]. The high-velocity jets and shock wave emissions produced by the collapsing bubbles create a pitting surface and crack formations that assist in the pulverization of the kidney stone [129]. The fragments resulting from cavitation damage tend to be small, as it is caused by the intense localized stress from collapsing bubbles.

While ESWL is a successful treatment method, it is not uncommon for patients to experience some level of renal injury, with the potential for severe tissue damage [49]. The causes of tissue injury during ESWL can be traced back to two primary factors. The first one is due to the shear stresses produced by the compressible wave interaction with the tissue in the pre-focal region [42]. The second one is due to cavitating bubbles that either form after the passage of the tensile part of the lithotripter shock, or pre-exist as gas nuclei and can lead to blood vessel dilation and even rapture [46, 186].

Furthermore, it has been suggested that inertial cavitation inside blood vessels can be responsible for hemorrhage [177, 81]. In the work of Chen et al. [27] high-speed images show that bubble collapse can lead to vessel invagination, in ex vivo rat mesenteries. The work of Zhou et al. [189] first suggested that the expansion of intraluminal bubbles might lead to the disruption of capillaries and minor blood vessels during ESWL, particularly when nuclei are incorporated into the bloodstream. The experimental study of Liu et al. [100] in cavitation bubbles inside vessel models, further revealed the intricate dynamics of blood vessel potential damage by ultrasound-induced cavitation bubbles. Experimental studies [96] have repeatedly shown the adverse effect of cavitation in ESWL, however, the exact mechanism of vessel rapture and tissue injury still remains unknown [27]. Thus, the present thesis aims to investigate cavitation-induced tissue injury and "further understanding of the precise mechanism of bubble action in SWL" [9].

High-intensity ultrasound treatments such as High Intensity Focused Ultrasound (HIFU) and histotripsy are two non-invasive medical modalities, that leverage cavitation phenomena

[6]. Their ability to precisely destruct a volume of tissue is utilized in clinical applications such as prostate cancer, essential tremor disorder, and treatment of pain from bone cancer metastasis to name a few [133, 17, 23, 105]. HIFU can be used to thermally ablate tissue, through acoustic energy absorption, however, cavitation may appear in the focal region which impacts the treatment by shifting the focal region towards the source of the ultrasound i.e. the piezoelectric transducer [34]. The pre-existence of bubbles can also enhance the absorption of acoustic energy and thus improve the overall efficiency of the treatment [43].

Histotripsy relies on cavitation to mechanically fractionate tissue into a liquid-appearing homogenate with no cellular structure [170]. The 'shock scattering mechanism' or the 'intrinsic threshold mechanism' are two techniques that generate a bubble cloud in the focal region [97]. The former, utilizes a multi-cycle pulse and the scattering of the positive wave from the initial bubbles, whereas the latter uses only one pulse with a tensile phase. [6, 169, 106]. The rapid expansion of these bubbles results in substantial stresses and strains, thus turning the tissue into acellular debris.

Sonoporation is a technique that enhances cell membrane permeability through the interaction of ultrasound with stabilized microbubbles, such as those found in ultrasound contrast agents or pre-existing cavitation nuclei [19]. This method facilitates the transmembrane transport of molecules across the cellular barrier, leveraging both stable and inertial cavitation for molecular transfer. as well as microstreaming and induced shear stress on the membranes. The first experiments on sonoporation date back to the 1980s [18]. Since the initial conception of the idea, numerous studies have explored this subject, yet the precise mechanism of sonoporation that leads to cell permeabilization remains unclear. Furthermore, the synergetic use of ultrasound with lipid- or protein-based vesicles encapsulating both a gas and a drug in liquid form has been explored by many studies for drug delivery [95]. Achieving targeted delivery of therapeutic agents to specific cell types or tissue areas while minimizing systemic toxicity represents a significant challenge with massive potential therapeutic rewards. [159].

Another promising application of cavitation in biological flows is the treatment of vessel occlusions by microbubble-enhanced sonothrombolysis. Cavitation has the potential to directly mechanically damage clots and beneficially influence the efficacy of $rtPA$ by enhancing access to fibrin strands and facilitating drug transport, as reported by [84]. While the specific contributions of microstreaming and microjets in this procedure are not fully understood, it is widely acknowledged that cavitation is crucial in the process of clot dissolution, as indicated by several researchers [124].

Cavitation is also suspected to play a crucial role in traumatic brain injury. Shock waves propagating through the head or sudden impacts, common in motorcycle incidents and sports, can produce low pressures in the interface of the cerebrospinal fluid with the sub-arachnoid space [65]. The subsequent collapse of the formed cavities can damage soft tissue, in a similar manner as in the cases of lithotripsy. These low-pressure regions are found on the opposite side to the initial impact as the pressure wave is inverted due to the acoustic impedance difference across the interfaces [54]. It has been suggested that this mechanism leads to post-traumatic stress disorder, mainly prevalent among war veterans [116].

Another promising use of cavitation in medical treatments is the use of micro-jetting devices, with application in needle-free injections. Laser based injectors focus the optical energy on small liquid-filled chips, where the formation of plasma and the rapid subsequent expansion of vapor bubbles propel the liquid outwards, enabling the delivery of various drugs, into the skin [87]. Such devices have the potential to revolutionize the medical treatment of millions of people, thus further investigation of the cavitation mechanics and the liquid-jet interaction is essential.

An important step in understanding cavitation in biological flows is to examine the bubble dynamics under various conditions and configurations. The dynamics of bubbles present complex challenges due to the presence of diverse scales, various boundaries, and numerous oscillation cycles. These factors collectively pose significant difficulties for theoretical, numerical, and experimental studies.

The theoretical research of cavitation dates back to 1917 [142] when Rayleigh first described the motion of a single bubble surrounded by an infinite medium. Plesset later derived the classic Rayleigh-Plesset model for bubble oscillations [47]. This model is widely used in the literature mainly due to its simplicity. The main shortcoming of this model lies in the assumption of incompressible liquid and thus it is only valid in low Mach flows, with the latter being defined as $\dot{R}/c$, where R is the radius of the bubble and c the speed of sound. Additionally, the model neglects the loss of energy due to acoustic radiation. There are many extensions to the aforementioned model [181], with the Keller-Miksis [74] and the Gilmore-Akulichev [52] models being particularly popular. Their formulation have milder assumptions and are applicable across a broader range of conditions as they consider the compressibility of the surrounding medium and the pressure-dependent sound speed.

These single bubble dynamics models have also been coupled with elastic/visco-elastic models to more accurately capture the tissue/bubble dynamics [191],[40],[37] as well as with

thermal models [134],[192]. These models have been instrumental in advancing theoretical research on bubble dynamics in an unbounded medium. Although, those models give great insight into the non-linear behavior of bubbles under even high amplitude and high-frequency drive sources, such as HIFU, they onlyu model a single spherical bubble, meaning that only stable cavitation phenomena can be considered. Collapsing bubbles and the resulting jet formation as well as bubble cloud dynamics, require different modeling.

Experimental and computational studies have shown that the collapse of a bubble is not spherical for non-symmetrical configurations such as in the proximity to a rigid surface, or a free boundary of a deformable solid or neighboring bubble [91]. To capture those complex bubble dynamics, Plesset and Chapman [131] first employed a potential flow model and a Marker-and-Cell solver technique, to resolve the collapse of a gas bubble near a rigid wall. Similar strategies that employ potential flow solvers and Boundary Elements Methods (BEM) can be found in [79], [175]. The main advantage of the BEM method is that only the surface of the bubble is resolved.To produce more detailed physical representations, studies have adopted fully three-dimensional models capable of detailing the interactions among compressible materials and the propagation of shock waves. These models make use of Godunov-type schemes to calculate fluxes at the interfaces within the discretized domain.

To address the challenge of resolving interface discontinuities between different materials and phases, two primary strategies are employed: interface tracking and interface capturing. Interface tracking involves Lagrangian descriptions where the computational grid adapts to the flow, employing methods such as Level-Set or Ghost Fluid Methods (GFM) [59], [173], and front tracking methods [165]. Although these techniques can deliver accurate results for scenarios with significant deformations, they face limitations in handling the complex topological transformations occurring during collapse [167], and lack conservation properties within the discretisation process [149].

The Diffuse Interface Model (DIM) represents the second strategy, integrating different materials within a single Eulerian framework. In this approach, interfaces between materials are determined by the spatial distribution of each material's volume fraction throughout the domain. This modeling technique sidesteps the complexities associated with direct interface tracking, thereby facilitating the handling of arbitrary interface shapes, extensive deformations, and the dynamic emergence or disappearance of interfaces [149, 24]. Thus in the present thesis, a DIM method was employed to accurately capture bubble dynamics in biological flows.

Moreover, numerous numerical investigations have concentrated on the dynamics of bub-

7

bles induced by shock waves within a liquid medium [15, 25, 68]. Nonetheless, the presence of a solid material near a bubble significantly impacts its collapse characteristics and dynamics. [144].

In the seminal study by Johnsen and Colonius [68], the shock-induced bubble dynamics were analysed using a pressure pulse profile derived from experimental observations. This investigation highlighted the potential damage caused by the collapse of non-condensable bubbles. Pan et al. [119] conducted research on the mechanics of sonoporation in liquid cells through shock-induced bubble collapse, uncovering how overpressure can be adjusted to influence the penetration depth. Two notable studies using Fluid-Structure Interaction models are the works of Cao et al. [25] and of Wang [174]. Wang [174] simulated the shock-induced bubble collapse near kidney stones, highlighting the importance of the amplitude of the reflected shock wave from the solid wall. In this study, a two-way coupling between the Eulerian flow-field solution and the finite element model for the solid was incorporated. Cao et al. [25] elaborated on this approach, revealing the intricate effect of acoustic impedance on bubble dynamics, reporting differences up to 30% in the recorded pressure during the collapse, liquid jet formation, and collapse time, between a wall treated either as a boundary condition (infinite acoustic impedance) or as an elastic solid. However, the authors reported only on stiffer materials or small deformation of tissue-like materials. Turangan et al. [166] utilized a free Lagrangian method to simulate erosion damage caused by shock-induced bubble collapse near rigid materials. Kaiser et al. [70] showcased fully 3D numerical simulations of shock-induced bubble collapse adjacent to a water/gelatin interface, confirming the self-similarity of axis-symmetrical outcomes. Kobayashi et al. [80] applied an enhanced ghost-fluid method to examine the behavior of a shock-wave induced bubble near various materials, using the stiffened gas equation of state but omitting the deviatoric stress tensor component. Freund et al. [48] explored the jet impingement response of tissues during Extracorporeal Shock Wave Lithotripsy (ESWL), treating tissue as a viscous fluid in their modeling. Coralic et al. [33] conducted further 3-D numerical simulations within a capillary to study vascular injury from inertial collapse. The constraints of the studies mentioned earlier primarily stem from two aspects: the simplification of soft tissue as a liquid, which overlooks the impacts of shear stresses and elasticity; and the limitations in Fluid-Structure Interaction (FSI) modeling, particularly the Eulerian-Lagrangian coupling with Finite Element Method (FEM) solvers, restricting the models to scenarios of low deformation that involve rigid materials such as metals and kidney stones. Thus, the present thesis aims to overcome these limitations by enabling large solid deformations and accurate bubble dynamics, through the implementation of a DIM model.

The aforementioned multiphase models with either interface tracking or interface capturing can accurately model the dynamics of both single bubbles [149] and of clouds [139, 140]. However explicitly resolving acoustic waves, bubble interfaces, and shock waves, can only be simulated on the scale of micro-seconds, and for a low number of bubbles. Thus those models pose the problem of forbidding computational resources for large-scale simulations. The work of [143] illustrates the high computational cost to simulate a bubble cloud as 13 trillion cells were required to resolve 15 thousand bubbles. Several models have been developed to circumvent this problem, by employing sub-grid models for the bubbles [32] [152, 16, 104, 103, 50]. The subgrid models, do not explicitly resolve the full dynamics of individual bubbles, but they rather model them as either a Lagrangian particles or assume a stochastic distribution of bubbles. These particles undergo spherical oscillations governed by a single bubble dynamics models such as Keller-Miksis or Gilmore-Akulichev. Finally the volumetric oscillations of the bubbles are mapped to the eulerian grid and influence the volume fraction of the secondary phase.

Such models, that utilize subgrid models for the bubbles, follow a mixture-averaging approach and can be divided into two categories [1]. The first one is a volume-averaged method where each individual bubble is tracked as a Lagrangian particle. The mean flow, with the sub-grid model, is coupled through the projection of the volume fraction. The second one is an ensemble-average approach where rather than tracking the dynamics of each individual bubble, the model considers the statistically averaged dynamics of the mixture by assuming that a stochastic distribution of bubbles is dispersed across each computational grid cell. Although these models overcome the problems related to the computational cost, they require scale separation i.e. that the cell volume is much larger than the bubbles' distances. This requirement leads to low mass and volume fractions of the secondary phase. Thus in the present study, such an approach was not pursued.

Finally, in the context of shock wave lithotripsy, numerical simulations exhibit a broad spectrum of complexity in modeling. Cleveland et al. [31] demonstrated that the maximum stress experienced by a kidney stone arises from the constructive interference of initial longitudinal waves with shear waves, which are produced as the incident shock wave travels along the stone's outer surface. The experimental findings of [129] indicate that the tensile phase of the lithotripter pulse creates a bubble cloud around the stone's surface. Upon pressure restoration, the collapse of this bubble cloud leads to erosion of the stone's surface. Therefore, understanding the fluid-structure interaction between the kidney stone and the cavitating bubbles is crucial for clarifying this process.

One limitation of many multiphase/multimaterial numerical solvers is the requirement of high computational resources to accurately capture material interfaces and significant pressure gradients. A strategy to mitigate the growing need for these resources while enabling the use of advanced numerical models and the ability to simulate more complex geometries is to refine and adapt the mesh in "important" areas of the flow while reducing it in regions deemed less important.

Any flow characterized by multiple scales, often resulting in localized areas of high gradients, is suitable for AMR. In principle, the greater the discrepancy between spatial and temporal scales, the more significant the potential benefits. Bubble dynamics is a prime example of such cases, where large deformations in material interfaces are present. In extreme cases, AMR enables the solution of what would otherwise be excessively costly with fixed meshes. Such cases can be found in [62].

In general, AMR involves altering an existing mesh to more precisely represent various flow characteristics. Three distinct types of AMR strategies can be identified: r-refinement, h-refinement, or p-refinement, while the combination of these is also possible.

R-refinement involves enhancing the mesh resolution by redistributing grid points towards areas of higher gradients without changing the mesh's overall number of nodes or cells, or its connectivity.

P-refinement refers to the increase of the polynomial order within each element, thus refining the flow structures and increasing the accuracy. It's widely utilized in Finite Element Method (FEM) and discontinuous Galerkin method [121], however, it's not relevant for the Finite Volume Method, discussed in the present thesis.

The last type of AMR is the h-type. H-refinement enhances mesh resolution by altering its connectivity (splitting and merging of cells), which may or may not affect the total number of grid cells or points, depending on the approach. This category can be further subdivided into block-structured AMR and on-the-fly splitting and merging of individual cells. In the former category, an initial block of a structured mesh is split. This approach enables the efficient handling of large structured meshes. In contrast, the on-the-fly approach enables simulations of more complex geometries with unstructured meshes.

In the present thesis, the latter was selected. To this end, the Forest of oct-trees AMR technique for unstructured hybrid meshes originally published by Papoutsakis et al. [121] was utilized. This approach allows an on-the-fly refinement of the mesh to self-similar elements

to any desired level. The connectivity of the elements, their genealogy, and partitioning are outlined using linked lists of pointers integrated into a tree data structure. This setup enables real-time splitting, merging, and re-distributing of the computational mesh by adjusting the links at each node of the tree.

The ForestFV AMR technique is designed to capture the intricate dynamics of bubble interfaces and the shocks and refraction waves produced by bubble collapse with high precision. Thus, it is expected that this enhanced spatial resolution will reduce the errors associated with resolving interface discontinuities, offering a refined method for capturing interfaces.

1.2   Objectives

The aim of the present thesis is the development of a consistent multi-phase and multi-scale numerical solver to accurately and efficiently capture bubble dynamics, shock-wave propagation across interfaces, and fluid-structure interactions with large solid deformation, tailored specifically for biomedical applications.

The primary objectives of this thesis are summarised as follows:

1. To develop an h-type Adaptive Mesh Refinement (AMR) numerical framework able to handle both structured and unstructured meshes efficiently, with good scaling characteristics.

2. To develop, implement, and validate compressible diffuse interface models able to capture the intricate dynamics of bubble collapse and fluid-structure interaction in the context of biological flows.

3. To examine the shock-induced gas bubble-collapse dynamics during shock wave lithotripsy under various configurations and initial conditions.

4. To elucidate the inertial bubble collapse potential for tissue injury during ultrasound procedures.

5. To investigate the liquid-jet-skin interaction in needle-free injectors.

1.3   Thesis Outline

The main body of the present thesis is organized, as described below:

Chapter 2 outlines the developed diffuse interface model, starting with the governing equations of the model, the Equation of State (EoS), and the numerical implementation. Following, the adaptive mesh refinement framework is presented. Finally, validation cases are presented for a number of test cases.

Chapter 3 examines the shock-induced bubble collapse close to a soft tissue and a kidney stone, during shock wave lithotripsy, using the developed numerical framework. Three different configurations are examined for detached and attached bubbles. The characteristics of the bubble dynamics for these cases are discussed. A non-previously described mechanism leading to tissue damage mechanism is presented, revealing the intricate role of inertial cavitation in shock wave-lithotripsy.

Chapter 4 investigates the dynamics of shock-induced gas bubble collapses in a wider range of configurations. These include the stand-off distance, the bubble size, and the shock wave amplitude. The findings give insight into the role of various key parameters on bubble dynamics including the collapse time, shock wave emissions, penetration depth, volumetric changes of the gas phase secondary collapses, and liquid jet velocities. This study aims to further our understanding of inertial bubble collapse next to bio-materials and elucidate the potential for adverse side effects.

Chapter 5 examines laser-based needle-free injectors and the liquid-jet skin interaction. Validation cases are presented for various initial conditions. It is found that the liquid-jet velocities are in agreement with those from experimental and numerical studies. Furthermore, 4 different skin-mimicking materials are examined, and the penetration depth and stress development are reported. This study constitutes an initial investigation on the fluid-solid interaction in needle-free injectors and how computational modeling can help in tuning working parameters for various skin types.

Chapter 6 emphasises the principal conclusions of this study and proposes recommendations for subsequent research and practical applications.

Chapter 7 offers a comprehensive overview of the publications in peer-reviewed journals and conference proceedings that have emerged from this research.

2   Methodology

2.1   Governing equations

The principal flow features during the inertial collapse of a gas bubble in SWL include the shock-wave interaction between the incident and reflected shock waves on the interfaces of the bubble and the solid surfaces, the large deformation of solids as a result of the collapse of the bubble, and the induced compressibility effects.

The 6-equation DIM model [148] and its extension for isotropic elastic solids [44] is adopted, to model shock induced gas bubble collapses and soft tissue interaction, shock wave impacts on kindey stones and cavitation-induced jetting in needle free injectors. In the specific inertia-driven configuration, viscous forces, surface tension,thermal diffusion, mass transfer and phase change between phases are neglected. The Reynolds number, which quantifies the ratio of inertial to viscous forces, sheds light on the impact of neglecting viscous terms during shock-induced collapse. Research by E. Johnsen et al. [69] indicates that the Reynolds number for peak jet velocities in such events typically lies around 10^3. This observation is reiterated in Chapter 3, suggesting that viscosity is unlikely to significantly influence the dynamics of jets and bubbles. Additionally, the Weber number is employed to rationalize excluding the surface tension. For bubbles with an initial radius equal to $10\mu m$, the Weber number ranges from 10^3 to 10^4, leading to similar conclusions. Thermal and mass diffusion between water and air, being several orders of magnitude lower than viscosity, is also considered negligible. Furthermore, studies [125],[4] demonstrate that phase transitions do not substantially affect bubble dynamics in the initial stages of collapse. This approach aligns with assumptions made by various scholars regarding the dynamics of inertial gas bubble collapses [55]. The solid materials are considered elastic. Soft tissue in particular exhibits various non-linear effects such as strain-stiffening or visco-elastic effects. These effects are neglected in the present study. However, given that in a considerable number of numerical studies on shock-induced bubble collapse the tissue is modelled as a viscous fluid, the isotropic elasticity is a first step towards a better understanding of the bubble-tissue interaction [33],[80].

The specific model has been validated for bubble dynamics and has been used to capture the fluid-structure interaction and the extreme deformations for soft and rigid solids. The governing equations are:

$$\frac{\partial(\alpha_i \rho_i)}{\partial t} + \nabla\Big(\alpha_i \rho_i \vec{u}\Big) = 0, \quad i = 1, ..., N$$

$$\frac{\partial(\rho\vec{u})}{\partial t} + \nabla\Big(\rho\vec{u} \otimes \vec{u} - \boldsymbol{S}\Big) = 0$$

$$\frac{\partial \alpha_i}{\partial t} + \vec{u}\nabla\alpha_i = \mu(p_k - p_I), \quad i = 1, ..., N-1 \tag{1}$$

$$\frac{\partial(\alpha_i \rho_i e_i)}{\partial t} + \nabla\Big(\alpha_i \rho_i e_i \vec{u}\Big) + \alpha_i tr\Big(\sigma_i \frac{\partial \vec{u}}{\partial \vec{x}}\Big) = -p_I \mu(p_K - p_I), \quad i = 1, ..., N$$

$$\frac{\partial e^\beta}{\partial t} + \frac{\partial e^\beta}{\partial \vec{x}}\vec{u} + \Big(\frac{\partial \vec{u}}{\partial \vec{x}}\Big)^T e^\beta = 0$$

where the scalar fields $\alpha_i, \rho_i, p_i, e_i, \sigma_i$ correspond to the volume fraction, the density, the pressure, the internal energy, and the stress tensor for each material i, ρ is the mixture density, $\mathbf{u}$ is the velocity vector, $\mathbf{S}$ is the stress tensor, δp is the pressure difference between the phases, $e^{\boldsymbol{\beta}}$ are the columns of F^{-T} (i.e. the local cobasis) with F being the Jacobian of the deformation defined as $F = \partial x/\partial X$ with x being the Eulerian coordinates and X the Lagrangian, while p_I is the interfacial pressure defined as:

$$p_I = \frac{\sum \frac{p_k}{Z_k}}{\sum \frac{1}{Z_k}}, \tag{2}$$

where Z_i is the acoustic impedance of the material i. The mixture density and the saturation constraints are defined as:

$$\rho = \sum_i^N (\rho\alpha)_k, \quad \sum_i^N \alpha_i = 1 . \tag{3}$$

Given the non-conservative formulation of the specific energy equations in Eq. (1), an additional equation for the total mixture energy is introduced, to ensure the numerical conservation of the total energy [148]. The total energy is used during the pressure relaxation step, to re-initialize the internal energies of each phase. The total mixture energy conservation equation is defined as:

$$\frac{\partial(\rho E)}{\partial t} + \nabla\Big[(\rho E + \boldsymbol{S})\vec{u}\Big] = 0 . \tag{4}$$

The closure of the system of Eqs.1, is achieved by the relation between the pressure density and the internal energy as dictated by the material EoS, as:

$$e_i = e_i(\rho_i, p) . \tag{5}$$

For liquid substances, the stiffened gas equation of state is used:

$$p_i = (\gamma_i - 1)\rho_i e_i - \gamma_i \pi_{\infty i} \ , \tag{6}$$

where, γ and π_∞ are parameters of the EoS. For solids, the stiffened gas EoS is extended to account for the elastic energy as:

$$e_i = e_i^h(\rho_i, p) + e_i^e(\rho, \tilde{G}) \ . \tag{7}$$

In Eq. 7, e_i^h is the hydrodynamic component which depends solely on density and pressure, while the second part corresponds to the elastic component dependent on the tensor $\tilde{G}$. The tensor $\tilde{G}$ is defined as:

$$\tilde{G} = \frac{G}{|G|^{1/3}} \ , \tag{8}$$

where G is the finger tensor, i.e. the inverse of the left Cauchy–Green tensor $B = FF^T$, thus, $G = F^{-T}F^{-1}$. The components of F^{-T} are the vectors $\boldsymbol{e^\beta}$. The vectors $\boldsymbol{e^\beta}$ form the jacobian of the deformation defined as $F = \partial x/\partial X$ with x being the Eulerian coordinates and X the Lagrangian. The elastic component ε_s^e of the specific energy for a solid as described in the Equation (7) is:

$$\varepsilon_s^e = \frac{\mu_s}{4\rho_{s0}} \operatorname{tr}\left((\tilde{G} - I)^2 \right) \ . \tag{9}$$

The stress tensor for solids is:

$$\mathbf{S}_s = -2\rho \frac{\partial e}{\partial \tilde{G}} \tilde{G} = -p_s I - f_s(\mu_s, \rho_s, \rho_{s0}, G) \ ,$$

$$f_s(\mu_s, \rho_s, \rho_{s0}, G) = \mu_s \frac{\rho_s}{\rho_{s0}} \left(\frac{1}{|G|^{2/3}} \left(G^2 - \frac{J_2}{3} I \right) - \frac{1}{|G|^{1/3}} \left(G - \frac{J_1}{3} I \right) \right)$$

where μ is the shear modulus, ρ_s is the density of the solid phase, ρ_{s0} is the initial density of the material, p_s is the hydrodynamic pressure and $J_i = tr(G^i)$.

The total stress tensor $\mathbf{S}$ is defined as:

$$\mathbf{S} = -\sum_i^N (p_i I + f_i(\mu_s, \rho_s, \rho_{s0}, G)) \tag{10}$$

For a viscous fluid the stress tensor is further expanded to incorporate the viscous stress tensor:

$$\mathbf{T} = 2\eta_m(\mathbf{D} - \frac{1}{3}(\nabla\vec{u})I) \tag{11}$$

where η_m is the mixture viscosity and the deformation tensor $\mathbf{D}$ is defined as::

$$\mathbf{D} = \frac{1}{2}(\nabla\vec{u} + \nabla\vec{u})^T) \tag{12}$$

2.2   Numerical method

The system of equations (1) can be written as:

$$\frac{\partial U_i}{\partial t} + \frac{\partial F_{ij}}{\partial x_j} + H_{ikl}\frac{\partial u_l}{\partial x_k} = \mu S_i, \quad i = 1, ..., 3 \cdot N_{mat} + 12 , \tag{13}$$

where U_i are the components of the state vector $\mathbf{U}$, F_{ij} is the flux vector, H_{ikl} is the non-conservative term, S_i corresponds to the source terms and the u_k are components of the velocity vector $\vec{u}$ at the direction k (see Appendix A). The total number of equations is equal to $3 \cdot N_{mat} + 12$, where N_{mat} is the number of the different materials. The presence of non-conservative and relaxation terms introduces difficulties to the integration of the set of governing equations. The integration of the governing equations is achieved by an explicit density-based implementation of the Finite Volume methodology [161, 44] for hybrid unstructured grids incorporating hexahedral prismatic and tetrahedral elements (ForestFV). The specific implementation developed utilizes a graph representation of the computational domain as a dynamically evolving forest of oct-trees [121, 120].

The integration of the governing equations is achieved by employing the splitting procedure described in [44] in the following consecutive steps:

1. A hyperbolic step, i.e. solving (1) without the source terms.

2. A pressure relaxation step to restore the mechanical equilibrium.

3. A Ghost Fluid Method (GFM) for the correct treatment of solid-fluid/gas interfaces.

2.2.1   Hyperbolic step

The system of equations (1) in the absence of source terms can be expressed in a homogeneous formulation as:

$$\frac{\partial U_i}{\partial t} + \frac{\partial F_{ij}}{\partial x_j} + H_{ikl}\frac{\partial u_l}{\partial x_k} = 0, \quad i = 1, ..., 3 \cdot N_{mat} + 12 , \tag{14}$$

In the current implementation, the system of equations (13) is discretized following an explicit finite-volume Godunov method for a general 3-dimensional non-Cartesian computational mesh as:

$$\mathbf{U}_i^{n+1} = \mathbf{U}_i^n - \frac{\Delta t}{V_i}\left(\sum_{f=1}^{N} A_f \mathbf{F}_f^{\star} \cdot \mathbf{n}_f + \sum_{f=1}^{N} A_f\left(\sum_{k=1}^{3} n_k \sum_{l=1}^{3} H_{ikl}u_l^{\star}\right)\right) , \tag{15}$$

where V_i, A, n_f are the volume of the cell, area, and the normal vector of a face respectively. $\mathbf{F}_f^*$ is the flux tensor computed at the interfaces with the HLLC approximate Riemann solver [161], and $\mathbf{u}_f^*$ is the flow velocity vector.

2.2.2   HLLC Riemann solver

The HLLC Riemann solver is used to solve the Riemann problem across an cell boundary. More details about the interface relations and the jump conditions can be found in [117].

The left and right waves speeds are defined as:

$$S_R = max(u_L + c_L, u_R + c_R)$$
$$S_L = max(u_L - c_L, u_R - c_R)$$

where $u_{L,R}$ are the normal flow velocities to the face, and $c_{L,R}$ are the longitudinal sound speed of the mixture defined as:

$$c^2 = \sum_{i}^{N_{mat}} Y_i c_i^2, \quad and \quad c_i^2 = \gamma_i \frac{(p_i - \pi_\infty)}{\rho_i}$$

Using the HLLC approximation the intermediate wave speed is estimated as:

$$S_* = \frac{(\rho u^2 + \sigma_{11})_L - (\rho u^2 + \sigma_{11})_R - S_L(\rho u)_L + S_R(\rho u)_R}{(\rho u)_L - (\rho u)_R - S_L\rho_L + S_R\rho_R} \tag{16}$$

The star values for the conserved variables are:

$$\left((\alpha\rho)_k\right)^*_{L,R} = \left((\alpha\rho)_k\right)_{L,R} \frac{S_{L,R} - u_{L,R}}{S_{L,R} - S^*}$$

$$\sigma^*_{11} = \frac{(u_R - S_R)\rho_R\sigma_{11L} - (u_L - S_L)\rho_L\sigma_{11R} + (u_L - S_L)\rho_L(u_R - S_R)\rho_R(u_R - u_L)}{(u_R - S_R)\rho_R - (u_L - S_L)\rho_L}$$

$$\sigma^*_{12} = \frac{(u_R - S_R)\rho_R\sigma_{12L} - (u_L - S_L)\rho_L\sigma_{12R} + (u_L - S_L)\rho_L(u_R - S_R)\rho_R(v_R - v_L)}{(u_R - S_R)\rho_R - (u_L - S_L)\rho_L}$$

$$\sigma^*_{13} = \frac{(u_R - S_R)\rho_R\sigma_{13L} - (u_L - S_L)\rho_L\sigma_{13R} + (u_L - S_L)\rho_L(u_R - S_R)\rho_R(w_R - w_L)}{(u_R - S_R)\rho_R - (u_L - S_L)\rho_L}$$

$$v^*_{L,R} = v_{L,R} + \frac{\sigma^*_{12} - (\sigma_{12})_{L,R}}{(u_{L,R} - S_{L,R})\rho_{L,R}}$$

$$w^*_{L,R} = w_{L,R} + \frac{\sigma^*_{13} - (\sigma_{13})_{L,R}}{(u_{L,R} - S_{L,R})\rho_{L,R}}$$

The deformation tensor star values are defined as normal to the face and are given by:

$$(A_{1j})^*_{L,R} = \frac{(A_{1j})_{L,R}(u_{L,R} - S_{L,R}) + (A_{2j})_{L,R}(v_{L,R} - v^*_{L,R}) + (A_{3j})_{L,R}w_{L,R} - w^*_{L,R})}{u^* - S_{L,R}}$$

$$(A_{2j})^*_{L,R} = (A_{2j})_{L,R}$$

$$(A_{3j})^*_{L,R} = (A_{3j})_{L,R}, \quad with \quad j = 1, 2, 3$$

The total mixture energies for the left and right star states are given by:

$$E^*_{L,R} = \frac{\rho_{L,R}E_{L,R}(u_{L,R} - S_{L,R}) - \sigma_{11L,R}u_{L,R} - \sigma_{12L,R}v_{L,R} - \sigma_{13L,R}w_{L,R} + \sigma^*_{11}S^* + \sigma^*_{12}v^*_{L,R} + \sigma^*_{13}w^*_{L,R}}{\rho^*_{L,R}(S^* - S_{L,R})}$$

$$(17)$$

where the total energy is:

$$E = Y_s e_s + Y_g e_g + \frac{1}{2}u^2 + \frac{1}{2}v^2 \tag{18}$$

The star values for the non-conservative variables are:

$$\alpha^*_{kL,R} = \alpha_{kL,R}$$

$$\rho^*_{kL,R} = \rho^0_{kL,R}\frac{u_{L,R} - S_{L,R}}{S_M - S_{L,R}}$$

Finally the star values for the pressures $(p_k)^*_{L,R}$ and internal energies $(e_k)^*_{L,R}$ must be
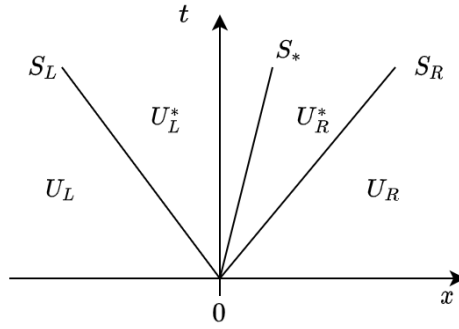
Figure 1: Wave structure of HLLC Riemann solver. The star region is separated into two constant states, by a middle wave with speed S_*

defined. The EoS and the jump relations for the internal energies define a 2x2 system of equation, given the phase densities $(\rho_k)^*_{L,R}$ and the geometric variables $(A_{ij})^*_{L,R}$. Thus we first solve for the star values of the pressure. The internal energies can be later found by using the respected EoS with the star values:

$$e^*_{kL,R} = e_g\Big((p_g)^*_{L,R}, (\rho_g)^*_{L,R}\Big), \quad for\,fluids$$

$$e^*_{kL,R} = e_s\Big((p_s)^*_{L,R}, (\rho_s)^*_{L,R}, (A_{ij})^*_{L,R}\Big), \quad for\,solids$$

Having determined the star values, the flux across a cell boundary face is then determined [160]:

$$\mathbf{F}^{hllc}_{i+\frac{1}{2}} = \begin{cases} \mathbf{F}_L & \text{if} \quad 0 \leq S_L, \\ \mathbf{F}_L + S_L(\mathbf{U}_{*L} - \mathbf{U}_L) & \text{if} \quad S_L \leq 0 \leq S_*, \\ \mathbf{F}_R + S_R(\mathbf{U}_{*R} - \mathbf{U}_R) & \text{if} \quad S_* \leq 0 \leq S_R, \\ \mathbf{F}_R & \text{if} \quad 0 \geq S_R \end{cases} \tag{19}$$

The computation of the numerical fluxes, is performed using the reconstructed primitive variables on the faces of the cells.

2.2.3 Pressure relaxation step

At the end of the hyperbolic step, the first stage of the splitting procedure for the numerical solution of the model (1) is complete. The obtained solution corresponds to a mechanical disequilibrium state in which the relaxation terms are neglected. At this stage, the N_{mat}

discrete materials are under different pressures. The relaxation procedure ensures that in the presence of shock or rarefaction waves the volume of each phase must be adjusted to reach pressure equilibrium. This is reflected in the right-hand side of the volume fraction equation, which represents the volume fraction expansion with rate μ. Additionally, the change in the volume fraction is reflected by pressure work, which is shown on the right-hand side of the internal energy equation. When the rate μ approaches infinity, the mechanical equilibrium is reached instantaneously. Thus this step entails the solution of:

$$\frac{\partial U_i}{\partial t} = \mu S_i, \quad i = 1, ..., 3 \cdot N_{mat} + 12 \; , \tag{20}$$

where μS_i is composed of the right hand-side terms of (1).

By combining the equations of the specific energies, the mass conservation, and the saturation constrain, the following relation is obtained, [92]:

$$\frac{\partial e_k}{\partial t} + p_k \frac{\partial v_k}{\partial t} = 0 \; , \tag{21}$$

where $v_k = 1/\rho_k$ is the specific volume. Integration over time, yields:

$$e_k^f - e_k^i - p_k \left(\tau_k^f - \tau_k^i \right) = 0 \; , \tag{22}$$

where f denotes the final relaxed state and i is the initial disequilibrium state after the hyperbolic step. Substituting the internal energy using the stiffened gas EoS, and using the saturation constrain (3), an implicit relation of the pressures p^f and p^i with the volume fractions a_k^i is derived:

$$\sum_{k=1}^{N_{mat}} \frac{\alpha_k^i}{\gamma_k} \left(\frac{p_k^i + \pi_{\infty,k}}{p_{rel} + \pi_{\infty,k}} \right) = \sum_{k=1}^{N_{mat}} \frac{\alpha_k^i}{\gamma_k} \; . \tag{23}$$

Eq. (23) is solved using the Newton-Raphson method. The resulting relaxed pressure p_{rel}, and the new volume fractions that correspond to the relaxed pressure field can now be updated. It is noted that the relaxed pressure will not, in general, satisfy the total energy of the mixture or the equation of the state of the mixture. For this reason, a correction is needed using the total mixture energy E which is intrinsically conservative. Given the relaxed volume

fractions, the mixture equilibrium pressure will be determined by the mixture EoS as:

$$p_{eq} = \frac{\rho \varepsilon^h - \left(\sum_i^{N_{mat}} \frac{\alpha_i \gamma_i p_{xi}}{\gamma_i - 1} \right)}{\sum_i^{N_{mat}} \frac{\alpha_i}{\gamma_i - 1}} \; , \tag{24}$$

where ε^h is the hydrodynamic part of the mixture energy given by:

$$\varepsilon^h = E - \frac{1}{2}(u^2 + v^2 + w^2) - e_{elastic} \; , \tag{25}$$

with the elastic energy defined as:

$$e_{elastic} = \sum_i^{N_{solid}} Y_{si} e_i^e \; . \tag{26}$$

Finally, the mixture equilibrium pressure and the internal energies of the N materials can be updated following the equation of state:

$$e_k^h = e_k^h \left(p_{eq}, \frac{(\alpha\rho)_k}{\alpha_k} \right), \quad k = s, g \quad e_s^e = e_s^e(A_{ij}), \quad k = s \; . \tag{27}$$

2.2.4   Ghost fluid method

The DIM framework introduce certain complexities at the material interfaces of solids with gases or fluids.

1. The tangential stresses σ_{12}, σ_{13} will not be zero in the gas/fluid region of the interface due to the diffused interface which will result in the presence of a small volume fraction of solid.

2. In the solid/fluid or gas interfaces the numerical diffusion of the transverse velocities creates nonphysical stress waves in the solid.

To deal with those problems two modifications should be made. The first step is to track and identify the interfaces. To detect the interfaces we use the volume fraction to define a level set function ϕ defined as:

$$\phi_i = \alpha_i - \alpha_{interface} \tag{28}$$

where $\alpha_{interface}$ is a constant equal to 0.5. Thus the sign of ϕ indicates the presence or not

of a dominant solid phase. The product of ϕ of two neighboring cells also indicates the type of the interface. A negative product reveals a solid-gas or fluid interface whereas a positive all the other types of interfaces.

A correction to the Riemann problem solution is introduced to avoid the appearance of the tangential stresses influencing the solution across a solid/fluid interface. This correction guarantees that $\sigma_{13}^* = \sigma_{12}^* = 0$, if $\phi_L\phi_R < 0$. Thus:

$$
\sigma_{12}^* = \begin{cases} \frac{(u_R-S_R)\rho_R(\alpha_s\sigma_{12s})_L-(u_L-S_L)\rho_L(a_s\sigma_{12s})_R+(u_L-S_L)\rho_L(u_R-S_R)\rho_R(v_R-v_L)}{(u_R-S_R)\rho_R-(u-S_L)\rho_L} & \text{if } \phi_L\phi_R > 0 \\ 0, & \text{if } \phi_L\phi_R < 0 \end{cases}
$$

$$(29)$$

$$
\sigma_{13}^* = \begin{cases} \frac{(u_R-S_R)\rho_R(\alpha_s\sigma_{13s})_L-(u_L-S_L)\rho_L(a_s\sigma_{13s})_R+(u_L-S_L)\rho_L(u_R-S_R)\rho_R(w_R-w_L)}{(u_R-S_R)\rho_R-(u-S_L)\rho_L} & \text{if } \phi_L\phi_R > 0 \\ 0, & \text{if } \phi_L\phi_R < 0 \end{cases}
$$

$$(30)$$

To address the second problem a Ghost Fluid Method (GFM) approach is employed [2, 44, 117]. If an interface is found across the face of two neighboring cells, then two numerical fluxes, $F_{i+1/2,L}^*$ and $F_{i+1/2,R}^*$, will be computed for the current face. Those fluxes are constructed by extrapolating the tangential velocities from both sides of the interface. Thus:
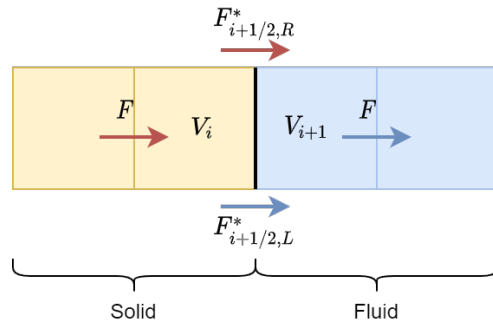
Figure 2: Ghost fluid method, numerical fluxes of Riemann problems across a solid-fluid interface

$$
\begin{aligned}
F_{i+1/2,L}^* &= F(V_{i,L}^n, V_{i+1}^n) \\
F_{i+1/2,R}^* &= F(V_i^n, V_{i+1,R}^n)
\end{aligned}
$$

$$(31)$$

where $V_{i,L}^n$ has the tangential velocity of V_{i+1}^n, and $V_{i+1,R}^n$ has the tangential velocity of V_i^n, i corresponds to the current cell under consideration and $i+1$ to the neighboring cell. For this, the interface needs to be captured and its movement needs to be predicted. Thus, the

calculation of a temporary solution for the current cell is required, using Eq. (15), modified with the correct fluxes from Eq. (31). For advected interfaces, the transverse speed of the upwind cell is considered.

$$\vec{v}_i^{n+1} = \begin{cases} \vec{v}_i^{n+1}, & \text{if} \quad \phi_i^n \phi_i^{n+1} < 0 \\ \vec{v}_{i+1}^{n+1}, & \text{if} \quad \phi_i^n \phi_i^{n+1} > 0 \end{cases}, \tag{32}$$

where $\vec{v}$ is the vector of the transverse velocity. For multidimensional cases, the interface may not lie on a single face, rather it is defined as a plane for each cell. For that, a local 3D reconstruction of the interface is required. The flow velocities can be projected onto the reconstructed plane's normal and tangential vectors.

2.2.5 Second order extension

In order to preserve the flow structures and the interfaces, a higher-order extension to the first-order Godunov scheme is needed. To this end, a second-order MUSCL-type scheme is used, formulated for unstructured grids [28]. For the spatial reconstruction, the gradient is computed using the least squares method, and the `minmod` limiter is used to suppress spurious oscillations. The two-step integration scheme is summarized as:

$$\begin{aligned} U_i^{n+\frac{1}{2}} &= U_i^n + \frac{\Delta t}{2}\text{RHS}(V_i^{\text{rec}}) \\ U_i^{n+1} &= U_i^n + \Delta t\, \text{RHS}(V_i^{n+\frac{1}{2}}) \end{aligned}, \tag{33}$$

where RHS is the right-hand side of the Eqs. (15), evaluated using the primitive reconstructed variables on the faces of the cells V_i^{rec}. $V_i^{n+1/2}$ is the primitive reconstruction of the half-time evolution of the state vector $U_i^{n+\frac{1}{2}}$. The reconstruction with the conservative variables was found to lead to spurious oscillations in the solution. Similar findings have been reported in [149, 28]. Thus, it is deemed necessary that the primitive variables are used for the spatial reconstruction.

2.3 Adaptive Mesh Refinement

Bubble collapse and multi-material interaction are the results of a several interactions of phenomena occurring at different scales across fine interfacial structures. These structures present a dynamically changing spatial distribution, are not known *a*priori, and require a localized fine resolution of the flow field. Additionally, given the high number of equations

that are being solved in each time step, the three additional steps of relaxation re-initialization, and the ghost fluid method, there is a need to contain the computational costs.

The Finite Volume implementation presented in this thesis is based on the Forest of oct-trees AMR framework that was developed by Papoutsoukis et. al [121]. This approach is based on a topological representation of the computational mesh by a hierarchical structure consisting of oct- quad- and binary trees. The ancestral elements of the mesh are split into self-similar elements allowing each tree to grow branches to an arbitrary level of refinement. The resulting elements have the same quality metrics of the ancestral mesh thus preserving the mesh characteristics. The developed h-refinement method enables us to increase the spatial resolution for the computational mesh in the vicinity of the points of interest such as interfaces, geometrical features, or flow discontinuities. The connectivity of the elements, their genealogy, and their partitioning have been described by linked lists of pointers. These pointers are attached to the tree data structure. This facilitates the on-the-fly splitting, merging, and repartitioning of the computational mesh by rearranging the links of each node of the tree.

In the current FV implementation presented here (ForestFV), the partitioning of the connectivity graph has been upgraded thus, allowing the sending and receiving of individual trees of the forest and their topological characteristics across processors in addition to the field variables. This ensures a balanced computational load and memory allocation across processors. Changes in the forest topology are expressed by re-stitching pointers and relations, rather than moving and rearranging data structures.

The tree data structure that contains the information for each cell is depicted in Fig. 4. Each tree stores the vector of the conserved variables (leaf), the pointers for the addresses of the parent tree the ancestor (lowest level) tree, the previous and the next tree node, and the neighbors for each face of the element. The graph consisting of all the trees (cells) as they split and merge, creates a forest of octa, quad or binary trees depending on the splitting procedure and dimensions of the problem. This graph is partitioned using the graph domain decomposition library ParMETIS [73] which splits the domain into sub-domains, enabling dynamic load balancing among the processing nodes.

This on-the-fly AMR implementation allows for the continuous refinement and coarsening of the grid. As such,it can help in improving shock-capturing of the model and enhances the resolution of the interface discontinuities. It has proven to be a powerful tool for modeling the complex mechanism of bubble growth [120], tracking the volatile topology of the bubble interface during bubble collapse, and capturing the progression of pressure wave fronts.
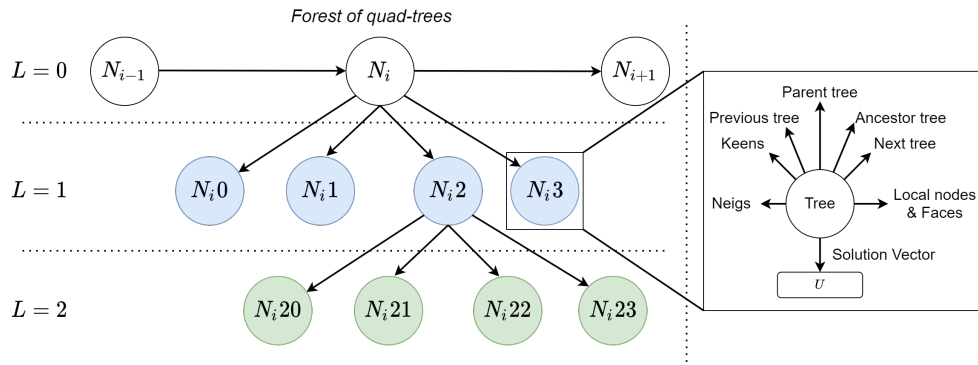
Figure 3: Forest of quad-trees with 2 levels of refined elements. On the left, the address of each element is depicted as N_i. On the right the tree data structure.

Splitting or merging cells is decided based on the basis of desirable mesh resolution needed to capture the flow characteristics. Those can be shock waves, interface tracking for low numerical diffusion, high velocities, or density gradients. Refinement based on geometrical characteristics of the flow field initialization is also incorporated.

For each cell the presence of significant gradients [149] serves as an indicator for refinement and is based on the following expression:

$$\frac{\left|U_{Neig}^i - U_{current}^i\right|}{\min\left(U_{Neig}^i, U_{current}^i\right)} > \epsilon \ , \tag{34}$$

where $\mathbf{U}$ is the vector of the conservative variables. ϵ serves as a cut-off limit for the refinement.

The conservation properties of the discretization for non-conforming faces in the Finite Volume framework presented here is ensured by treating the non-conforming faces as individual faces of polyhedral elements. After every adaptation of the mesh, a smoothing pass is executed to ensure a $1:1$, $1:2$, or $2:1$ connectivity. Finally, the resulting sum of the numerical fluxes from the refined cells up to level l is used in the lower level $l-1$ nonconforming neighboring cell with level $l-1$

2.4   Summary

The steps for the numerical method are summarized below:

1. Reconstruct the primitive variables on the cell faces following the 2nd order MUSCL scheme.
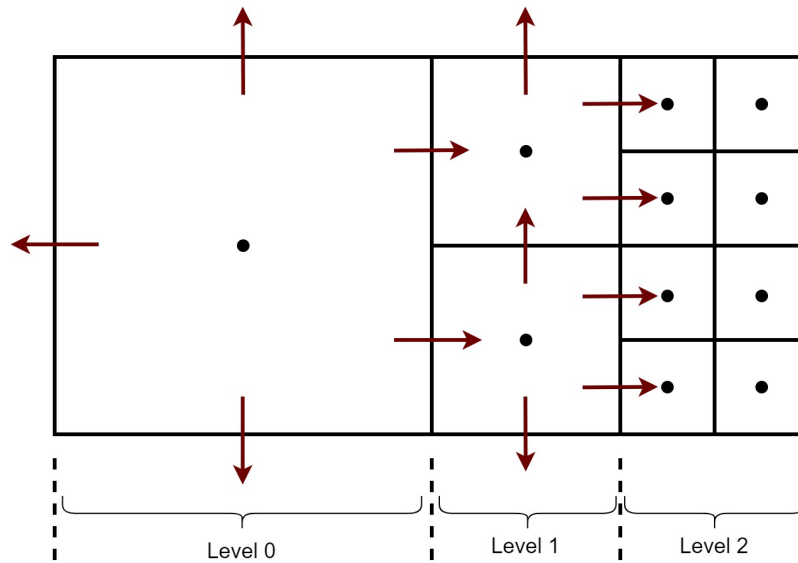
Figure 4: Non-conforming faces across 3 levels of refinement. With red arrows the numerical fluxes are depicted.

2. Half-time evolution, and relaxation/re-initialization steps.

3. Solve the Riemann problems at the cells' faces, with the help of the HLLC.

4. In the presence of a solid, check whether the interface has moved and if so, use the Ghost-fluid method to advect correctly the tangential velocities.

5. Using the relaxation step, compute the relaxed pressure.

6. Compute the p_{eq} from the total energy and re-initialize the internal energies.

7. Compute the criterion for refinement and adapt the mesh if needed.

8. Go to step 1 for the next time step.

2.5   Validation

In this section, 9 cases used for the validation of the numerical framework are illustrated. The chosen validation cases, are widely used in the literature in the framework of multi-material models.

2.5.1   Shock-Tube: Liquid/Gas

This validation case consists of a $L = 1m$ shock tube containing two regions, one of high-pressure water and one of low-pressure air, with zero initial velocities. This objective of this test case is to verify the fluid-gas part of the numerical solver. The interface is initially located at $x/L = 0.75$. The initial density of the water is $\rho_{water} = 1000 kg/m^3$, and the pressure is $p = 1 GPa$. The high-pressure region contains a small volume fraction of gas $a_{gas} = 10^{-6}$. The low pressure gas is at $p = 0.1 MPa$ with density of $\rho = 1 kg/m^3$. The parameters of the equation of state for the water are $\gamma_{water} = 4.4$, $\pi_{\infty,water} = 6 \; 10^8 Pa$ and for the air $\gamma_{air} = 1.4$, $\pi_{\infty,air} = 0 Pa$.

The numerical results Fig. 5 are in perfect agreement with the exact solution provided in the work of [148]. The initial mesh has 100 cells, and 4 levels of refinement are used with the resulting mesh at $t = 240 \mu s$ having 792 cells.
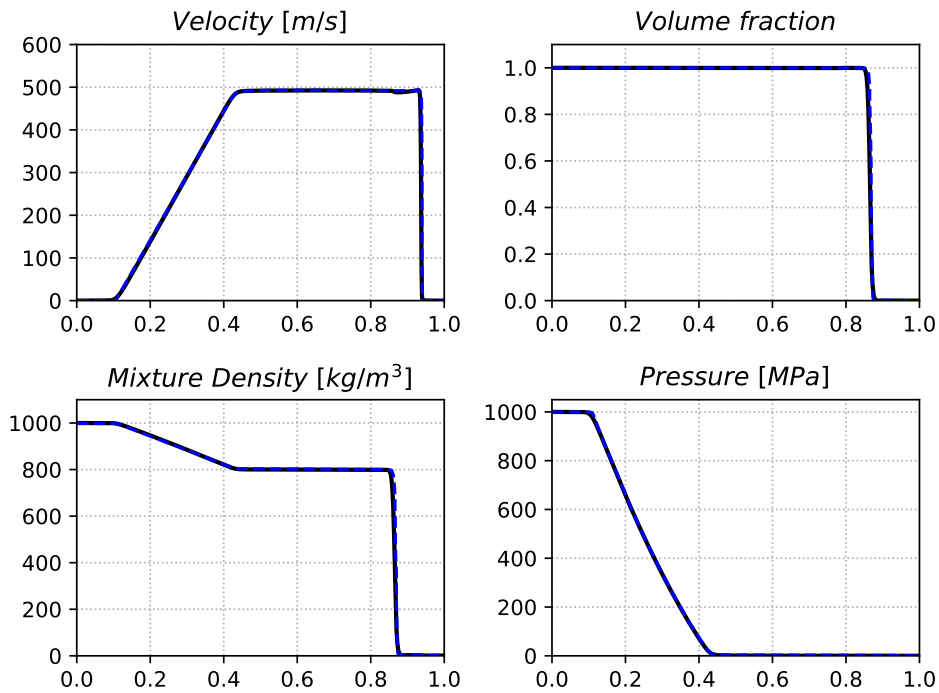
Figure 5: Shock-Tube case: High-pressure water, low-pressure gas. Black symbols represent the results from the presented solver, and the exact solution is shown with the solid blue line. Time: $t = 240 \mu s$

2.5.2   Cavitation test

The present validation case is composed of a $L = 1m$ long tube containing water with initial density $\rho = 1000kg/m^3$ at atmospheric pressure, with a small volume fraction of air present $a_{air} = 10^{-2}$. This objective of this test case is to verify the fluid-gas part of the numerical solver and the appearance of new interfaces. A discontinuity in the flow velocity is initially located at $x/L = 0.5$. The velocity of the left part is set equal to $u = -100m/s$ and the right part equal to $u = 100m/s$. The parameters of the equation of state are the same as in the previous validation case.

As the two halves are separated the pressure drops, resulting in the increase of the gas volume fraction and the appearance of two new interfaces. As it can be seen in Fig. 6 the solution is in agreement with the the exact [148]. The initial mesh used consists of 1000 cells, and the final one has 8446. Four levels of refinement were used.
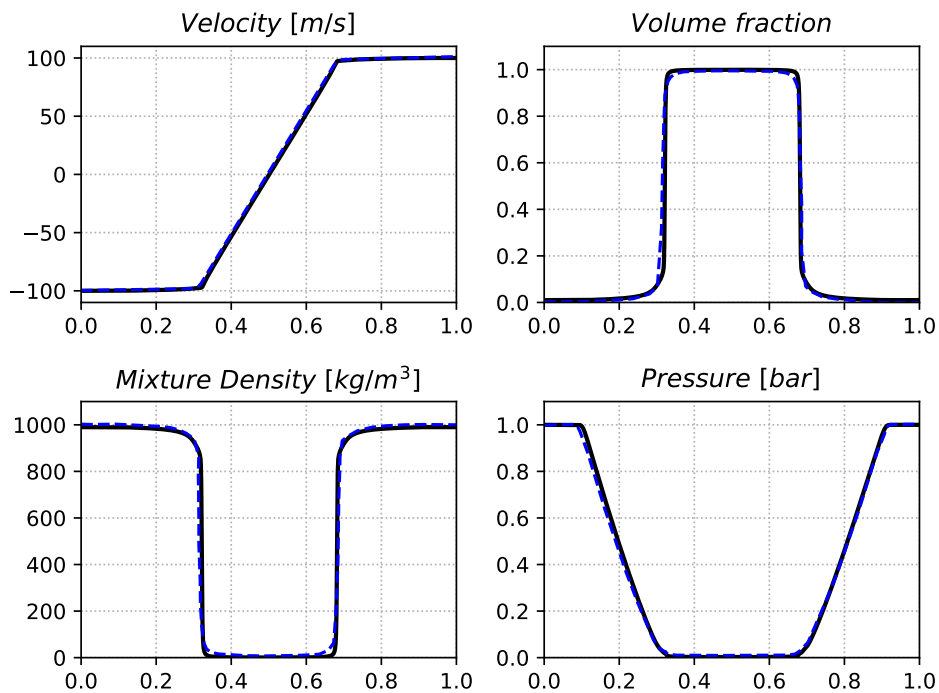
Figure 6: Cavitation test. Black symbols represent the results from the presented solver, and the exact solution is shown with the solid blue line. Time: $t = 1.85 \, [ms]$

2.5.3 Shock-Tube: Solid/Gas

A shock tube case with solid and gas with a high-pressure ratio is considered here. This objective of this test case is to verify the solid part of the numerical solver. The left part of the tube is filled with high-pressure copper and the right part with air at atmospheric pressure. The initial discontinuity is located at $0.6\,[m]$. The initial velocity is set to zero. The parameters of the equation of state for the copper are the following: $\gamma_{copper} = 4.4$, $\pi_{\infty,copper} = 6\ 10^8 Pa$, $\mu_{copper} = 9.2 \cdot 10^{1}0\ Pa$ and the initial conditions: $\rho_{copper} = 1000 kg/m^3$, $p = 5 \cdot 10^9 Pa$. The results presented below in Fig. 7 are in excellent agreement with the exact solution, proving the ability of the present solver to deal with high density and pressure ratios. The mesh used in this case is uniform and consists of 1000 cells.
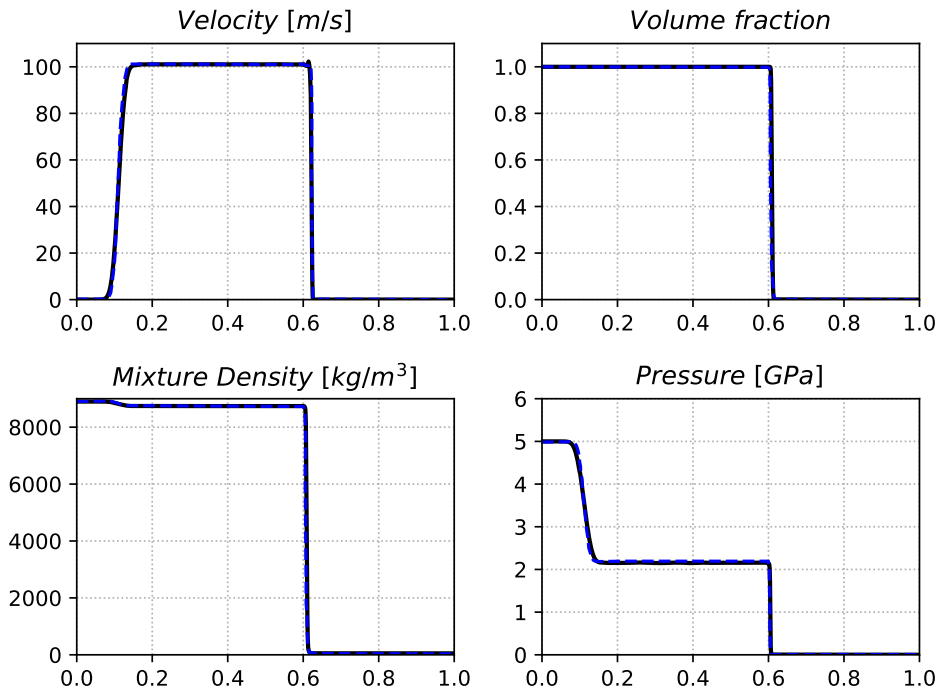
Figure 7: Shock-Tube: Solid/Gas. Black symbols represent the results from the presented solver, and the exact solution is shown with the solid blue line. Time: $t = 0.87\,[ms]$

2.5.4 Spherical bubble collapses in an infinite medium

The validation case presented in this paragraph corresponds to the high/low-pressure collapse of a gas bubble in water. A typical benchmark case that can be easily verified against simple one-dimensional semi-analytical models such as the Rayleigh-Plesset and the Keller-Miksis [74] equations. This objective of this test case is to verify the numerical solver can accurately

predict the bubble collapse dynamics. In both cases, viscosity and surface tension are not accounted for. The computational domain spans to a far-field distance equal to $L = 50R_0$ to avoid any boundary interference effects. The initial bubble radius for all cases is $R_0 = 1.0mm$. Symmetry boundary conditions were assumed in all boundaries, except the outer boundary of the domain, where an outflow boundary condition was imposed at the external face of the outermost cell. A grid independence investigation carried out resulted in a sufficient resolution of at least 35 cells for the initial radius. Similar findings were found in [149, 14]. Here the initial number of elements is 175 for the whole domain, with 50 corresponding to the initial bubble radius.

For the first case, a high-pressure ratio collapse at $p_l/p_g = 352$ is considered. The gas is considered ideal with $\gamma = 1.4$, $\pi_\infty = 0$ Pa, and the gas initialization pressure is considered as atmospheric $10^5 Pa$. For the low-pressure bubble collapse test case, a pressure ratio of $p_l/p_g = 20$ is assumed. In Fig. 8 we show the bubble radius evolution for both cases and are in excellent agreement, compared with the Keller-Miksis model. In particular, the high-pressure ratio results in a much faster collapse time and reaches a smaller rebound radius $\approx 0.35R_0$ due to the higher surrounding liquid pressure compared to the low-pressure ratio which reaches $\approx 0.97R_0$. The details of the initial value problem formulation for the Keller-Miksis model, along with the parameters for the cases can be found in [14]. The results from the Keller-Miksis model were obtained, by integrating the corresponding equation, using a third-order Runge-Kutta scheme with the same pressure ratios as in the numerical simulations.
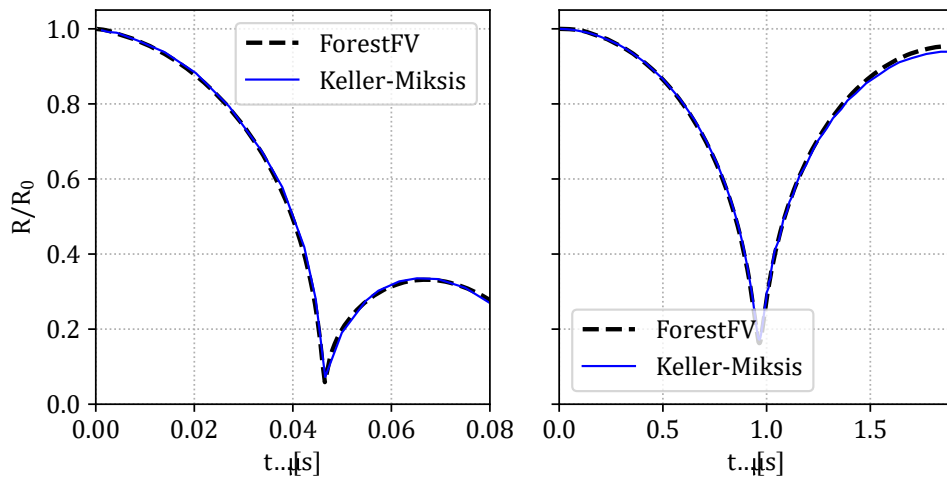
Figure 8: Temporal evolution of the normalized bubble radius for the symmetric gaseous bubble collapse and rebound test case validation. Dashed line: (- - -) ForestFV result. Solid line(——): Keller-Miksis model. **Left**: High-pressure ratio case. **Right**: Low-pressure ratio case. 50 cells were used for the initial bubble radius R_0.

	$\alpha\rho_1 \ [kg/m^3]$	$\alpha\rho_2 \ [kg/m^3]$	$u \ [m/s]$	$p \ [Pa]$
Post-Shock:	0	1.658	0	101325.0
Pre-Shock:	0	1.204	-114.49	159060.0
Bubble:	0.158	0.061	0	101325.0

Table 1: Shock-induced helium bubble collapse. Initial conditions and EoS parameters.
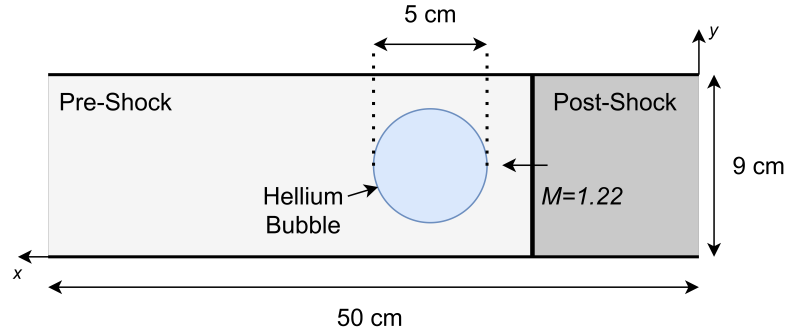
Figure 9: Initial configuration of shock-induced bubble collapse.

2.5.5   Shock-induced helium bubble collapse

A two-dimensional shock-induced bubble collapse is often used as a benchmark case for multiphase numerical solvers. This objective of this test case is to verify the multi-dimensional implementation of the numerical solver. The problem we consider here is the collapse of a helium bubble caused by a weak shock-wave in air, which was experimentally investigated by Haas and Sturtevant [57]. The configuration of the problem is shown in Fig. 9. Here we qualitatively compare our results against the experimental images. The initial conditions and the parameters of the equation of state are given in the table below.

The initial computational domain consists of 240000 cells. The interface of the bubble and significant pressure gradients are tracked using 6 levels of refinement. Only half of the problem is simulated, thus a symmetric boundary condition is used along the x axis and a reflective boundary condition is used along the top wall. Finally, inflow and outflow conditions are used for the remaining right and left edges of the computational domain. The results shown in Fig. 10 compare well to the shadowgraphs from the experiment of Haas and Sturtevant [57].
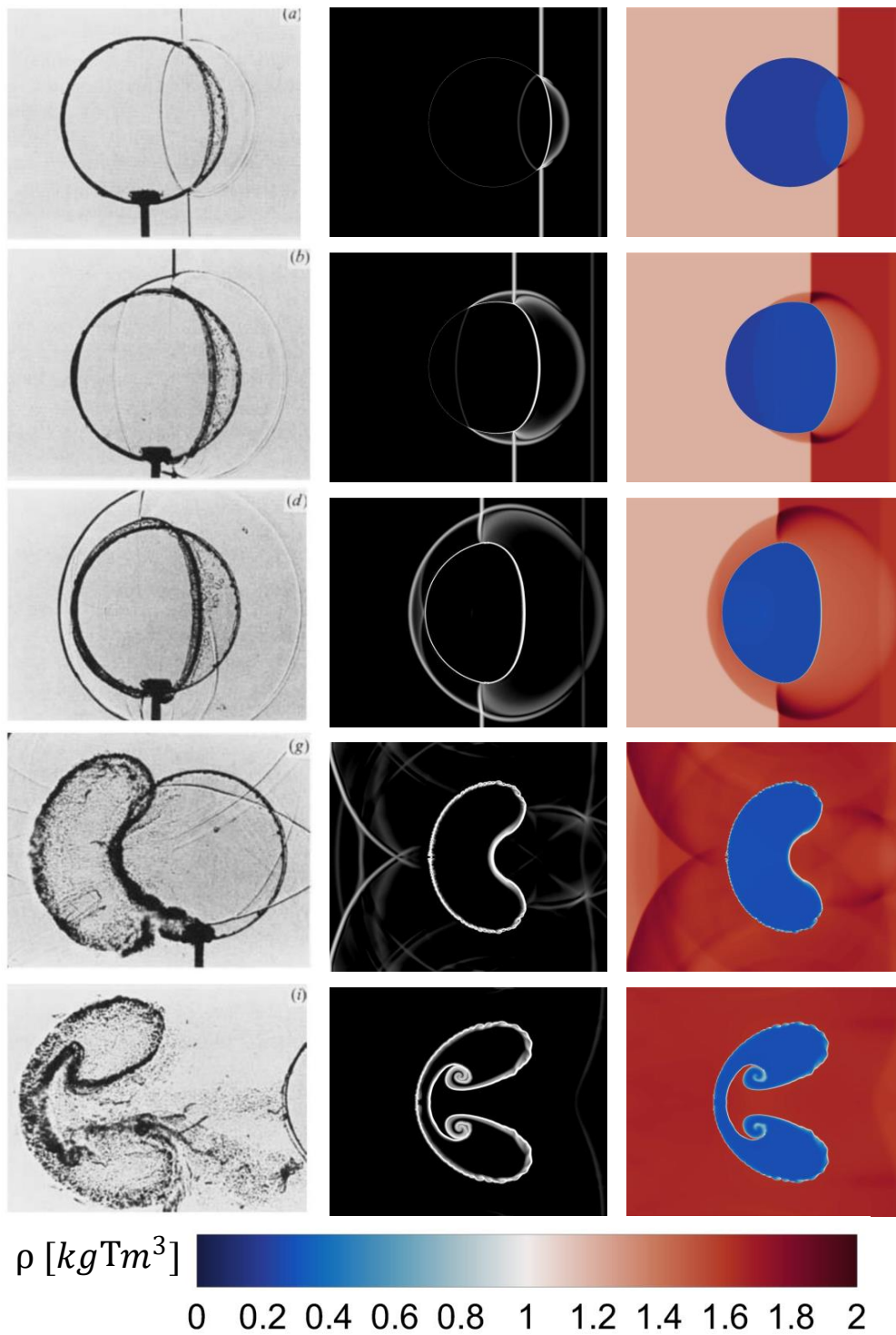
Figure 10: Shock-induced bubble collapse. **Left row**, shadowgraphs from the experiment of Haas and Sturtevant, **Middle row**, Schlieren images from the present solver **Right row**, density contours at times $t = 32 \ [ms]$, $t = 62 \ [ms]$, $t = 72 \ [ms]$, $t = 245 \ [ms]$, $t = 674 \ [ms]$

2.5.6   Richtmyer–Meshkov instability

The next two-dimensional benchmark case is a gas-water cavitating Richtmyer–Meshkov instability, initially proposed in Saurel et al. [148]. and Pelanti et al. [122]. In this test case, the ability of the solver in following dynamic interfaces is tested. The domain configuration is presented in Fig. 11 and is composed of two regions one with nearly pure water and one with nearly pure gas, being separated by a curved interface. The parameters of the equation of state and the initial conditions are given in the table below.

	$\rho\ [kg/m^3]$	$p\ [Pa]$	$u\ [m/s]$	$\pi_\infty\ [Pa]$	γ
Liquid:	1000.0	101325.0	-200	$6\cdot10^8$	4.4
Gas:	0.0495	5066.0	-200	0.0	1.4

Table 2: Richtmyer–Meshkov instability. Initial conditions and EoS parameters.

The computational domain is composed of 25000 cells. Similar to the shock-induced collapse of the helium bubble, we track the interfaces and significant pressure gradients using 4 additional levels of refinement. The bottom, top, and right boundaries are considered walls thus a reflective boundary condition is applied, whereas the left boundary is outflow. Only the top half is simulated, thus a symmetric boundary condition is used along the x axis.
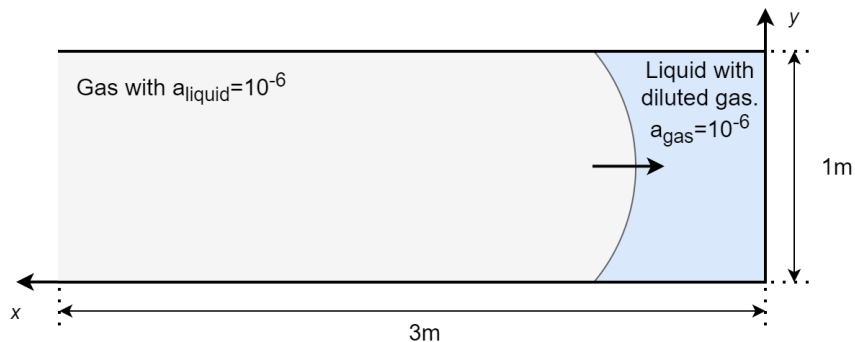
Figure 11: Initial configuration of Richtmyer–Meshkov instability.

The flow impinges the right wall creating a shock wave which then impacts the curved interface. This interaction produces the Richtmyer–Meshkov instability depicted in 12. New interfaces dynamically appear near the right boundary due to expansion waves. Cavitation pockets also appear on the right boundary due to pressure drop. Finally the characteristic elongated jet of Richtmyer–Meshkov is formed. Our results closely match those of [148],[122].
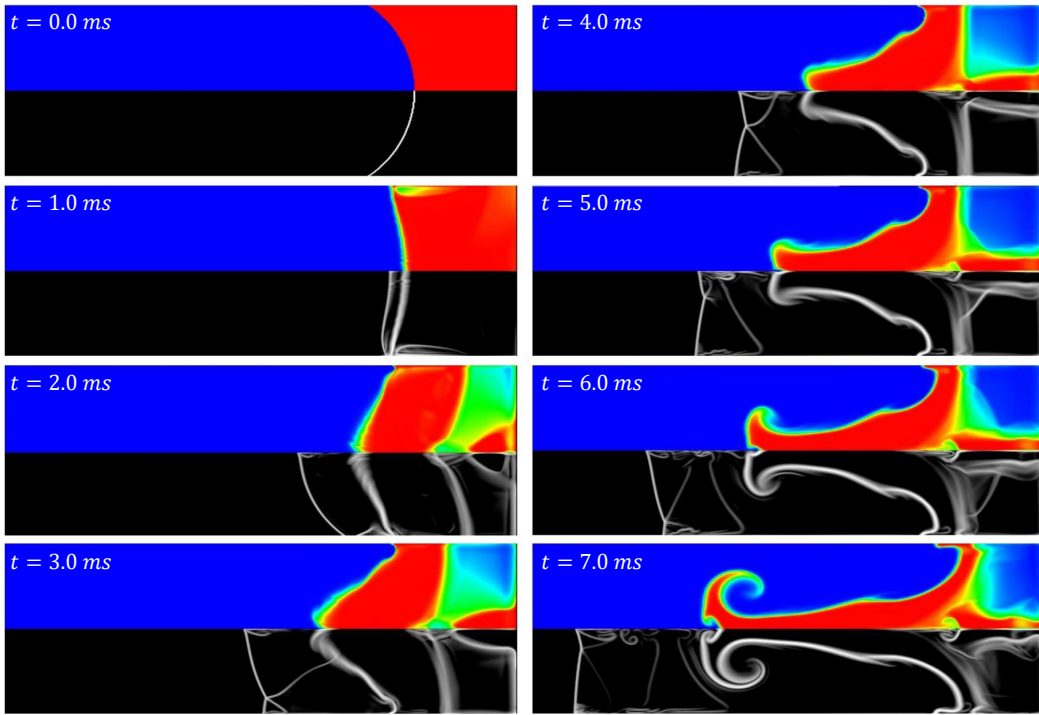
Figure 12: Richtmyer–Meshkov instability. **Bottom half** presents Schlieren images of each time frame, **Top half** volume fraction of water.

2.5.7 Wave transmission across a solid/fluid interface

The first validation case presented here is a 2-D problem of a pressure wave impacting a planar fluid-solid interface. The objective of this case is to verify the fluid-structure interaction and the correct prediction of the transmission and reflection of the pressure wave across interfaces. The configuration of the case is presented in Fig. 13. A square with edges of 40 mm is considered with the top half being the fluid-subdomain, and the bottom half solid.

A spherical high-pressure region at 10 kPa higher than the ambient, is considered within a fluid region. The pressure around this high-pressure region smoothly transitions to the ambient following a tangent function distribution as described in [35]. This configuration replicates a pressure wave, similar to one that is emitted during a bubble collapse. The initial condition for the pressure across the fluid is given by:

$$p = p_0 + \beta\Big(1 - \alpha\Big(\tanh(2\pi(2\beta r - \alpha)) + 1\Big)\Big) \tag{35}$$

where r is the distance from the source, p_0 is the hydrostatic pressure and α and β are scaling
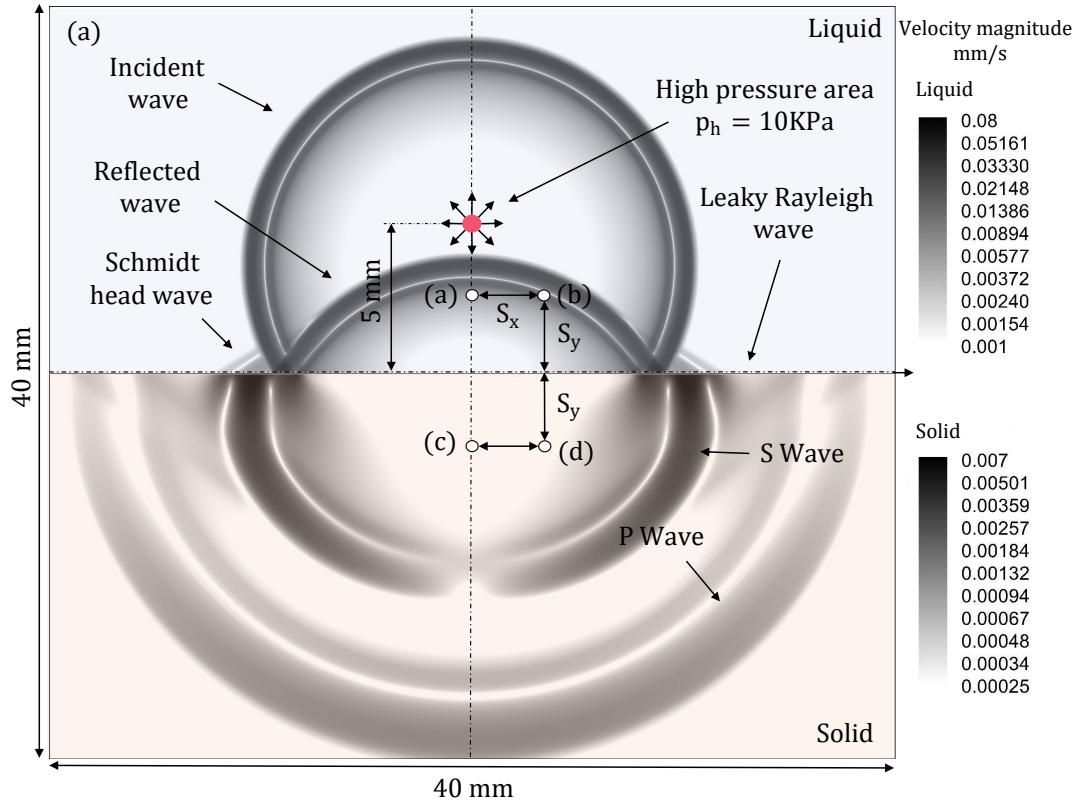
Figure 13: Wave propagation across a fluid-solid interface case setup and velocity magnitude distribution. **Top half**: fluid region, **bottom half**: solid region. (a)-(d) pressure sensors with $S_x = S_y = 2.5mm$. The initial area of high pressure $(10KPa)$ is denoted with red. Wave structure in the fluid region consists of the incident wave, the reflection, and the Schmidt head wave. In the solid region S/P and leaky Rayleigh waves.

parameters equal with 0.5 and 1000, respectively. The initial position of the high-pressure area is located $5.0mm$ above the solid/fluid interface. The initial condition for the velocity field as provided by the acoustic theory [25] is initialized as:

$$u = \frac{p - p_0}{\rho c_0} \; , \tag{36}$$

where c_0 is the speed of sound of water and ρ the density. The parameters of the equation of state for water is $\rho = 1000.0 \; kg/m^3$, $\pi_\infty = 6.0{\cdot}10^8 \; Pa$, $\gamma = 4.4$. For the solid $\rho = 8900.0 \; kg/m^3$ $\pi_\infty = 342.0 \cdot 10^8 \; Pa$, $\gamma = 4.22$, $\mu = 9.2 \cdot 10^{10} \; Pa$ which corresponds to the properties of copper.

The computational mesh consists of a total number of 12.8 million hexahedral elements. The characteristic element size is uniform and equal 10 μm throughout the Eulerian field and the time-step is held constant at 0.5 ns for the entirety of the simulation.

Fig. 13 presents the velocity magnitude for the numerical solution at a time instance where the high-pressure wave has impacted the interface and has propagated inside the solid. The velocity magnitude colormap scale is adjusted to the different characteristic values of the maximum velocity in the solid and the fluid. The reflection of the pressure wave can be clearly seen in the fluid region, alongside the incident wave, which propagates outwards. In the same figure, the transmitted longitudinal P waves and transverse S waves can be identified in the solid phase region. The generation of surface waves, emanating from the interface is also apparent, with Schmidt head waves in the fluid region and leaky Rayleigh waves in the solid. A similar wave structure is reported in [183]

To validate the developed numerical solver, the same case is simulated with a linear acoustic model that accounts for homogeneous fluids and elastic solids. This is accurate due to the small magnitude of the incident pressure wave, and the absence of solid deformation. The solution to this problem thus can be simulated by K-Wave [45] which employs such a model and has been validated against numerous other wave propagation problems [162]. In Fig. 14, the pressure time-series is given for two sensors (a),(c) located at (0,2.5)mm and (0,-2.5)mm, alongside the numerical solution of K-Wave. The two solutions are in close agreement, with minor differences of less than 1% in magnitude.
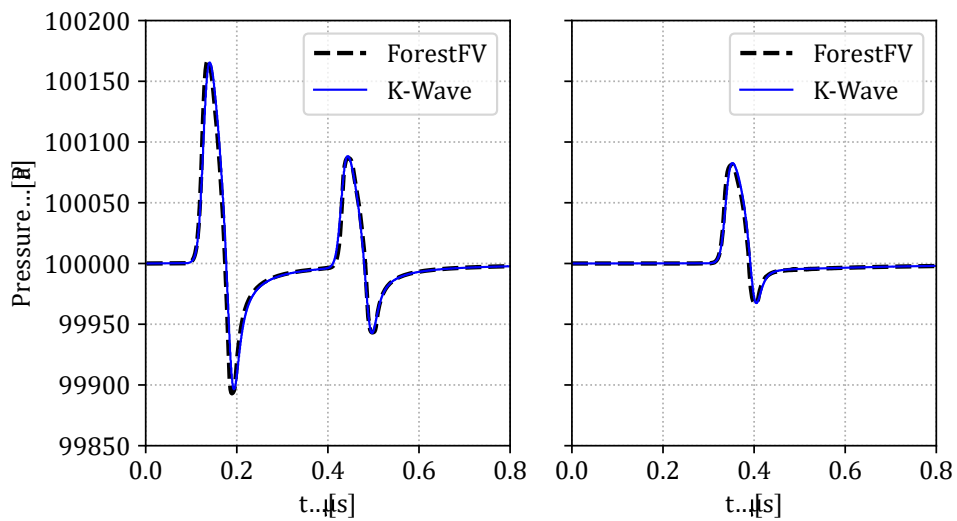
Figure 14: Comparison of numerical solution of the wave transmission across a fluid/solid interface, using the developed ForestFV solver presented in this paper and the K-Wave [163] linear elastic-acoustic model. **Left**: Pressure time series at probe point (a) (0,2.5)mm. **Right**: Pressure time series at probe point (c) (0,-2.5)mm

2.5.8   Shock induce bubble collapse close to a wall

Finally, to validate the resolution of the shock-induced bubble collapse dynamics, the validation case first presented in [68] and later in [174] is considered. This case is composed of a gas bubble collapsing after the impact of a lithotripter's shock wave (LSW). The gas bubble has an initial radius $R_0 = 0.05mm$ and is at a distance $S/R_0 = 2$ from the wall. The surrounding media is water with the same properties as defined in the previous cases. The lithotripter pulse can be fitted from experimental data [29], with $p+$ and $p-$ equal to $35MPa$ and $-10MPa$ respectively. The pulse is modeled as planar given that a typical focal width FW is much larger than the radius of the bubble FW/R_0 200.:

$$p(t) = p_0 + 2p_s e^{-\alpha t} cos(\omega t + \pi/3) \ , \tag{37}$$

where $\alpha = 1.48 \cdot 10^6 s^{-1}$, $\omega = 1.21 \cdot 10^6 s^{-1}$ are equal to the parameters values used in [68] and the maximum over-pressure is $p_s = 35MPa$. The pulse is introduced into the domain by modifying the initial conditions for the pressure, total energy, and velocities according to the acoustic theory [25]. The rest of the domain is initialized with atmospheric pressure and zero velocity.

The computational domain is presented in Fig. 15. Due to the symmetry of the problem around the z-axis, the computational domain consists of a 2° degrees wedge type mesh. Symmetry boundary conditions are assumed at the limiting planes while the out-most boundaries are modeled by outflow conditions. The rigid wall was modeled using reflective boundary conditions. The initial mesh consists of 125,000 elements. A grid convergence study was carried out with uniform and local mesh refinement up to 2,3 and 4 levels respectively. The resulting meshes have 0.5,2 and 8 million cells for the uniform re-meshing, whereas the local refinement is focused on the bubble interface and on significant pressure gradients, leading to at most 0.5 million elements. The results show (Fig. 16) that the local mesh refinement preserves the bubble's interface in the same as in the uniform meshes. Additionally, the pressure loss due to numerical diffusion is minimized, with the 4-level AMR run having less than 5% difference from the 3 levels of uniform refinement. Thus, the strategy that was employed for this simulation is a combination of 2 levels of uniform refinement in the area close to the bubble with additionally two more levels on the interface and in the proximity of significant pressure gradients.

To compare and validate the present methodology, two pressure sensors are assumed along the wall. The sensors are located in the same radius from the center-line as in [174, 68] i.e
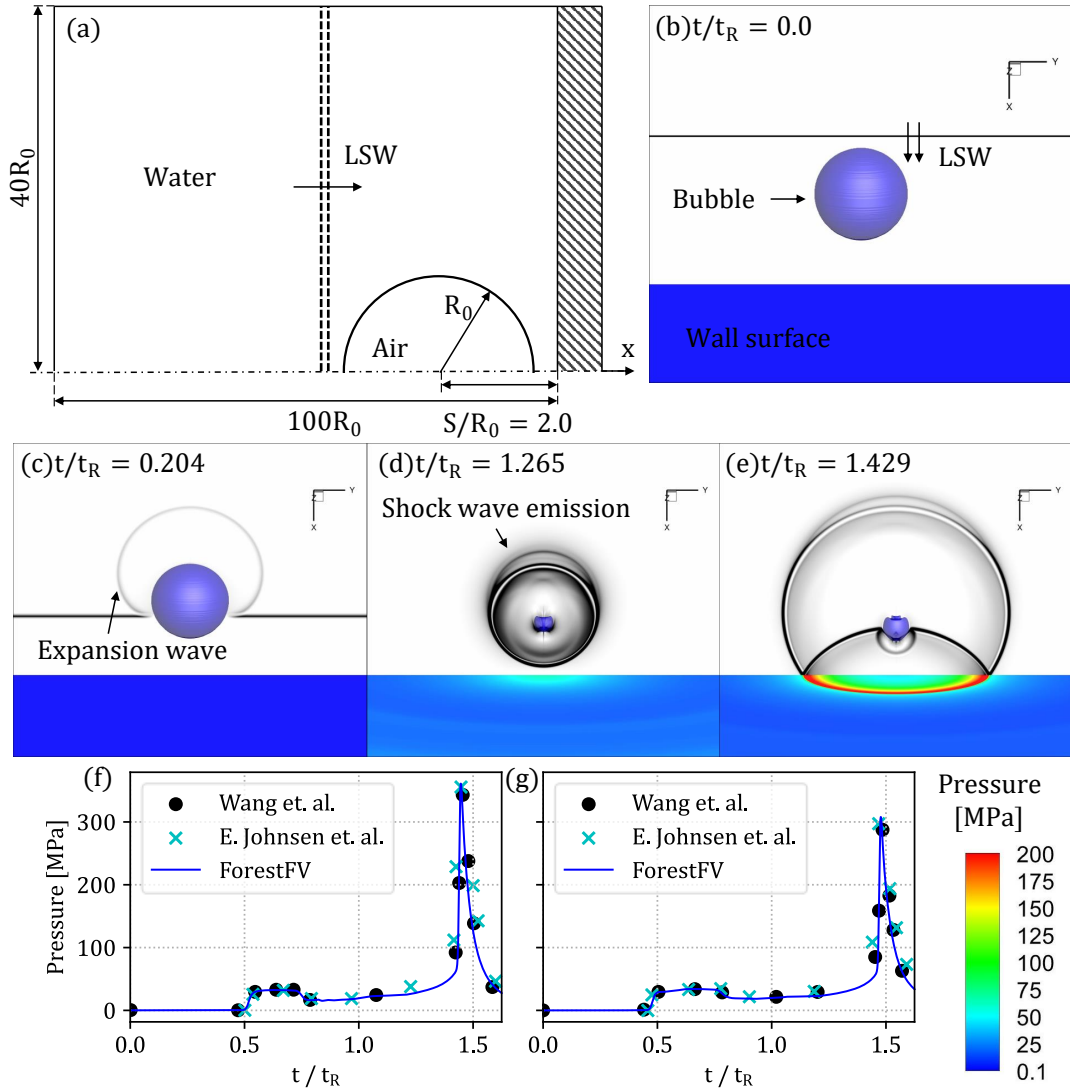
Figure 15: Shock-induced gas bubble collapse near a wall with stand-off distance $S/R_0 = 2$. (a) Case configuration. (b) Initial conditions. (c) $t/t_R = 0.204$, (d) $t/t_R = 1.266$, (e) $t/t_R = 1.429$, gray-scale colormap: magnitude of the pressure gradient, blue iso-surface: bubble interface, rainbow colormap: pressure distribution on the wall surface. (f) Pressure time series probed at $r/R_0 = 0.0$, (g) pressure time series probed at $r/R_0 = 1.0$, pressure time series comparison between the present results with ForestFV and published results in [68] and [174].

$r/R_0 = 0$ and $r/R_0 = 1$. The time history of the pressure evolution at those probing stations is presented in Fig. 15(f and g). The first spike in pressure is the result of the LSW impacting the wall. The small time delay in the two sensors is due to the shielding effect of the bubble. After the reflection of the LSW of the wall, the bubble is loaded even more from the right side, accelerating the collapse. The bubble collapses and emits a shock wave which reaches a ratio of $p/p_s = 10$. As shown in Fig. 15 a liquid jet forms from the distal side and towards

the wall which finally results in a bubble that presents the classical pattern of the near-wall collapse toroidal shape and a vortical structure that stretches the bubble radially towards the wall [120]. The recorded time series of pressure are in good agreement with those reported in [174, 68], with a less than 10 % difference in the peak pressure, at both sensors.
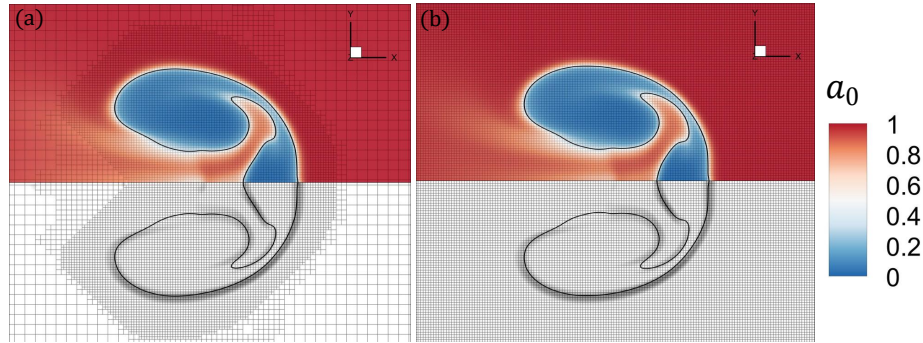
Figure 16: Shock-induced bubble collapse close to a rigid wall. Colormap: volume fraction (α_0) contour of water. Gray-scale: density gradient magnitude. Black iso-surface: bubble interface. **Left**: AMR with 3 levels of refinement on the interfaces, **Right**: Uniform refinement with 3 levels.

2.5.9 Stress development within kidney stones

The last validation case presented here is a shock wave impact on a kidney stone mimicking material submerged in water. The objective of this case is to qualitatively compare the numerical results with the photoelastic images from the experimental work of Xi and Zhong [179] and thus to verify the wave transmission across the interface and the evolution of the transient stress field in solids during shock wave lithotripsy. The case's configuration is presented in 17a(i). The kidney stone modeled in this study is similar to the phantom used in the experiment with a rectangular cross-section $14x14mm$. The material used was plaster-de-Paris, which has similar properties to struvite stones. The parameters of the equation of state are calculated by matching the acoustic impedance and speed of sounds of the phantom similar to the work [80]. These are equal to $1500.0MPa \cdot s/m$ for water and $2866.95MPa \cdot s/m$ for the kidney stone. The lithotripter pulse is fitted from experimental data [179, 174, 68] with $+p = 46.7MPa$ and $-p = 5.44$. The pulse is introduced into the domain by modifying the initial conditions for the pressure, total energy, and velocities according to the acoustic theory [25]. The rest of the computational domain is initialized with atmospheric pressure and zero velocity.

The initial computational mesh consists of 120,000 elements. Three levels of mesh refinement are used in the kidney stone and the solid-fluid interfaces. The traveling pressure waves
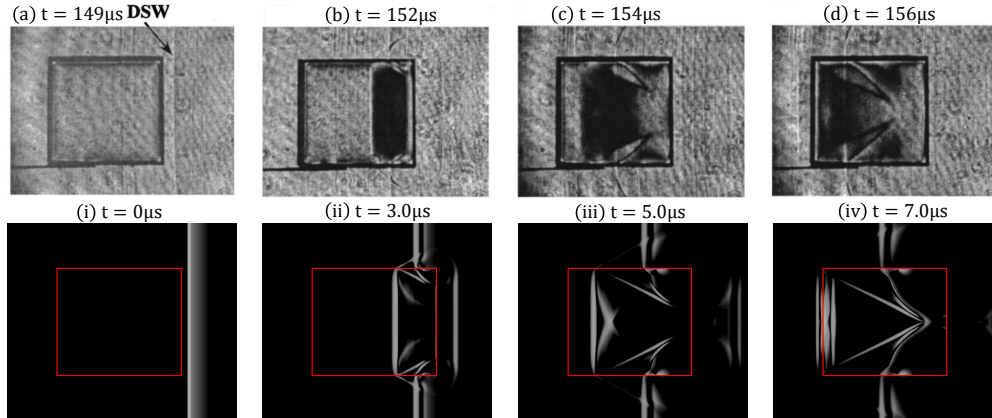
Figure 17: Qualitative comparison of a shock impact to a kidney stone phantom with photoelastic imaging. **Top:** Experimental work of Xi and Zhong [179] **Bottom:** Numerical results, contours depicting gradient of principal tensile stress.

are also resolved with three levels of mesh refinement. The minimum cell size reaches $18\mu m$. Due to the planar nature of the problem, only a 2D slice was simulated. Outflow boundary conditions are applied to the outermost boundaries.

In Fig. 17 a qualitative comparison between the experimental data from [179] and the simulation is presented. On the top row, the photoelastic images are presented, which are indicative of the stress development inside the material. On the bottom row the numerical results of the gradient of the maximum principal tensile stress.

The left image depicts the initial configuration at the time when the incident shock wave is about to impact the kidney stone. It should be noted that the gradient of the principle tensile stress in the fluid region corresponds to the pressure gradient. When the LSW impacts the stone, a pair of planar P wave-fronts are created, one towards the inner part of the kidney stone and one reflected in the fluid region. Wave diffraction occurs at the boundary of the stone as the width of the beam is wider than the diameter of the stone. Thus, two S waves are generated at an oblique angle and propagate towards the center of the stone. This can be seen in 17(b)-(d) and (ii)-(iv). Because the longitudinal speed of sound is greater than the transverse speed of sound $2493m/s$ and $1108m/s$ respectively, the P wave will lead followed by the transverse waves. $P-head$ waves will be generated as the incident shock wave travels along the outer boundary of the stone when the critical angle is reached. Finally, the leading P wave will be reflected at the distal face of the stone and will propagate towards the proximal face, reaching the S-waves. The superposition of those reverberating stress waves leads to a maximum stress. The location of the peak pressure is affected by the speed of the longitudinal and transverse waves, thus for each different type of kidney stone, the results will significantly

differ. The numerical results are in close agreement with the photoelastic images.

2.5.10 Qualitative comparison of bubble soft tissue interaction

The case presented in this section concerns a qualitative comparison of a shock-induced bubble collapse simulation, close to a gelatin surface, against the experimental work of Kodama et. al [82]. In this study, 3-D configurations are examined with various stand-off distances and bubble sizes. For validation of the presented model, the smallest bubble was selected as it is more relevant to the bubble sizes present during shock wave lithotripsy. The bubble's radius is equal to $R_0 = 0.21 mm$ and placed at a stand-off distance equal to $S/R_0 = 1.1$ from the gelatin surface. The lithotripter pulse profile is recorded in the experimental study and the characteristic overpressure has an aptitude of $ps = 10.2 + -0.5 MPa$. The initial incident pulse is placed at $1.25 R0$ upstream of the bubble's center. The parameters of the EoS for the gelatin are computed by matching the acoustic impedance and speed of sound based on those given in [82] and they are; $\rho = 1060.0 \ kg/m^3$, $\pi_\infty = 0.69 \ GPa$, $\gamma = 4.3$, and $\mu = 1.0 \cdot 10^3 \ Pa$. The surrounding medium is water and shares identical properties as specified in the previous case.

The computational domain is similar to the one used in [85]. Initially, it consists of 125,000 elements, four additional levels of mesh refinement were used to preserve sharp solid-fluid-gas interfaces, and significant pressure gradients. Two levels of mesh refinement were used around the area of the collapse, forming a circular area and thus preserving the various flow features, such as the velocity and density fields.

The impact of the incident shock wave on the distal side of the bubble accelerates the bubble wall and sets the motion for the asymmetric bubble collapse. Due to the difference in the acoustic impedance between the gas content and the surrounding water, an expansion wave forms, traversing upstream from the bubble. The incident shock wave impacts the gelatin surface, with minimal reflection due to the small relative difference in acoustic impedance. The deformation of the gelatin surface induced by the impact of the incident of the shock wave is negligible, compared to the deformation that the liquid jet will later induce. A sink flow around the bubble is formed in Fig 18(i) during the initial stages of the collapse, which leads to an upward motion of the gelatins' surface; in Fig 18(1) this is not apparent as the resolution of the experimental images is not sufficient to depict such movement. During the initial collapse phase, the distal bubble interface has gained enough momentum and is rapidly collapsing towards the proximal interface, resulting in increased pressure.
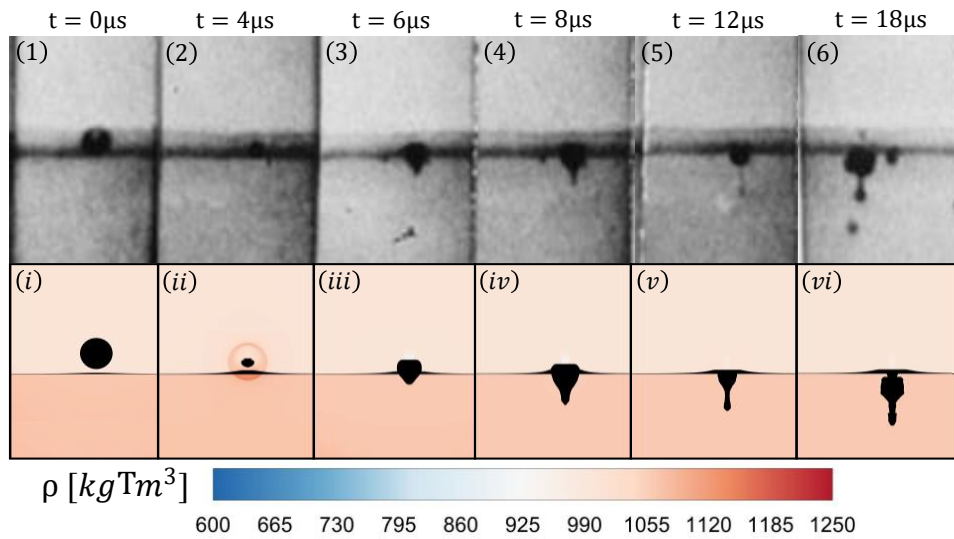
Figure 18: Qualitative comparison of shock-induced bubble collapse close to a gelatin surface. **Top:** Experimental work of Kodama et. al [82] **Bottom:** Numerical results, grey colormap: density distribution, with black isosurface of bubble and gelatin interface.

The collapse happens after $t \approx 4\mu s$ the impact of the shock wave and is depicted in Fig. 18(2) and (ii). The two opposing moving liquid flows, at the upper and lower interfaces of the bubble impact, thus resulting in the emission of a water hammer shock wave. Both the experimental and the numerical results demonstrate the same mechanism. The resulting liquid jet impacts the gelatin surface and starts deforming the gelatin, while high normal and shear stresses are developed in the contact area. Following the initial collapse phase, the formation of the liquid jet resulted in the penetration of the gelatin surface. The bubble at this stage has taken a toroidal shape with two distinct regions. The upper torus, which is initially expanding within the gelatin, and a long neck-like structure, which is composed of toroidal gas pockets that are transported by the fast liquid jet. The pressure differential of the expanding toroidal structure is eventually reversed and the surrounding gelatin and liquid, force the gas pockets to a secondary collapse (see Fig. 18(5) and (v)). In both the experiment and the simulations, the direction of the collapse and the subsequent formation of the liquid jet is governed by the shock impact on the bubble wall and leads to the jet forming towards the solid interface.

3 Shock-induced bubble collapse during SWL

3.1 Background

Experimental and computational studies have shown that the collapse of a bubble is not spherical for non-symmetrical configurations such as in the proximity to a rigid surface, or a free boundary of a deformable solid or neighboring bubble [91]. The bubble dynamics close to rigid or soft surfaces can be affected by multiple factors. Lauer et al. [90] reported on the symmetry of the collapse mechanisms of detached and attached bubbles to rigid walls. Koukouvinis et al. [86] expanded on this mechanism by highlighting the influence of the angle of attachment between the near-wall liquid/vapor interface with the wall. For attachment angles greater than 90°, the collapse is focused away from the wall, resulting in the "*jetting and wall hammer*" effect. In contrast, for angles smaller than 90°, the collapse is driven by a local pressure increase in the circumference of the bubble leading to the shape of the bubble at the collapse resembling a pin-like structure. This pin-type structure is also reported in the work of Kyriazis et al. [89]. Trummler et al. [164] showed the influence of stand-off distance on jet formation, rebound, and maximum wall pressures, as well as the importance of grid resolution on peak pressure estimation. Even though the above-mentioned studies utilized different numerical models and assumptions, they predict a similar collapse behavior, due to the common inertia-driven mechanism of the phenomenon. The collapse dynamics of attached bubbles to soft solids, however, still remain not fully understood.

In this chapter, we aim to expand on previous studies by investigating the collapse dynamics in the vicinity of deformable solids by modeling them as elastic solids. For this, we have performed and presented a limited number of shock-induced bubble collapse simulations of detached and attached bubbles in the proximity of bio-materials for the first time. Specifically, three configurations were investigated. The first corresponds to a detached gas bubble with an initial stand-off distance of $S/R_0 = 1.2$ to the solid boundary collapsing under the effect of a lithotripter pulse, commonly used in numerical and experimental studies [68]. The second and third configurations correspond to bubbles attached to the solid surface with stand-off distances equal to $S/R_0 = 0.6$ and $S/R_0 = -0.2$ respectively. The solid materials selected for this computational study are a uric acid type kidney stone and a soft tissue, with properties close to those of liver tissue. The results reveal the detailed collapse dynamics, jet formation, solid deformation, rebound, primary and secondary shock wave emissions, and secondary collapse that govern the near-solid collapse and penetration mechanisms. Significant correlations of the problem configuration to the overall collapse mechanisms were found, stemming from the

contact angle/attachment of the bubble and from the properties of solid material. It should be noted that only one shock wave profile and bubble size were considered, thus limiting the generality of the conclusions. Our aim is to expand on previous studies by revealing the complex fluid-solid interactions of these bubbles, i.e.: how they deform the surface of kidney stones and how they penetrate and damage soft tissues.

3.2   Results and Discussion

In this section, we present the collapse dynamics of a gas bubble for varying stand-off distances and attachment configurations (see Fig. 19) for two different solids materials relevant to shock-wave lithotripsy, and the results are discussed and compared with similar findings in the literature. The first material studied is a uric type of kidney stone (KS), a common type formed in human kidneys. The material properties of the KS are taken as: $\rho = 1546.0\ kg/m^3$, $\pi_\infty = 8.37 \cdot 10^9\ Pa$, $\gamma = 1.7$, $\mu = 3.0 \cdot 10^9\ Pa$. To investigate tissue damage during shock-wave lithotripsy, a soft tissue material is also studied with the following properties: $\rho = 1060.0\ kg/m^3$, $\pi_\infty = 1.43 \cdot 10^8\ Pa$, $\gamma = 4.3$, $\mu = 1.0 \cdot 10^3\ Pa$. The properties of this second material are akin to the properties of human liver tissue. Following the approach of Kobayashi et. al. [80], the parameters for the equation of state for the soft tissues and the kidney stone, are calculated by matching the acoustic impedance and the speed of sound. In the work of Bailey et al. [8] it was found that bubbles nucleate following the passage of the lithotripter pulse, in the renal collecting system and more precisely in urine. Thus, the surrounding medium was modeled as fluid to simulate urine.

In the analysis presented in this thesis, three distinct stand-off distances S of the bubble's center to the surface of the solid are considered. In the first configuration the bubble is not attached, i.e $S/R_0 > 1$ (see Fig. 19). In the second configuration, the bubble is attached to the solid with an acute angle, i.e. $1 > S/R_0 > 0$, and finally, a closely attached configuration where an obtuse angle of attachment is considered, i.e. $S/R_0 < 0$. The initial size of the bubble is $R_0 = 0.04mm$ which is a typical radius for bubbles formed during shock-wave lithotripsy. From a purely numerical viewpoint, the parametric study of Wang [174] addressed the question of the bubble size that collapses during the passage of a single shock wave pulse. It was found that bubbles larger than $R_0 > 0.13mm$ do not collapse in the time frame of the shock wave propagation across a kidney stone with a size $1.5mm$. It should be noted that the same shock wave intensity and profile was used thus the result from that study should hold for our cases. In principle, larger bubbles will tend to take longer to collapse. Similar findings were reported in the work of Sankin et al. [145]. Additionally, in the work Philipp et al. [126] it is stated that
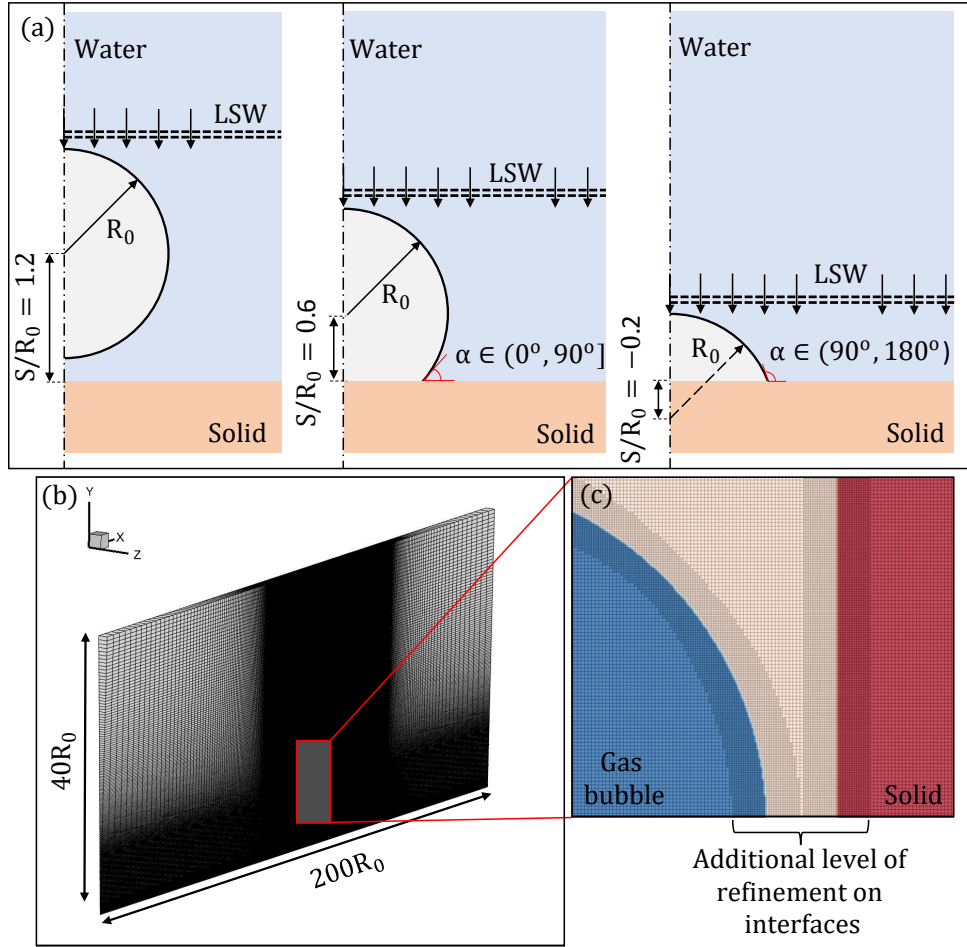
Figure 19: Shock-induced gas bubble collapse case configurations. (a) Types of bubble attachment on the solid surface based on the angle α (b) Computational domain. The initial ancestral mesh consists of $125K$ elements, (c) Detail of Gas/Liquid/Solid interfaces, additional levels of refinement on the bubble and solid interfaces

after the shock impact the bubble wall will accelerate to twice the material velocity behind the shock front. An explicit correlation between the bubble size and the jet velocity, however, was not identified. The same behavior is apparent in our findings as well. A bubble size was established in the work of Philipp et al. [126] that characterizes the intensity of the bubble rebound in relation to the shock wave profile, as the collapse might be hindered by the tensile part of the shock wave.

In our study, we did not observe such mechanism for the initial collapse as the shock impact set in motion the collapse of the bubble. This mechanism, however, can indeed play a role in the secondary bubble expansion. For all cases, the same shock wave, as in the validation case presented in subsection 4.3 is considered. The shock is modeled by its corresponding spatial pressure distribution in the initial conditions of the simulation and is positioned at a

distance $d/R_0 = 1.25$ away from the bubble's center. The rest of the domain is initialized with atmospheric pressure and zero velocity.

The axis-symmetric configuration of the problem, allows the use of an unstructured hybrid computational grid for a 2° sector of the computational domain. The initial ancestral mesh consists of 125.000 hexahedral and prismatic elements. The assumption of symmetry greatly reduces the computational cost and enables a higher resolution on the solid-fluid-gas interface dynamics, which otherwise would elude. In principle, however, there are two distinct processes that cannot be investigated under this assumption. The first is related to the shock wave alignment to the bubble and solid interfaces. In the work of Johnsen et al., [69] and Coralic et al. [33], it is stated that the shock will dictate the direction of the collapse and the jet formation. Thus, a relative angle of 0 degrees, i.e., the symmetry assumption, leads to the most energetic collapse and is the most detrimental for vessel damage which is the case under investigation in this work. The second is that inherently the bubble collapse dynamics are fully three-dimensional processes. Theoretical studies [132] have suggested that during the collapse and rebound phases, bubbles do not remain spherical. The loss of sphericity has been reported by many authors [149, 68], and can be attributed to Rayleigh-Taylor and shape instabilities. A numerical study that embodies the assumption of symmetry [69], however, presents a good agreement with experimental results. More precisely it is stated that the location of the collapse does not vary significantly, although wall pressure might be overestimated by the simulations. This was attributed to the infinite acoustic impedance used in that study. Later work by Wang [174], revealed that when modeling an elastic solid with a finite impedance, the overestimation of pressure is substantially lower by 60% to 90%. Thus, the assumption of symmetry can have applicability, with future three-dimensional studies to fully investigate the aforementioned aspects of bubble dynamics.

A mixed refinement strategy, similar to the one discussed in subsection 2.5, was used. The interfaces were resolved using 4 levels of refinement and significant pressure gradients, while 2 to 3 levels of refinement were used in the area around the collapsing bubble. The final dynamic mesh reaches a maximum of 1 million cells during the collapse of the bubble. An equivalent uniform mesh would have resulted in a prohibitive mesh size of two orders of magnitude more cells for the resolution of the dynamically developing interfaces. The time step was adjusted so that CFL would not exceed 0.1, thus, ensuring numerical stability and the convergence of the pressure relaxation procedure.

To facilitate the comparison of the various cases presented in this work, the results are presented as nondimensional values. Specifically, time is non-dimensionalized against the

Rayleigh collapse time t_R,

$$t_R = 0.915 R_0 \sqrt{\frac{\rho_l}{\Delta p}} \, , \tag{38}$$

where R_0 is the initial radius of the bubble ρ_l is the fluid density of the surrounding liquid and Δp is the pressure difference between the two fluids [130]. Similarly, the velocities and pressures scales are normalized as in, [164]:

$$p_c = \rho_l c_l^2, \quad u_c = \sqrt{\frac{\Delta p}{\rho_l}} \, , \tag{39}$$

3.2.1 Detached bubbles: $S/R_0 > 1$

The impact of the incident shock wave on a detached bubble near a Kidney stone is presented in Fig. 20. The initial configuration of the simulation is presented in Fig. 20a with an initial stand-off distance of $S/R_0 = 1.2$. The incident shock wave is initially placed at $1.25 R_0$ upstream from the bubble's center. At the instance $t/t_R = 0.127$ the shock has impacted the bubble, resulting in the formation of an expansion pressure wave due to the difference in acoustic impedance between the gas content of the bubble and the surrounding water. The impact of the shock wave increases the pressure of the liquid around the bubble, Fig. 20b, inducing the asymmetric collapse of the bubble [20].

In the last two instances presented in Fig. 20,(c-d) the shock wave has been reflected by the KS. The reflected shock impacts the bubble again, inducing a further secondary pressure loading on the bubble interface. The formation and the characteristics of the reflected pressure wave are governed by the mechanical properties of the solid surface [107]. The magnitude of the deformation induced by the solid is also a function of the properties of the solid material. The intensity of the reflected shock is of the same order of magnitude as the incident shock given the stiffness of the material, as highlighted in the validation case in subsection 4.1. Due to the high shear and elastic modulus of the KS, the solid interface deformation is minimal and the solid does not deform for more than $0.1\% R_0$ under the effect of the incident shock wave. The acoustic impedance for the kidney stone is $5909.94 \ MPa \cdot s/m$. Following the analysis of Brekhovskikh and Godin [21], the amplitude of the reflected p_r and the transmitted and p_t waves are:

$$p_{rf} = p_i \frac{Z/Z_0 - 1}{Z/Z_0 + 1}, \quad p_{tr} = p_i \frac{2Z/Z_0}{Z/Z_0 + 1} \, , \tag{40}$$
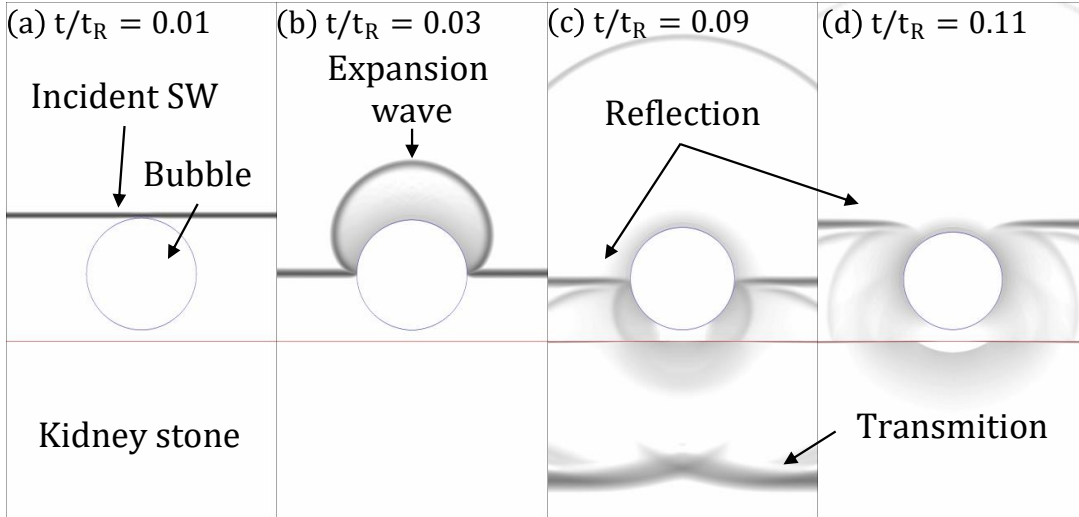
Figure 20: Contour map of the evolution of shock structure before the bubble collapse. The gray-scale colormap corresponds to the magnitude of the pressure field gradient. Blue iso-surface: The gas volume fraction level at $a_g = 0.5$, representing the bubble interface. Red iso-surface: The solid volume fraction at $a_s = 0.5$ represents the solid interface. (a) The initial configuration before the shock wave impact. (b) The expansion wave, (c) and (d) The reflection of the shock wave in the fluid and its transmission inside the solid phase.

where p_i is the intensity of the incident shock, Z is the acoustic impedance of the material, and Z_0 is the acoustic impedance of the surrounding liquid.

For the cases presented here, the incident shock wave intensity is $p_i = 35MPa$, thus Eq. 40 results in $p_{rf} = 19.9\ MPa$ and $p_{tr} = 55\ MPa$ for the reflected and transmitted wave intensities. The numerical analysis presented here compares well with the simplified model described in [21] providing similar predictions for the kidney stone configuration with the reflection and the transmission as measured in the simulation being $p_{rf} = 19.8\ MPa$ and $p_{tr} = 54.9\ MPa$ respectively. The agreement between the numerical simulation results and the analytical model of Brekhovskikh and Godin seems to hold for the softer material studied.

Similar conclusions can be drawn for the soft tissue with the acoustic impedance equal with $Z = 1647.56\ MPa \cdot s/m$, $p_r = 6.1\ MPa$, $p_t = 41.3\ MPa$ from the analytical expression and $p_r = 6.0\ MPa$, $p_t = 41.1\ MPa$ from the simulations. These values are in close agreement with both the acoustic theory and the results published by [25]. In both cases, the reflection is a compressive pressure wave. It should be noted that the aforementioned pressures were measured $25R_0$ from the center of the axis, in order to minimize the effect of the expansion wave from the LSW-bubble interaction prior to the shock impact to the solid surface.

The pressure field distribution at different instances for the shock-induced bubble collapse

in the proximity of KS is presented in Fig. 21a-a4. The result for the same configuration in the proximity of soft tissue is shown in Fig. 21b-b8. All cases shown in Fig. 21 correspond to detached bubbles with the same initial stand-off distance $S/R_0 = 1.2$.

Figs. 21a1 and 21b1 correspond to the start of the formation of the high pressure region
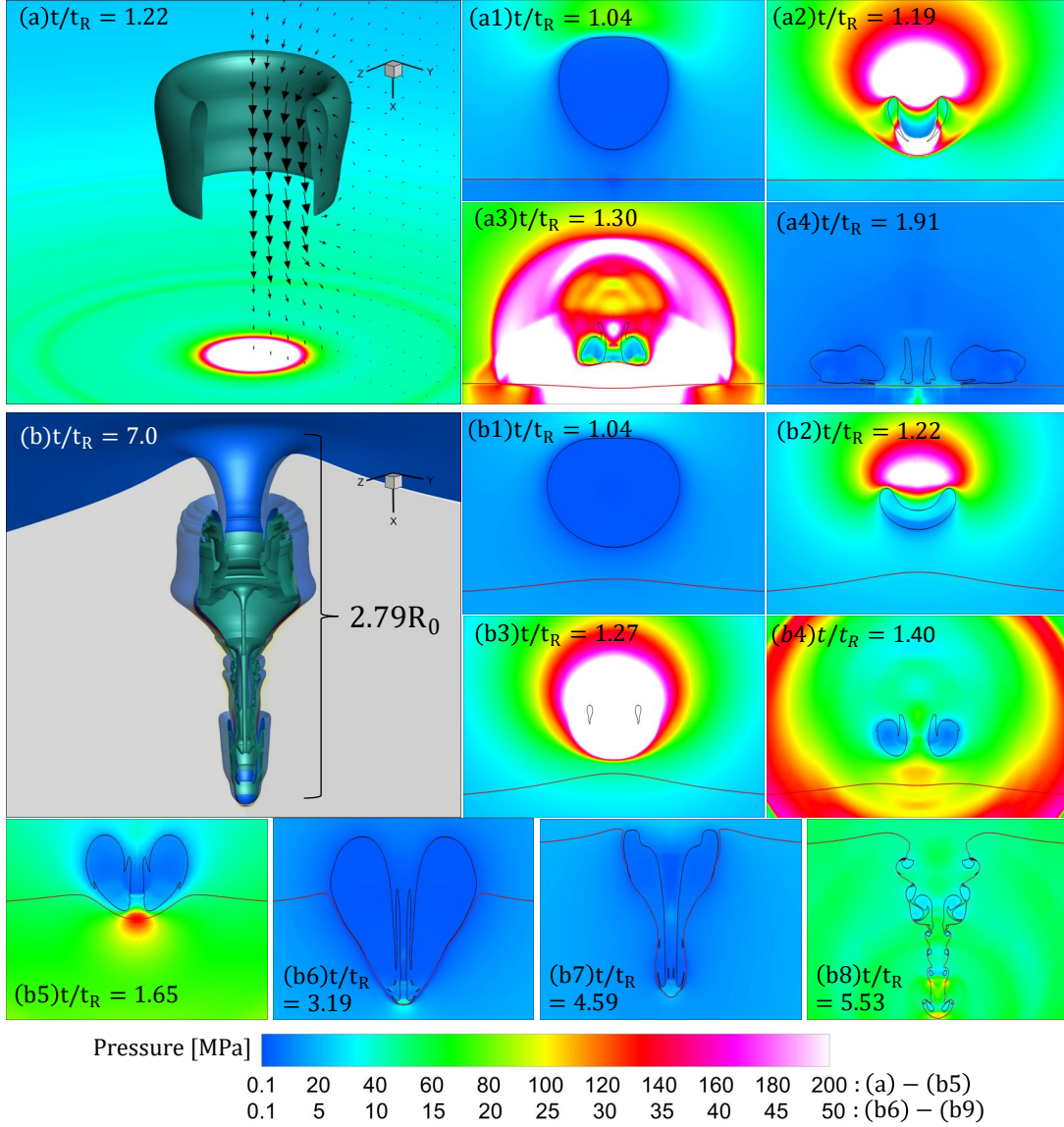
Figure 21: Shock-induced collapse of a detached gas bubble with initial stand-off distance $S/R_0 = 1.2$. Colormap: pressure distribution. Black iso-surface: The gas volume fraction level at $a_g = 0.5$ corresponds to the bubble interface. Red iso-surface: The solid volume fraction at $a_s = 0.5$ represents the solid interface. (a-a4) Collapse near the KS, (b-b8) collapse near the soft tissue. (a) Detail of the jet formation (arrows velocity magnitude) and the impact of the shock on the KS (pressure contour on the KS surface), (b) detail of tissue deformation. Same magnification in all figures, except the (a/b), and (b5-b8)

which initiates the collapse of the bubble. The bubble close to the kidney stone is collapsing faster compared to the bubble close to the soft tissue, as seen in the same figures. This is attributed to the increased intensity of the incident shock wave's reflection on the bubble interface. For the kidney stone configuration, the reflection is greater by 13.6 MPa, compared to the soft tissue. In general, the collapse is faster near solids with higher acoustic impedance, such as kidney stones, which is expected due to the additional loading of the reflection of the incident shock wave. Similar findings have been reported in [25].

The shrinking of the bubble during the initial collapse phase induces a characteristic sink flow [80]. In contrast to the rigid KS, the soft tissue has lower elastic modulus and thus deforms and moves upwards towards the adjacent interface of the bubble, (see Fig. 21b1 and 21b2).

In the frames of Fig. 21a2 and 21b2 the collapse of the bubble is presented. During the collapse, the distal bubble interface is gaining momentum moving rapidly towards the proximal bubble interface resulting in increased pressure distribution and rapidly moving towards the solid surfaces. In the present cases the direction of the collapse and the jet formation are dictated by the shock wave impact, as the bubble is initially in equilibrium. In principle, under other initial conditions, the liquid jet might be directed away from the solid boundary, in contrast to the presented results [171]. For the KS simulation at $t/t_R = 1.22$ (Fig. 21a) the bubble volume reaches a minimum. The impact of the two opposing moving liquid masses at the upper and lower interfaces of the bubble results in the emission of a water hammer shock wave directed toward the solid interface. The same mechanism is observed for the collapse near the soft tissue with the main difference that the toroidal shape is wider and shorter (Figs. 21a2 and 21b2). Specifically, the ratios between the two are: $d_{KS}/d_{ST} = 1.017$ and $L_{KS}/L_{ST} = 1.734$.

The emitted shock wave reaches $p/p_c = 0.370$ for the KS case while for the soft tissue case, it reaches $p/p_c = 0.183$. The induced impingement jet impacts on the surface of the kidney stone (Fig. 21a3) which further compresses the surface, at $t/t_R = 1.22$. This impact results in compression loading. The reflection of the shock wave impacts again the collapsing bubble. The effect of this secondary impact is more pronounced in the case of the kidney stone. In the KS case, a characteristic toroidal vortical structure is formed for both cases in Figs. 21a2 and 21b3.

The induced velocities, from the liquid jets, on the solid interface at $r/R_0 = 0$ are presented in Fig. 23a. In this figure, we present the initial upward movement of the soft tissue, due

to the sink flow, which reaches a maximum velocity of $u/u_c = -0.25$. Following the collapse of the bubble, the strong shock wave compresses the interface of the solid, specifically for the soft tissue case, the interface is abruptly changing its direction of movement. Following
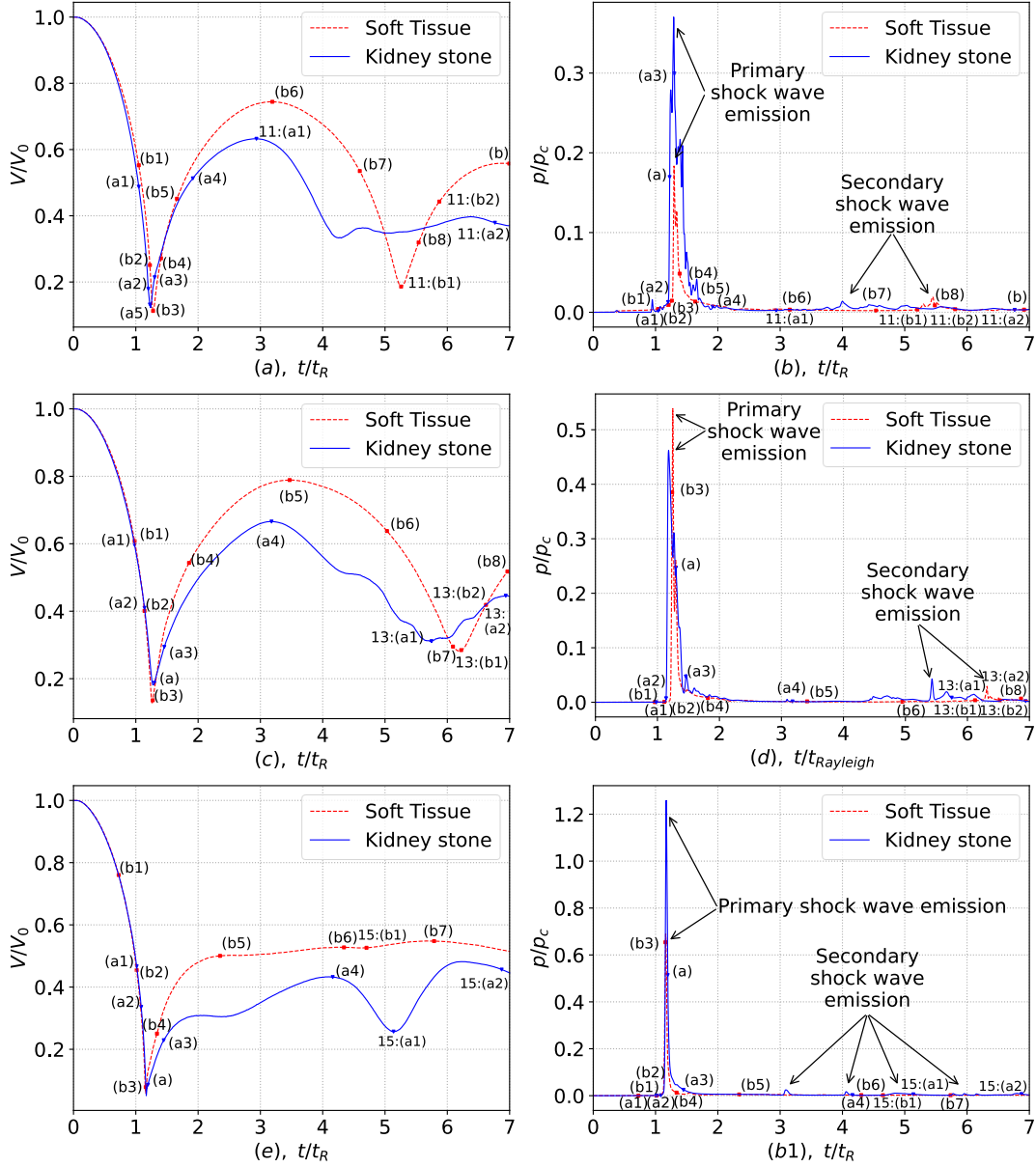
Figure 22: Effect of stand-off distance/attachment on non-dimensionalized gas volume evolution over time and non-dimensionalized pressure on the solid interface at $r/R_0 = 0$. (a)/(b) Detached bubbles with stand-off distance $S/R_0 = 1.2$, (c)/(d) Attached bubbles with stand-off distance $S/R_0 = 0.6$ and acute angle, (e)/(f) Attached bubbles with stand-off distance $S/R_0 = -0.2$ and obtuse angle. Time instances given are: (a-a4) for KS, and for ST (b-b8) from Figs. 21,25,27. References to secondary collapse figures 24,26,28 are given with their corresponding number. Same magnification in all figures, except the (a/b), and (b5-b8)

the impact of the liquid jet the interfaces further gain momentum. Due to the high shear and elastic modulus of the kidney stone, the maximum induced velocity is almost half of the corresponding in the soft tissue. Finally, the surface of the kidney stone rebounds, due to the high elastic energy gained by the initial compression.

In the work of P. Zhong et al. [185] and Heymann [61] the pressure rise due to liquid jet's impact on a solid boundary was investigated and a contact angle dependency was found. In both studies the authors considered a jet formation with clear boundaries and uniform velocity to derive the exact relations for the pressure rise. In our simulations, a pressure rise upon the jet's impact on the solid surface can be identified, which is in agreement with the reported correlation between the pressure rise and the contact angle.

As the bubbles continue to move towards the solid interfaces, the gas contained in the toroidal cavities expands, and the bubble rebounds, similar to a Rayleigh-spherical collapse. At $t/t_R = 1.5$ the bubble has reached the kidney stone and expands radially and in the proximity to the solid surface. This results in a secondary collapse shown in Fig. 22a and presented in more detail in Fig. 24a1-a2. The secondary collapse is weaker, due to the reduced pressure difference of the gas bubble content.

The bubble collapse close to the soft tissue exhibits a different mechanism as it expands further and impinges the solid surface, forming a circular crevice, Fig. 21b6 within the solid. The strong liquid jet thus greatly deforms the soft tissue creating the space for the torus to penetrate inside of it.

In Fig. 21b6 the bubble has penetrated the soft tissue, has reached its maximum volume, and thus the second collapse phase has started. As the bubble moves further inside the soft tissue, the soft tissue exerts a radial pressure, due to the elasticity of the pre-loaded material. This mechanism in addition to the pressure drop inside the bubble, due to its expansion, leads to the secondary collapse shown in detail in Fig. 24(b1 and b2). Two main features can be identified. The first is that the bulk of the bubble volume has created a circular crevice with $R_{cr}/R_0 = 0.482$, whereas the second one is that the fast-moving jet has impinged the tissue forming a long neck-like structure (see Fig. 24b1). The secondary collapse emits shock waves that originate from the 4 toroidal cavities that collapse, with some additional auxiliary pockets of gas not visible in Fig 24a1-a2 [120]. The resulting collapse and shock wave emission, generate vortices around the expanding torus, that in turn exert high tensile stress on the tissue. The vortices are generated by the high liquid velocities between the torus and the solid interface. The induced stress is forces strips of tissue to elongate.
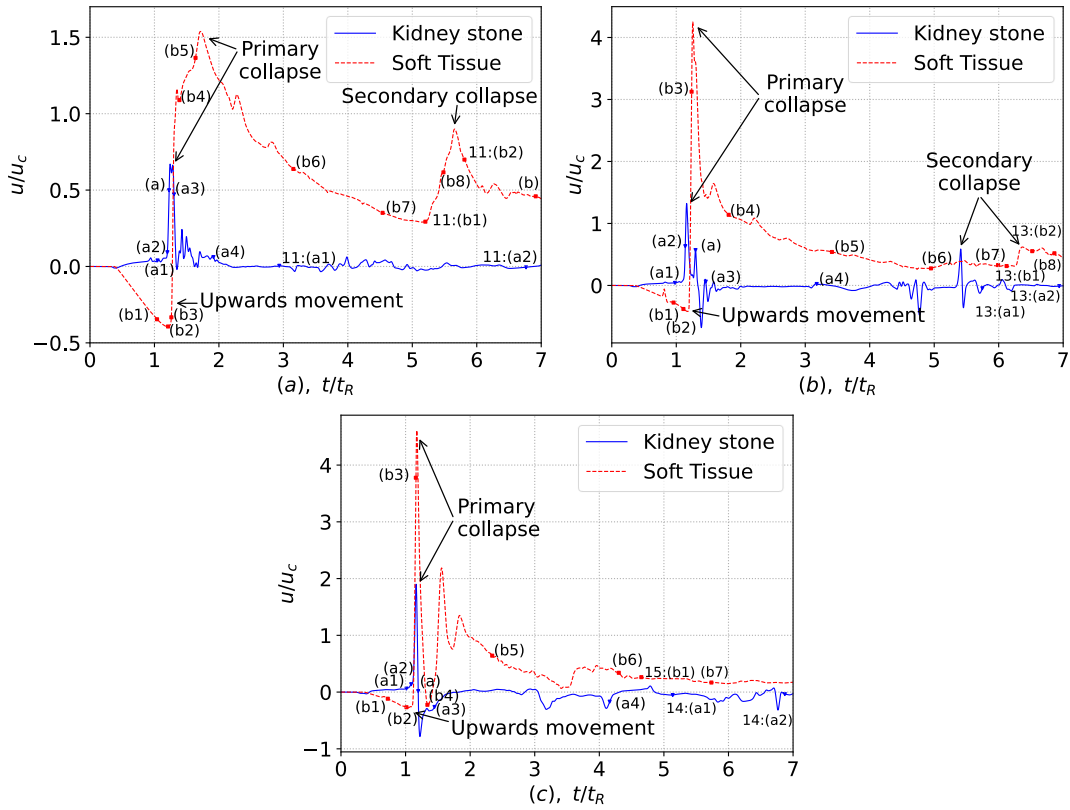
Figure 23: Effect of stand-off distance/attachment on solid boundary's velocity overtime at $r/R_0 = 0$. (a) Detached bubbles with stand-off distance $S/R_0 = 1.2$, (b) Attached bubbles with stand-off distance $S/R_0 = 0.6$ and an acute angle, (c) Attached bubbles with stand-off distance $S/R_0 = -0.2$ and obtuse angle. Time instances given are: (a-a4) for KS, and for ST (b-b8) from Figs. 21,25,27. References to secondary collapse figures 24,26,28 are given with their corresponding number.

Additionally, this phenomenon produces high shear stresses, highlighted by the red and black areas of the maximum tensile stress contour map in Fig. 24. This can be identified as a secondary mechanism for tissue damage during ESWL. The expanding toruses further thicken the neck of the crevice. At the head of the crevice located at the very bottom, the same mechanism of tension-driven tissue damage takes place. In the experimental work of Kodama et al. [83] (see Fig. 5(c)) a qualitatively similar structure can be identified for a bubble collapsing close to a gelatine surface. In total three different bubble sizes were examined namely, $R_e = 0.61mm$, $R_e = 0.33mm$, $R_e = 0.21mm$, utilizing a shock wave with a lower amplitude $p_s = 10.2 \pm 0.5 MPa$ than in our case. For the first two bubble sizes, the collapse dynamics and the gelatin response exhibit rather different behavior than the one discussed presently. This can be attributed to mainly to the bubble size difference. The third and smaller bubble size, however, appears to produce the same structure with both the circular crevice and the neck-like structure and even the expansion of the 4th torus which will lead to the

head-like structure. Additionally, the secondary collapse mechanism, and tissue penetration, are also reported in the study. Comparing the first and secondary collapse mechanisms (see Fig. 22a), the equivalent bubble radius exhibits a damped oscillatory behavior, with most of the energy of the system having decayed after $t/t_R = 7$. The resulting shape of the torus and the deformation of the tissue are presented in Fig. 21b, after which the elasticity of the tissue is the main driving restoring force.
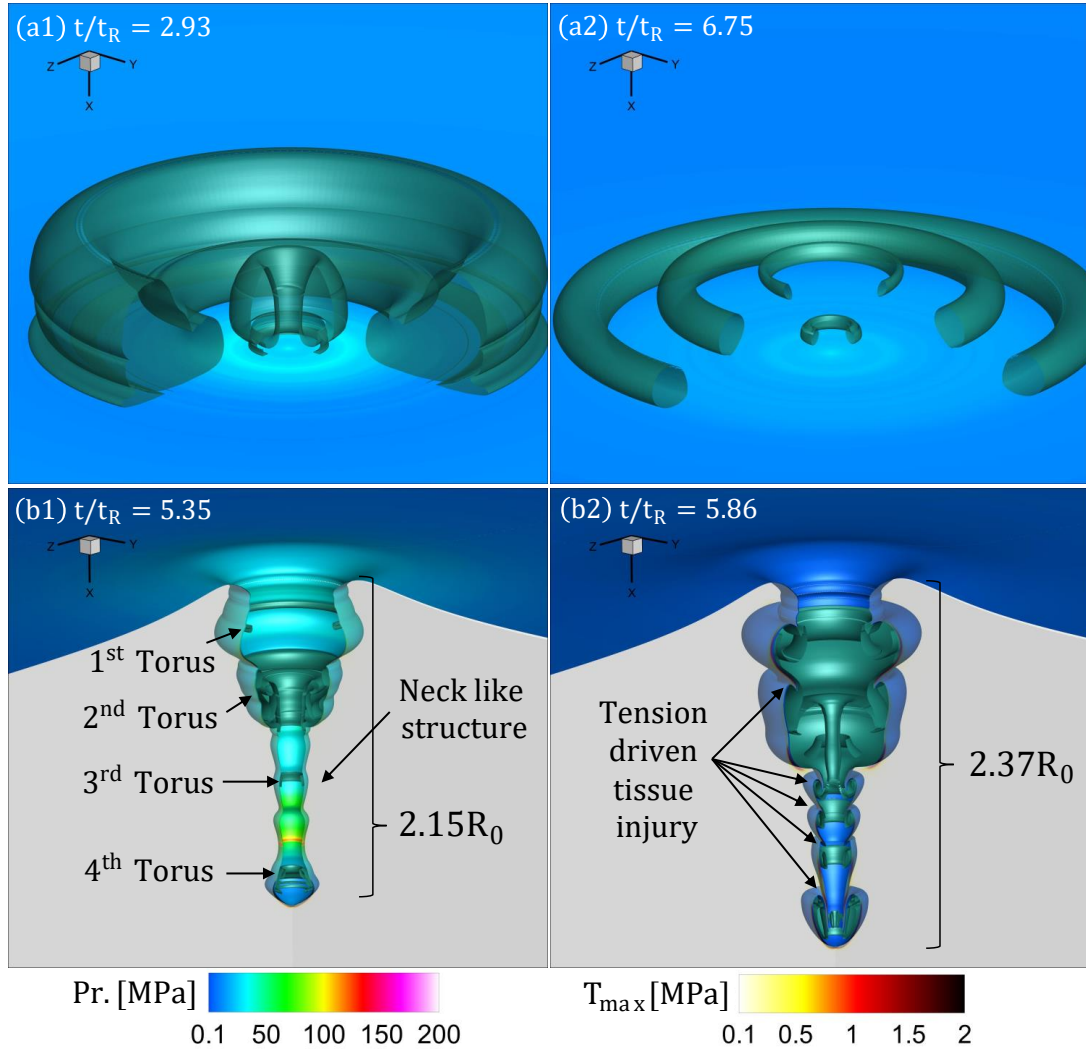
Figure 24: Secondary collapses for detached bubbles with initial stand-off distance $S/R_0 = 1.2$. Colormap on solid surface: pressure distribution. Green iso-surface: The gas volume fraction level at $a_g = 0.5$. Colormap on cross-subsection: maximum tensile stress distribution. (a1/a2) Collapse near the KS, with torus break up (b1/b2) Collapse near the soft tissue, tissue penetration, and tension-driven tissue damage.

3.2.2   Attached bubbles with acute interface angle, $1 > S/R_0 > 0$

In the following, we investigate the bubble dynamics of bubbles that are initially attached to solid surfaces, that form an interface at an acute angle at the solid surface, see Fig. 19b. Previous research by Lauer et al. [90] and others [86, 164, 120] have studied the collapse dynamics close to a rigid wall, under uniform high pressure. The findings indicate the formation of a high-pressure region on the top of the bubble, while the attached face, due to the depressurization of the surrounding liquid, lags behind. Thus, the collapse is predominately driven by the high-pressure region on the distal interface of the bubble. The collapse takes place near of the wall and gives rise to a torus after the impact of the jet on the wall.

In Fig. 25 pressure contours for the shock-induced bubble collapse are presented for attached bubbles with distance to the wall equal to $S/R_0 = 0.6$. Similar findings to the aforementioned studies can be observed for the case of a bubble collapse near a kidney stone Fig. 25a-a4. After the impact of the incident shock wave, the distal side of the bubble starts accelerating toward the interface. The rest of the bubble's interface is radially loaded as the incident shock wave transverses toward the solid. Depending on the acoustic impedance of the solid the reflected shock wave will further load the bubble interface. Thus, the proximal interface of the bubble starts to slide on the solid, and collapse radially (see Fig. 25a1-a2). Due to the depressurization of the liquid, however, the axial velocity, by which the bubble slides on the solid, is one order of magnitude lower, compared to radial velocity, with a ratio of $|u|/|v| = 7.53$. The axial velocity is denoted with u and v is the radial slipping velocity on the kidney stone surface, at $t/t_R = 1.13$.

After the collapse phase near the kidney stone, a water hammer shock wave impacts the surface, (see Fig. 25(a/a3). In Fig. 22d we present the pressure, probed on a Lagrangian sensor that follows the interface of the solid at $r/R_0 = 0$. The water hammer shock impact reaches $p/p_c = 0.462$. This value is greater than the one observed for the detached collapse case close to the KS. This can be explained as the liquid jet rapidly decelerates when it impacts the surface of the kidney stone. Similar findings are reported at [90]. Due to the constrained space, the liquid jet then expands radially, forming the toroidal shape shown in Fig. 25a/a3. Due to the abrupt change of the liquid jet direction, vortex rings appear at the upper interface of the torus, which can be seen in Fig. 25a.

In Fig. 23b the solid boundary velocities are presented, for a sensor located at the axis of symmetry $r/R_0 = 0$. Initially, the KS interface starts accelerating due to the impact of the incident shock wave. Following the collapse and the impact of the liquid jet, the main

compression of the interface is apparent. The interface rebounds back due to the significant elasticity of the KS, and releases the stored elastic energy. In Fig. 22c the rebound of the torus is shown with the maximum volume reached at $t/t_R = 3.17$. Smaller secondary collapses induce additional velocities of the interface and less intense*- shock wave emissions at later stages. The final stable shape is reached after $t/t_R \approx 7$. The torus has detached from the kidney stone, expanded radially, and formed two new toruses, which remain in the proximity of the solid (see Fig. 26b).

Similar to the detached bubbles, there is a time lag of the initiation of the collapse phase as shown in Fig. 25a1 and Fig. 25b1. This is the result of the difference in the acoustic impedance between the kidney stone and the soft tissue, as explained in subsection 3.2.1. For the attached bubble cases this mechanism is less prominent. In later stages of the first collapse phase (see Fig. 22c), the time difference in the collapse is negligible.

As the bubble is getting compressed and finally collapses, a suction pressure is applied on the surrounding tissue by the inwards radial movement of the attached interface. This results in a wave-like formation seen in Fig. 25b1. In the next stage of the collapse (Fig. 25b2), and before the bubble reaches it's minimum volume, a more prominent wave-like structure has been created, which further deforms the soft tissue, resulting in its stretching and the increase of its tensile stress. The maximum upwards displacement reaches $d/R_0 = 0.427$ at $t/t_R = 1.218$.

In the same Fig. 25b2, it is apparent that the formation of the wave-like structure coincides with the creation of circular crevices. Similar to the detached bubble movement prior to the collapse, the soft tissue interface moves upwards, (Fig. 23b). Thus, when the bubble collapses the liquid jet gets trapped in this crevice, further intensifying the penetration of the tissue. In the same figure, the maximum velocity of the jet is presented, which reaches $u/u_c = 4.12$. Additionally, the impact of the axial jet with the inwards radial velocity results in vortices which in turn, create a radially and axially expanding torus as seen in Fig. 25b3/b4. The shock emission is presented in Fig. 22d and reaches $p/p_c = 0.539$, which is higher than the collapse near the kidney stone $p/p_c = 0.462$. This comes in contrast to the detached bubbles, presented in the previous subsection. Two main factors contribute to this behavior. The first is that the pressure loading is caused by the incident and the reflected shock wave on the entire bubble interface, whereas for the attached bubble this pressure stress is applied only to a portion of the bubble interface. The second factor is that the jet is entrapped within the circular tissue crevice that has formed.

As the bubble expands, following the initial collapse, the tissue is further compressed both axially and radially. The rebound phase ends after $t/t_R = 3.46$ where the maximum bubble volume is reached. In a similar way as the detached bubble collapse near the soft tissue, the latter exerts radial pressure on the bubble during the rebound. This mechanism alongside the gas expansion, and the subsequent pressure drop inside the bubble, leads to the secondary
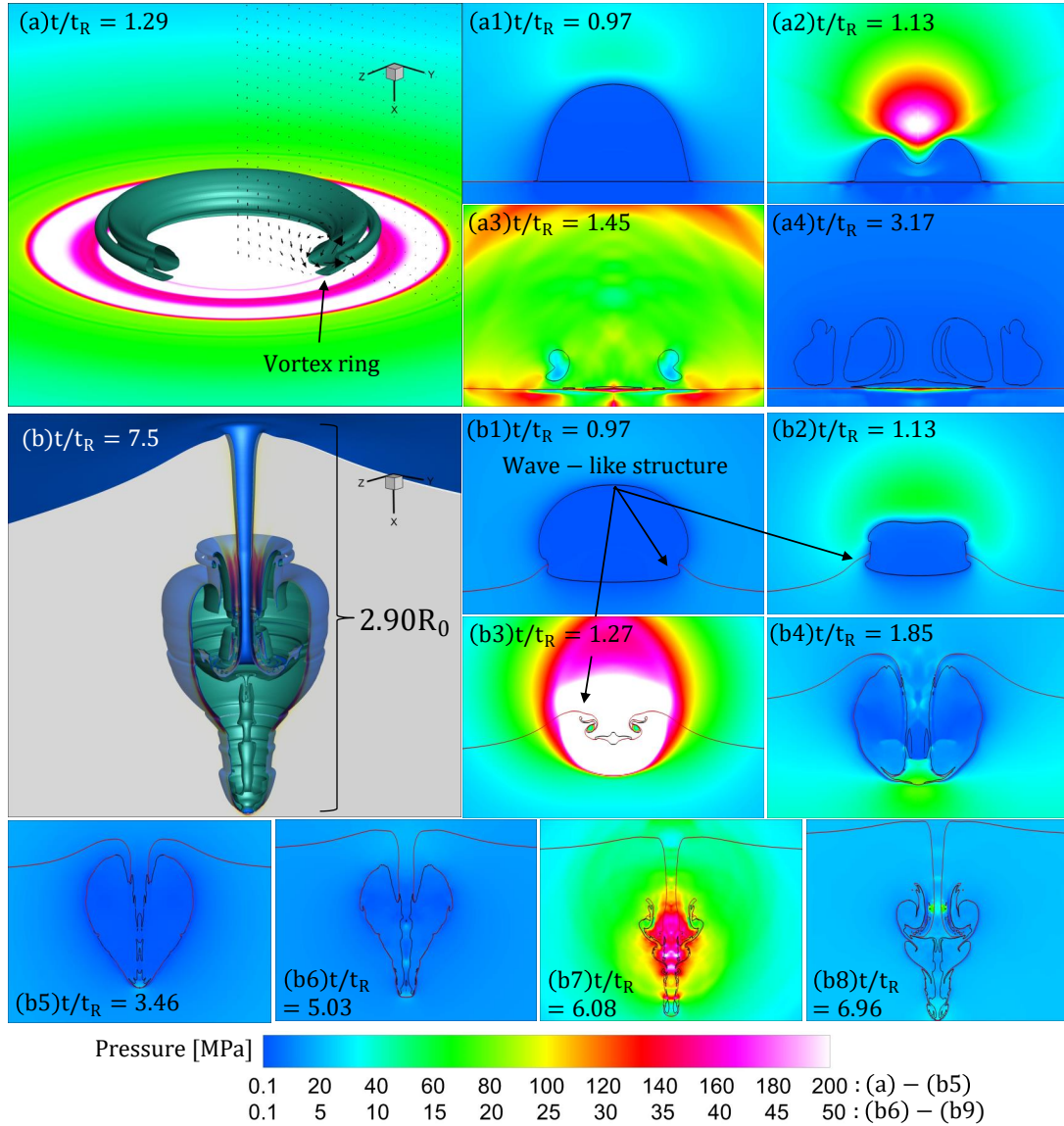
Figure 25: Shock-induced collapse of an attached gas bubble with initial stand-off distance $S/R_0 = 0.6$. Colormap: pressure distribution. Black iso-surface: The gas volume fraction level at $a_g = 0.5$ corresponds to the bubble interface. Red iso-surface: The solid volume fraction at $a_s = 0.5$ represents the solid interface. (a-a4) Collapse near the KS, (b-b8) collapse near the soft tissue. (a) Detail of the jet formation (arrows velocity magnitude) and the impact of the shock on the KS (pressure contour on the KS surface), (b) detail of tissue deformation. Same magnification in all figures, except the (a/b), and (b5-b8)
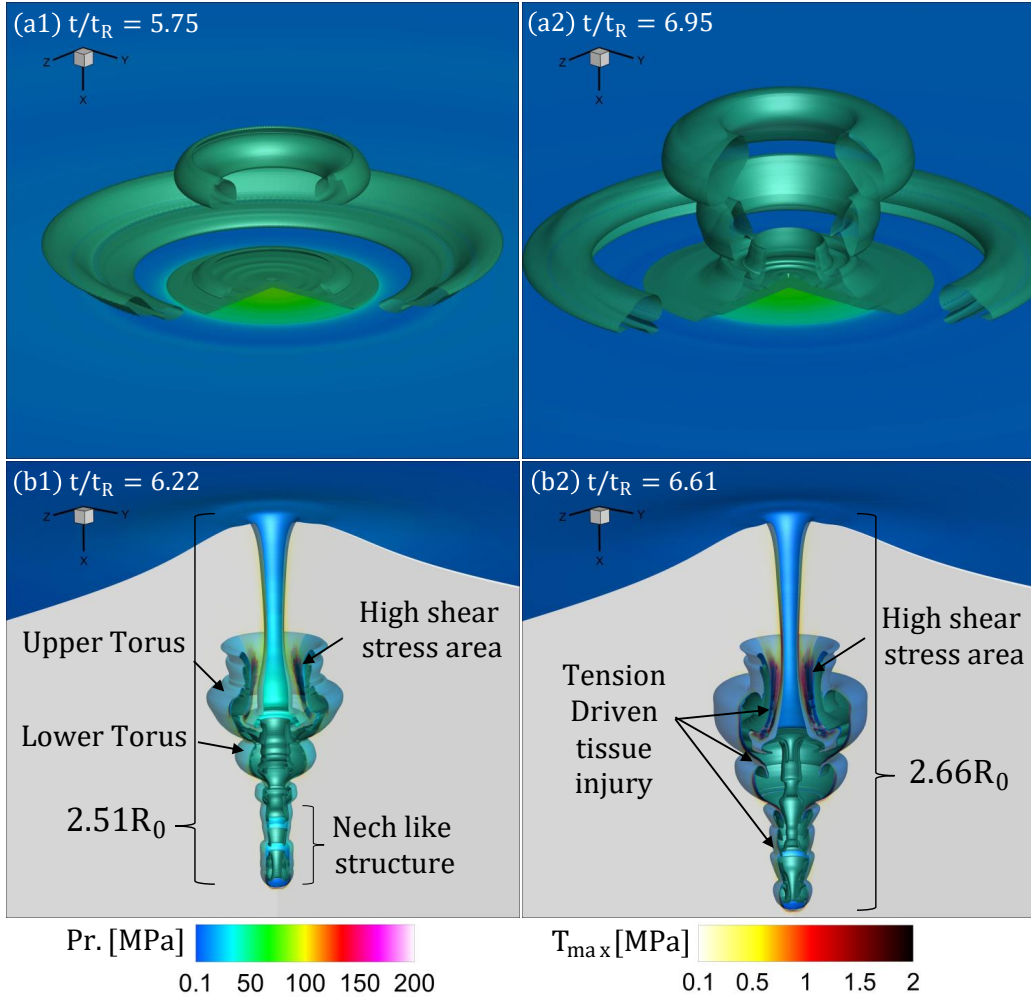
Figure 26: Secondary collapses for detached bubbles with initial stand-off distance $S/R_0 = 0.6$. Colormap on solid surface: pressure distribution. Green iso-surface: The gas volume fraction level at $a_g = 0.5$. Colormap on cross-subsection: maximum tensile stress distribution. (a1/a2) Collapse near the KS, with torus break up (b1/b2) Collapse near the soft tissue, tissue penetration, and tension-driven tissue damage.

collapse phase. In the Fig. 25b5 we present the penetration of the soft tissue at $t/t_R = 3.46$. It is apparent that the wave-like formation has now been deformed inwards, leading to a similar tensile-driven tissue damage mechanism. As the bubble collapses the main torus breaks into smaller toruses, shown in Fig. 25b7 and in more detail in Fig. 26b1. The shock emission from these secondary collapses can be seen in Fig. 22d. The creation of vortices on the tissue/gas interface and the shock emissions result in the same tension-driven elongation of the tissue from the toruses/tissue interfaces, similar to the initial collapse phase. This tissue damage mechanism is yet again notable for attached bubbles to soft tissue. High shear stresses are observed in Fig. 26, in these tension-driven areas, as well as in the imminent surroundings of the expanding torus. As the gas expands inside the tissue, a similar structure to the

detached bubble emerges, with a long neck-like structure followed by the main torus. The final deformation after $t/t_R = 7.5$ is presented in Fig. 25b.

3.2.3   Attached bubbles with obtuse interface angle $S/R_0 < 0$

Shock-induced attached bubble collapses with initial stand-off distance to the wall equal with $S/R_0 = -0.2$ are presented in Fig. 27. The initial attachment of the bubble relative to the solid surface forms an obtuse angle shown in Fig. 19c. As explained in the work of Koukouvinis et al. [86], the bubble collapse dynamics change compared to the previous cases. This is driven by the rapid local pressure increase in the circumference of the bubble, close to the solid surface, which leads to a momentum focusing. The increased pressure is the result of the velocity component normal to the solid interface, at the bubble/solid boundary. In this case, this velocity component causes a compression of the solid, contrary to the case before (see subsection 3.2.2) where this velocity component caused tension, and depressurization of the liquid that surrounded the bubble solid interface. The main difference between the presented results and the aforementioned study [86], is the incident shock wave loads the surface of the bubble gradually. Thus, the distal part of the bubble accelerates first, with the attached face of the bubble starting to slide on the kidney stone after $t/t_R = 0.141$.

In the Figs. 27(a-a4), the collapse near the kidney stone is presented. It is apparent that a circumferential pressure increase is the main driving force for this attachment configuration. The mechanism mentioned above, of the increased pressure close to the bubble/solid interface results in a higher radial acceleration of the interface than the acceleration at the distal face of the bubble. Thus the collapse of the bubble can be characterised as a radial collapse. Thus, the same bubble dynamics are present for a shock-induced bubble collapse, similar to the findings presented in literature [90], for bubbles under high ambient pressure. When the bubble interface collapses in the axis of symmetry, a water hammer shock wave is emitted. In Fig. 22f, the maximum amplitude of the shock is presented, which reaches $p/p_c = 0.689$. In Fig. 23c the jet velocities on the solid boundary are shown. The impact of the liquid jet on the solid surface induces the highest velocities amongst the cases presented in subsections 3.2.1 and 3.2.2. Here the maximum velocity observed is reaching $u/u_c = 4.609$. The stored elastic energy results in a restoring upwards movement of the solid surface.

The bubble collapse is depicted in Fig. 27a, producing a thin elongated cylindrical structure that resembles needle-like shape. The liquid jet abruptly changes direction, by $\pm 90^o$ degrees, creating two jets, one with an upwards direction and a one with downwards. The upwards

motion, in addition to the high vorticity around the top of the needle-like shape, creates the characteristic mushroom rebound of the bubble, presented in Fig. 27a3. In the rebound phase, the bubble expands away from the kidney stone, creating a torus from the mushroom cap, which collapses again at $t/t_R = 5.172$, as visible in Fig. 22e, and in more detail in Fig. 28(a1/a2). Due to the vortices around the torus, gas pockets detach and collapse producing secondary shock emissions, apparent in Fig. 22f. The remaining gas volume of the initial bubble stays attached to the kidney stone surface as it can be seen in Fig. 27b4, with some smaller collapses happening at times $t/t_R = 3.07, 4.03, 5.02$. This collapse also induces the motion of the solid surface.

In Fig. 27(b-b8), the shock-induced collapse of the bubble attached to the soft tissue is presented. After the incident shock wave impacts the bubble, the circumferential pressure rise around the bubble close to the soft tissue becomes apparent. The soft tissue is deformed upwards, following the motion of the bubble resulting in a similar wave-like structure observed in subsection 3.2.2. Gas pockets get trapped inside the soft tissue as the bubble collapses, which will lead to secondary collapses and rebounds at later stages. Additionally, a small torus is detached from the bubble in the upper part of the bubble interface (see Fig. 27b2) at $t/t_R = 0.976$ and collapses before the main bubble.

The hammer shock wave emitted during the secondary collapse which takes place within the initial crevice reaches a pressure maximum $p/p_c = 1.259$. This confined collapse leads to a needle-shaped structure that is forming after $t/t_R = 1.15$ as visible in Fig. 27.

The inwards radial jet terminates by producing a water hammer shock wave, similar to the case of the collapse near the kidney stone. A double wave-like structure has been created and shown in the same figure this structure is the result of the high radial velocities during the collapse, and the inability of the soft tissue to follow the bubble motion due to its stiffness. The downwards-moving liquid/gas jet impacts the soft tissue and creates an inner and an outer crevice, shown in Fig. 27b4. As the bubble expands and rotates inside the inner crevice, a strip of tissue is elongated under tension giving rise to the exact same mechanism of tension-driven damage as presented before. Furthermore, in the outer crevice, an expanding gas pocket, trapped in the initial stages of the bubble collapse, produces a similar feature with an additional tissue layer, that is tension driven by the liquid jet inside the main crevice. Thus, in this case, an extended tissue damage mechanism can be identified (see Fig.27(b5-b8)).

The liquid jet velocities on the solid interface at $r/R_0 = 0$ are presented in Fig. 23c. The same prevailing dynamics are present during the initial upwards movement, followed by

the violent liquid jet compressing the soft tissue interface. For this attachment configuration, the velocities induced in the soft tissue boundary are the highest. A detail observed in the same figure is that the strong vortex that develops during the collapse induces a momentary upwards movement on the soft tissue at $t/t_R = 1.33$. This sudden change of velocities can be an indication of an additional mechanism of tissue damage, in which high acceleration of the soft tissue boundary and compression/tension loading may result in localized tearing.
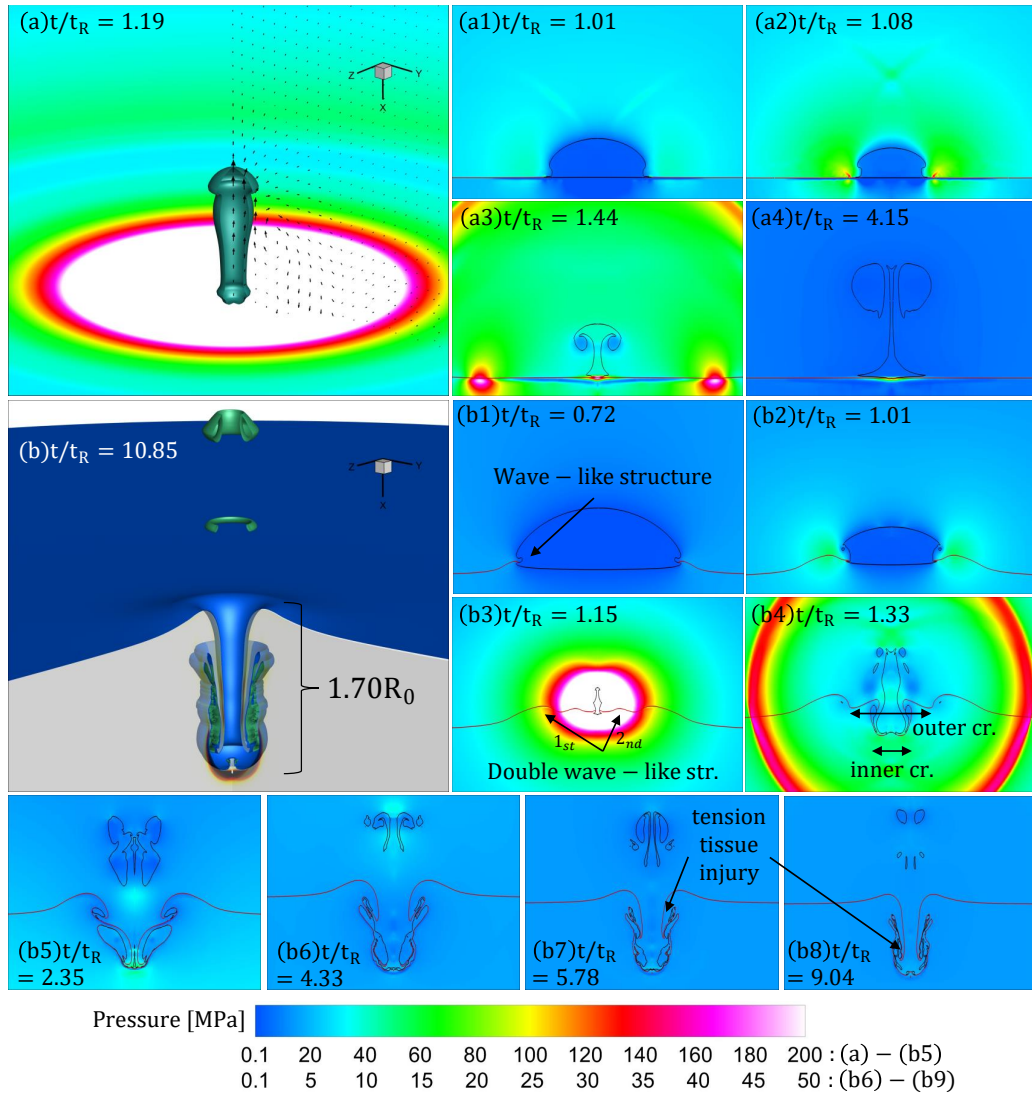
Figure 27: Shock-induced collapse of an attached gas bubble with initial stand-off distance $S/R_0 = -0.2$. Colormap: pressure distribution. Black iso-surface: The gas volume fraction level at $a_g = 0.5$ corresponds to the bubble interface. Red iso-surface: The solid volume fraction at $a_s = 0.5$ represents the solid interface. (a-a4) Collapse near the KS, (b-b8) collapse near the soft tissue. (a) Detail of the jet formation (arrows velocity magnitude) and the impact of the shock on the KS (pressure contour on the KS surface), (b) detail of tissue deformation. Same magnification in all figures, except the (a/b), and (b6-b8)
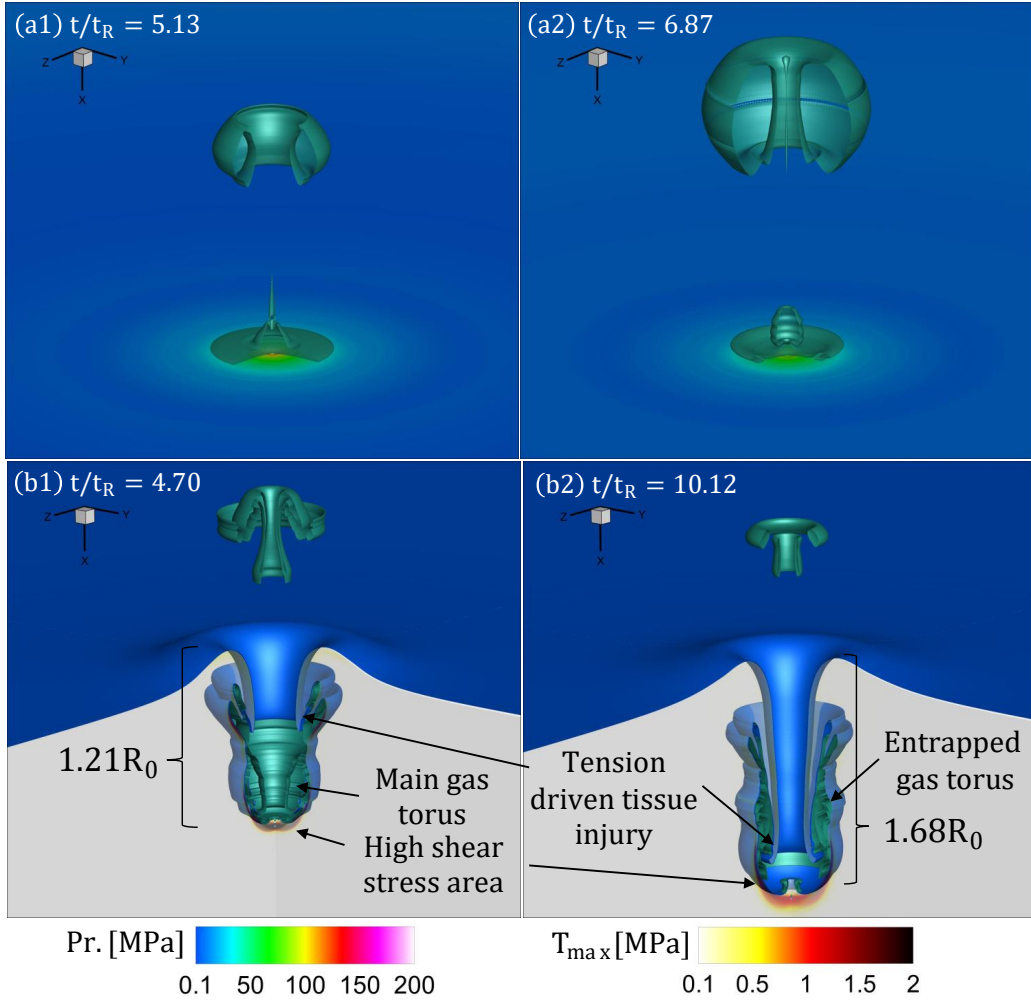
Figure 28: Secondary collapses for detached bubbles with initial stand-off distance $S/R_0 = 1.2$. Colormap on solid surface: pressure distribution. Green iso-surface: The gas volume fraction level at $a_g = 0.5$. Colormap on cross-subsection: maximum tensile stress distribution. (a1/a2) Collapse near the KS, with torus break up (b1/b2) Collapse near the soft tissue, tissue penetration, and tension-driven tissue damage.

In the later stages of the collapse, the liquid jet has further deformed the tissue, resulting in a crevice with part of the gas torus being enclosed between two layers of soft tissue. The tension-driven elongation of the tissue is still prominent, driving the collapse of the tissue in itself, as seen in Fig. 28, $t/t_R = 4.7 - \approx 10.0$. No strong secondary collapses are present in this case, as the collapse splits the gas volume into two parts and the vortices surrounding the gas toruses, restore the pressure without a rapid expansion, which could have led to a secondary collapse similar to the detached bubble collapses and attached with acute angle cases. The final shape of the deformed tissue after $t/t_R = 10.85$ is presented in Fig. 27b. High shear stresses can be seen in the same figure, at the base of the circular crevice, as well as inside the elongated part of the soft tissue which has trapped the rest of the gas torus between

the two layers.

3.3   Conclusions

In this chapter, we presented a numerical investigation of the dynamic solid-liquid-gas inter-actions occurring during shock-induced bubble collapse for detached and attached bubbles in the proximity of a kidney stone and soft tissue. The numerical solver presented in chapter 2 was applied for shock-induced bubble collapse configurations against soft and rigid biomateri-als with varying stand-off distances. Specifically, detached and attached bubbles were studied with acute or obtuse angles of contact.

The results revealed the effect of the stand-off distance of the bubble and the acoustic impedance of the solid material on the collapse dynamics characteristics. For detached bubbles with an initial stand of distance $S/R_0 = 1.2$, the influence of higher acoustic impedance leads to more violent collapse and higher primary shock wave emissions. The induced jet leads to the bubble's entrapment in an induced crevice formation within the soft tissue that is leading to a secondary collapse. A tension-driven tissue damage mechanism was detailed, where tissue filaments are stretched during the secondary collapse, and the subsequent bubble rebound. The secondary shock waves emitted were found to be of lower intensity than in the primary collapse. The secondary jet velocity magnitude, however, is comparable to the initial jet produced during the primary collapse.

For attached bubble collapses with an initial stand-off distance of $S/R_0 = 0.6$, the col-lapse dynamics are significantly different. The collapse is driven by a synergy of radial and axial movement of the bubble's interface, leading to a more violent collapse. No significant difference, however, was found in the collapse time. The primary shock wave emission in both solid materials is higher in relation to detached bubbles. Specifically, for the soft tissue case, a wave-like formation was observed. These wave formations entrapped the collapsing bubble within a crevice that enhanced the focusing of the shock wave and the impact of the resulting liquid jet. The tissue penetration from the initial collapse is thus more prominent, leading to greater penetration depth. The same tension-driven tissue damage mechanism is present during the secondary collapse phase.

For attached bubbles at an initial stand-off distance of $S/R_0 = -0.2$, the collapse dynamics present a significant deviation. The radial movement of the bubble is dominating the collapse, leading to a characteristic needle-like shape at the collapse stage. The radially converging

liquid jet split the bubble into two toruses. No difference in the collapse time is present, between the kidney stone and the soft tissue. The primary shock wave emission is higher for the kidney stone due to the rigidity of the specific material. For the soft-tissue case, a double-wave-like structure emerges on the interface, which leads to the elongation of a circular tissue filament during the liquid jet penetration of the tissue. Thus, the same tension-driven tissue damage mechanism is also apparent for this standoff distance. For this case, however, no instances of secondary collapse were detected inside the soft tissue

In this chapter, we have demonstrated the complexity of bubble dynamics close to rigid and soft bio-materials and elucidated a tissue damage mechanism for attached and detached gas bubbles during shock wave lithotripsy applications. This mechanism of tissue penetration and tension-driven tissue damage may be helpful to understanding the mechanisms leading to hemorrhage and tissue damage in shock wave lithotripsy and ultrasonic-related procedures. It should be noted, that the validity of the presented results is restricted to the conditions that were investigated, and a follow up study will address the influence of bubble size, shock wave profile, and a broader range of stand-off distances. In general, the developed framework is intended for the study of cavitation in complex geometries, spatial mapping of material properties, and bubble cloud interactions with soft tissue.

4   Effects of inertial bubble collapse on during SWL

4.1   Background

The adverse implication of cavitation has been investigated by several experimental studies focusing on the shock wave bubble interaction close to a soft bio-material [58, 77]. The pioneering work of Dear et al. [63, 67] reported high-velocity jets from planar shock-induced bubbles, for gelatin substrate Ohl et al. [155] showed that free gas bubbles submerged in water form a liquid jet in the direction of the impacting shock wave, suggesting a microinjection mechanism when bubbles are in the proximity of cells. Kodama et al. [81] elucidated this injection mechanism into gelatin, identifying a sonoporation mechanism induced by bubbles attached to the surface. Zhong et al. [188] studied the shock wave-inertial microbubble interaction and suggested that at low exposures the efficiency of shock-wave-mediated macromolecule delivery is enhanced, whereas at high exposures with more than 100 shocks and operating spark voltage of $25kV$ tissue injury is apparent. Sapozhnikov et al. [147] studied the effect of pulse repetition frequency (RPF) on cavitation and supported the hypothesis that slow RPF can reduce tissue injury as the nucleated bubbles dissolve before they inertially collapse by the subsequent shock waves. Philipp et al. [127] studied the interaction of a lithotripter-generated shock wave with a pre-existing air bubble using high-speed photography. In this study jet velocities in the range of $400 - 800 \ m/s$ were reported at the time of the collapse, for bubbles with initial size between 0.15 to $1.2mm$, which can penetrate soft tissue interfaces. Recent research has highlighted that, in principle, the formation and direction of the liquid jet are dependent on the shock wave profile and intensity, the initial bubble size, and the stand-off distance from a solid or free surface [115, 178, 182]. Towards addressing the scientific questions raised by this hypothesis, we aim to investigate the influence of these parameters, on the dynamics of the impact of bubble-induced cavitation on rigid and soft biological materials.

An important factor that affects bubble dynamics is the proximity of the bubble to a wall, i.e., the stand-off distance. The experimental work of Lindau et al. [30] investigated the jet formation and collapse dynamics for various stand-off distances. Several authors have conducted similar experimental studies on cavitation erosion [38, 72]. Numerical studies of collapsing bubbles detached and attached to a solid wall revealed the importance of the angle of attachment. Angles smaller than 90° result in an axial collapse with the formation of the liquid jet and wall hammer towards the solid interface. Angles greater than 90° resulted in

a radial collapse behavior with a pin-type collapse and mushroom shape rebound phase [86, 89]. In our previous work [85], we presented the development of a numerical tool that further expanded on these dynamics, revealing the mechanisms of crater formation, and the wave-like structures, during the collapse of attached bubbles on soft tissue.

Another important factor at play in cavitation-induced injuries is the shock wave profile and the pulse amplitude that is generated by the lithotripter. Lithotripters produce peak positive pressures in the range of $20 - 180\ MPa$, and maximum negatives of $-20 MPa$ [10, 187]. Tandem shock waves can additionally be utilized to enhance the effect of cavitation on kidney stone pulverization [101]. In principle, greater shock wave amplitudes force bubbles to collapse more violently. Studies suggest that higher shock wave amplitudes, in shock wave lithotripsy, can result in acute tissue injuries due to various factors, including cavitation bubbles, inhomogeneity of the tissue, and emergence of shear shock waves [64]. However, the exact relationship between higher amplitudes and cavitation-induced tissue damage remains not clearly understood.

Furthermore, the excitation of a polydisperse range of bubble sizes from the tensile part of a lithotripter shock wave is revealed in the experimental work of Pishchalnikov et al. [129]. It has been reported that bubble sizes from 7 to 55 μm nucleate and collapse after the passage of the shock wave. In the numerical work of Wang [174], it was found that bubble sizes larger than 130 μm do not collapse in the same time frame as the shock wave passage, for a shock wave with an amplitude of $35 MPa$. In general, higher shock wave amplitudes will accelerate the collapse, hence the range of bubble sizes that collapse under shock-induce loading will vary depending on the overpressure. Thus, the effect of the initial bubble size on the collapse dynamics close to the surface of kidney stones and soft tissues is an important parameter that we investigate in the present work.

In this chapter, we aim to expand from the study presented in the chapter 3 by investigating the influence of attachment, bubble size, and the pulse's amplitude and their effect on bubble-soft tissue interaction. More specifically, the first parametric study corresponds to the effect of the stand-off distance of the bubble center from the solid surface on the bubble collapse dynamics under the effect of a lithotripter pulse, commonly used in numerical and experimental studies [68]. The stand-off distances that were selected, range between bubbles placed away from the solid boundary ($S/R_0 = 4.0$) to bubbles attached to the wall boundary with an acute contact angle to the solid surface corresponding to a stand-off distance equal to $S/R_0 = -0.2$. Both rigid and soft solid materials have been simulated. Specifically, a uric acid-type kidney stone and a soft tissue, with properties close to those of liver tissue have been considered as

representative materials. The second parametric study corresponds to the effect of the initial bubble size. The range of bubble sizes is $R_0 = 80\mu m$ to $R_0 = 10\mu m$. In this case, three attachment configurations were examined, namely initially detached bubbles, and attached bubbles with an obtuse and an acute contact angle, as these attachment configurations exhibit different collapse dynamics [86]. The same soft and rigid solid materials were used, as in the first parametric study. The third parametric study investigates the effect of the lithotripter's pulse amplitude on the bubble-tissue interaction. In these cases, the overpressure varied from $20MPa$ to $180MPa$. Similar to the second configuration the same three stand-off distances were considered.

4.2   Parametric studies

In this section, the following parametric studies are presented:

a. The investigation of the effect of the stand-off distance and attachment angles of the bubble dynamics near two solid materials,

b. The investigation of the effect of the bubble size on the collapse dynamics close to soft and rigid bio-materials, and

c. The investigation of the effect of the amplitude of the lithotripter pulse on the collapse of gas bubbles close to soft tissue.

In total 57 cases were simulated. The simulations presented, consider two different types of solid materials. The first is a uric type of kidney stone, a common type to be found in humans, which is treated by shock-wave lithotripsy. The second solid material considered corresponds to soft biological tissue with properties similar to kidney or liver. The parameters for the equation of state for the soft tissues and the kidney stone are calculated by matching the acoustic impedance and speed of sounds, in a similar approach to the work of Kobayashi et al. [80]. The material properties for the kidney stone, as required in the equivalent EoS 7 are; $\rho = 1546.0 \ kg/m^3$, $\pi_\infty = 8.37 \cdot 10^9 \ Pa$, $\gamma = 1.7$, and $\mu = 3.0 \cdot 10^9 \ Pa$. The values of the soft tissue properties are as follows: $\rho = 1060.0 \ kg/m^3$, $\pi_\infty = 0.69 \ GPa$, $\gamma = 4.3$, and $\mu = 1.0 \cdot 10^3 \ Pa$. As shown in the experimental work of [129] a polydisperse range of bubble sizes will nucleate and expand from the tensile part of the lithotripter's pulse. In such a dynamic phenomenon the radius and attachment/stand-off distance of the bubble will vary, and will not assume the contact angle dictated by the material's properties. Thus in this work, we consider an initially spherical air gas bubble with a radius varying from $10\mu m$ to $80\mu m$

and a stand-off distance in the range of $4.0 \cdot S/R_0$ to $-0.2 \cdot S/R_0$.

To facilitate comparisons, the same planar shock wave profile as the one used in the studies of [85],[174], [68] has been utilised. The shock wave is initialized by imposing the initial conditions for pressure, density, and velocity, according to the acoustic theory, placed at a distance $1.25R0$ upstream from the center of the bubble parallel to the wall boundary. The characteristics of the shock wave pulse as described by the Eq. 41 are: $\alpha = 1.48 \cdot 10^6 s^{-1}$, $\omega = 1.21 \cdot 10^6 s^{-1}$, $p_s = 35MPa$. The pressure p initialisation is then described as:

$$p(t) = p_0 + 2p_s e^{-\alpha t} cos(\omega t + \pi/3) \ . \tag{41}$$

The case discretization and AMR strategy implemented is identical to the one used in the validation case presented in Section 2.5. The maximum number of cells for each simulation exceeds 1 million cells during the collapse of the bubble. The equivalent number of cells per radius of the bubble remains at > 250. A non-adaptive discretization would require two orders of magnitude more grid points to sustain the same resolution of the moving flow structures and interfaces, thus making the computational cost of extensive parametric studies prohibitive. The full $3D$ resolution of the bubble collapse and the shock impact would require two orders of magnitude more grid points (≈ 180 times more) to keep the resolution of pressure waves and the interfaces at the same level, thus making the computational cost of extensive parametric studies prohibitive. To ensure numerical stability the time step is adjusted to a CFL number less than 0.1.

To facilitate the comparison among the different cases, and with other numerical studies, the results presented have been nondimensionalized against the initial bubble radius R_0, the Rayleigh collapse time t_R, where $t_R = 0.915 R_0 \sqrt{\frac{\rho_l}{\Delta p}}$, and the velocities and pressure scales as in [164],[85]:

$$p^* = \rho_l c_l^2, \quad u^* = \sqrt{\frac{\Delta p}{\rho_l}} \ , \tag{42}$$

where c_l is the speed of sound, Δp is the pressure difference between the bubble and the high pressure p_s of the lithotripter pulse, and ρ_l is the density of the liquid.

4.2.1 Shock-induced bubble dynamics near bio-materials

In this section, a brief overview of the principal physical mechanisms that dominate the shock-induced bubble collapse during shock-wave lithotripsy is given. The cases discussed correspond to a bubble with an initial radius of $R_0 = 0.02mm$, for three stand-off distances, i.e.: $S/R_0 = 1.2$, $S/R_0 = 0.6$, and $S/R_0 = -0.2$, that correspond to detached and attached bubbles respectively.

The time evolution of the collapse of a bubble induced by a shock wave impact for detached and attached bubbles is shown in Fig. 29 close to a kidney stone and in Fig. 30 close to a soft tissue. The sequence shown at the top row of each figure corresponds to detached bubbles with an initial stand-off distance $S/R_0 = 1.2$. The middle row in Figs. 29 and 30 depicts bubbles attached with an acute interface angle. The bottom row features attached bubbles with an obtuse angle. These figures effectively capture the sequence of events from the initial impact to the collapse and rebound of the gas bubbles.
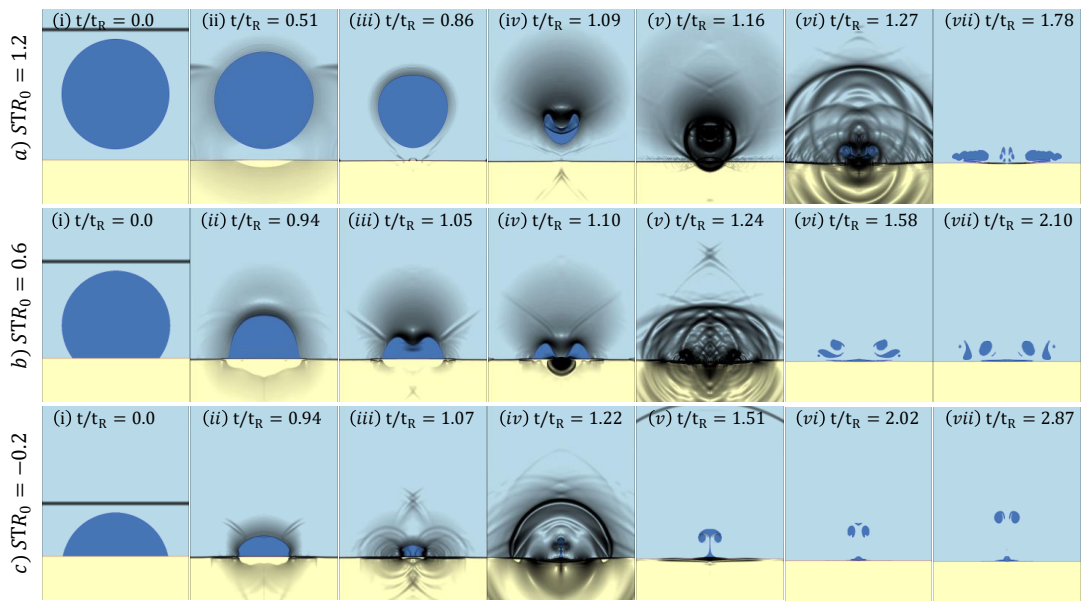
Figure 29: Shock-induced collapse of gas bubbles close to a kidney stone. Color map: represents the areas of different materials (gas/liquid/solid). The gray-scale colormap corresponds to the magnitude of the pressure field gradient. **(a(i))-(a(vii)):** detached gas bubble with initial stand-off distance $S/R_0 = 1.2$. **(b(i))-(b(vii)):** attached gas bubble with an acute interface angle and initial stand-off distance $S/R_0 = 0.6$. **(c(i))-(c(vii)):** attached gas bubble with an obtuse interface angle and initial stand-off distance $S/R_0 = -0.2$.

The dynamics associated with the kidney stone demonstrate complex interactions driven by the material's high elastic modulus and acoustic impedance. As shown in Fig. 29, upon the shock wave impact, the bubbles near the kidney stone collapse asymmetrically, leading

to the formation of high-pressure zones, liquid jet formation and subsequent toroidal shapes. These toroidal structures exhibit distinct phases of expansion and contraction, influenced by the shock waves reflected by the stone. Notably, upon the collapse the emitted shock waves from the bubble induces an intricate wave patterns within the stone, contributing to a multifaceted dynamic that includes high-pressure S, P, and head waves traversing the calculus. The visualization of these phenomena elucidates the interplay between the bubble's geometry, pressure dynamics, and the stone's material properties, underscoring the complex mechanics at play in the proximity of rigid solids.
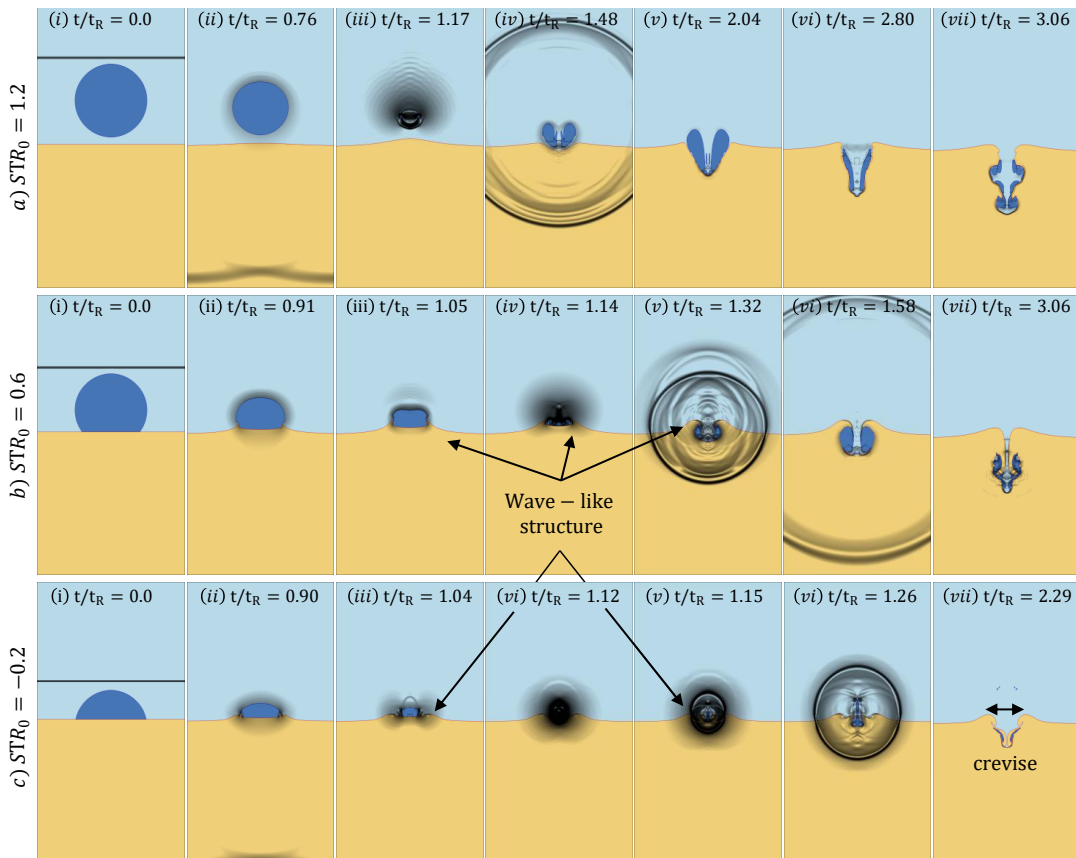
Figure 30: Shock-induced collapse of gas bubbles close to the soft tissue. Color map: represents the areas of different materials (gas/liquid/solid). The gray-scale colormap corresponds to the magnitude of the pressure field gradient. **(a(i))-(a(vii))**: detached gas bubble with initial stand-off distance $S/R_0 = 1.2$. **(b(i))-(b(vii))**: attached gas bubble with an acute interface angle and initial stand-off distance $S/R_0 = 0.6$. **(c(i))-(c(vii))**: attached gas bubble with an obtuse interface angle and initial stand-off distance $S/R_0 = -0.2$.

The collapse dynamics close to a soft tissue exhibit distinct characteristics, primarily influenced by the tissue's low shear modulus. This property results in a collapse process where tissue deformation intricately impacts the dynamics. As depicted in Fig. 30, the initial collapse phase is marked by the formation of a sink flow, which pulls the tissue into the collapsing

bubble, resulting in upward tissue movement and wave-like patterns on the tissue surface. This pattern formation is a direct result of the tensile forces at the interface between the gas bubble and the tissue. As the bubble contracts further to its minimum volume, these wave-like patterns become more pronounced, focusing the collapse dynamics within a crevice that forms at the interface. This focused collapse leads to an intensified penetration of the liquid jet into the tissue, driven by the radially collapsing bubble, which then morphs into a toroidal shape embedded within the soft tissue. Unlike the dynamics observed near kidney stones, the collapse near soft tissue shows a secondary collapse that is less intense, primarily due to the gas expansion and the tissue's ability to absorb and dampen the shock waves more effectively. This results in a less violent interaction, highlighting the influence of mechanical properties on the collapse behavior.

4.2.2 Influence of bubble's stand-off distance

In this section, we expand on the previous chapter 3 by considering a wider range of stand-off distances, starting from initially detached bubbles with a stand-off distance equal to $S/R_0 = 4.0$ and reaching attached bubbles with obtuse angles and stand-off distance: $S/R_0 = -0.2$. In total 12 stand-odd distances were selected. The stand-off distance distribution was selected to focus more numerical results on the limits of the various attachment configurations. Additionally, two parameters were kept constant; a. The shock wave amplitude, $p_s = 35MPa$, and b. the initial bubble size, $R_0 = 0.08mm$. The presented results from this parametric study are the following: the collapse time, the collapse position relative to the initial bubble placement, the maximum compression ratio of the bubble, the maximum deformation of the solid surface, the maximum liquid jet velocity that impacts the solid surface, and the maximum pressure on the solid's interface.

In Fig. 31a, we present the normalised collapse time as a function of the standoff distance for bubbles both detached from and attached to the surface of a kidney stone and soft tissue. For detached bubbles at a standoff distance $S/R_0 = 4.0$, the collapse time is $t/t_c = 1.465$. This time decreases to a minimum of $t/t_c = 1.385$ at $S/R_0 = 2.5$; then follows a power-law increase to $t/t_c = 1.444$ at $S/R_0 = 1.2$. Detached bubbles adjacent to soft tissue exhibit a consistent collapse time of $t/t_c = 1.51$. For attached bubbles to the solid surfaces, collapse times are normalised using an equivalent bubble radius computed from the initial gas volume. A linear relationship between collapse time and standoff distance is observed for both kidney stones and soft tissues, with a global maximum at $S/R_0 = 0.9$ and a minimum at $S/R_0 = -0.2$.

Fig. 31b illustrates the normalised displacement, on the axis of symmetry, of the bubble's centroid upon collapse, denoted by δx_{bubble}. This measure represents the shift from the bubble's initial center prior to the incident shock wave's impact to the centroid's position at t_c, the instant of minimal gas volume. With x_{bubble} is denoted the axis of symmetry. The computation of the centroid's position is defined by:

$$x_{bubble} = int_V x dV / V \tag{43}$$

For detached bubbles near a kidney stone surface, the displacement across the initial stand-off distances of $S/R_0 = 4.0$ and $S/R_0 = 2.5$ is found to be marginal. However, a pronounced power-law trend becomes evident as the stand-off distance decreases, with a marked propensity for the bubbles to collapse closer to the surface. In contrast, bubbles near soft tissue display a consistent centroid translation throughout. For bubbles attached to the surfaces of the solids, a linear relation is apparent between the collapse position and the stand-off distance, with maxima $\delta x_{\text{bubble}} = 0.84$ and $\delta x_{\text{bubble}} = 0.49$ reached for bubbles at a standoff distance of $S/R_0 = 0.9$, from a kidney stone and soft tissue, respectively.

Fig. 31c illustrates the correlation between the normalised bubble volume at the time of the collapse, t_c, and the standoff distance. For detached bubbles from the kidney stone surface, the minimum gas volume exhibits a power-law dependence on the standoff distance. This volume stabilizes for bubbles located at a standoff distance exceeding $S/R_0 = 2.5$, indicating a threshold beyond which the proximity to the solid surface has a diminished effect. When examining bubbles in closer proximity to the surface, it becomes evident that the minimum gas volume achieved is higher, reaching $0.141 V_c/V_0$. Consistent with earlier observations, bubbles adjacent to soft tissue reach a constant minimum volume. Conversely, bubbles with an acute interface angle affixed to the kidney stone surface demonstrate a markedly greater minimum volume equal to $0.21 V_c/V_0$. This trend is mirrored in the soft tissue scenario for bubbles at a standoff distance of $S/R_0 = 0.9$. When bubbles are further attached to solid materials, a linear relationship provides a good desciption of the behavior of the normalised minimum volume. The minimum volume is reached for bubbles with an obtuse angle and stand-off distance equal to $S/R_0 = -0.2$.

The maximum solid deformation versus the stand-off distance is presented in Fig. 31d. The maximum deformation is defined as $max \delta x_{solid}$, where δx_{solid} is measured on the center of the axis x i.e. $r/R = 0$, from the initial undeformed state, within a time-frame of $t/t_c = 2.5$ where t_c is the collapse time for each case. A significant contrast in the deformation
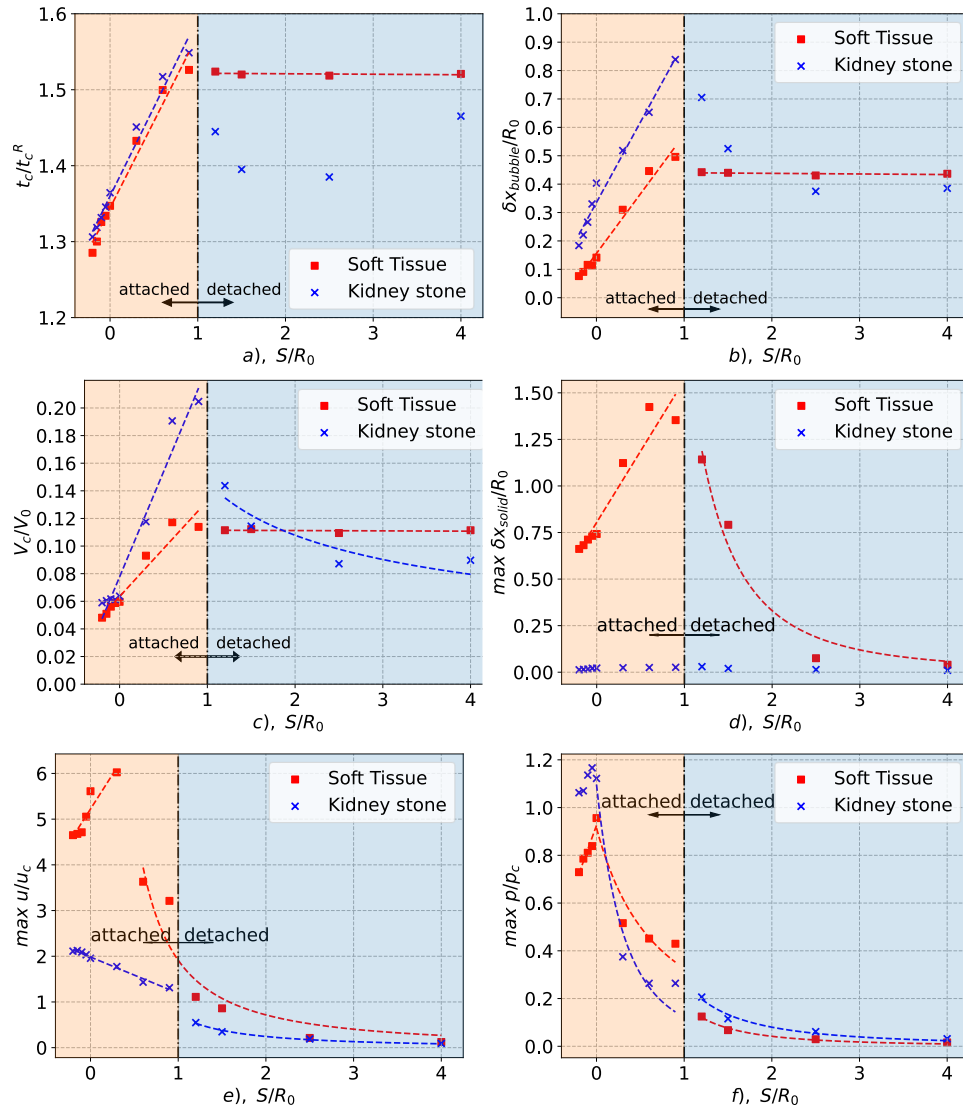
Figure 31: Effect of stand-off distance/attachment on bubble dynamics. **(a):** normalised collapse time with Rayleigh collapse time. **(b):** normalised bubble's collapse position in relation to the initial bubble center. **(c):** normalised gas volume V_c of the bubble at the initial collapse time t_c. **(d):** Maximum deformation of the solid interface at the axis of symmetry $r/R_0 = 0$. **(e):** Maximum velocity at the solid boundary interface overtime at $r/R_0 = 0$. **(f):** Maximum pressure on the solid interface due to the primary shock wave emission.

mechanics of soft tissues and kidney stones is observed. Notably, for all cases, the soft tissue deformation is found to be up to two orders of magnitude greater than that of the kidney stone. For bubbles with a stand-off distance less than $S/R_0 < 2.5$, the maximum deformation remains constant. Moreover, it was found that detached bubbles in proximity to soft tissue displayed a power law relationship between deformation and stand-off distance, reaching a maximum value at $S/R_0 = 1.2$. The maximum deformation is reached for attached bubbles with acute interface angles to the soft tissue, and stand-off distance equal to $S/R_0 = 0.6$. For bubbles further attached to the soft tissue, a linear approximation was found to be true, with the maximum deformation reached for bubbles attached with an obtuse angle and stand-off distance $S/R_0 = -0.2$.

Fig. 31e explores the maximum normalised jet velocity against the standoff distance at the solid boundary. The velocity time series are acquired by a Lagrangian sensor tracing the solid interface along the symmetry axis at $r/R_0 = 0$. The data indicates a power-law dependency between the jet velocity and standoff distance for bubbles that are initially detached from both types of solid materials. Notably, bubbles collapsing near soft tissue exhibit higher velocities. For attached bubbles, the behavior diverges between the two materials. With soft tissue, the maximum jet velocity is observed in bubbles attached at an acute angle with a standoff distance of $S/R_0 = 0.3$. Conversely, for kidney stones, an ascending linear trend in velocity is discernible with increased attachment to the solid, culminating in a maximum velocity ratio of $u/u_c = 2.16$ at a standoff distance of $S/R_0 = -0.2$.

To ascertain the peak pressure at the solid boundary during bubble collapse, we employed the same Lagrangian sensor as described previously. Fig. 31f presents the relationship between maximum pressure and standoff distance. The findings indicate an inverse power law relationship with the stand-off distance, with bubbles in closer proximity and attached to solid surfaces emitting stronger shock waves. In detail, we found that detached bubbles emit stronger shock waves when near stiffer solids. However, this trend inverts for bubbles attached at acute angles. At a perpendicular orientation (90°) to the solid interface, the dynamic changes, with stiffer materials experiencing higher shock wave pressures. Beyond this angle, there is a decline in shock wave amplitude for both materials.

4.2.3   Effect of initial bubble size on bubble dynamics

The effect of the initial bubble size on the shock-induced gas bubble dynamics close to either a kidney stone's surface or to a soft tissue is examined in this section. Utilizing the Rayleigh

collapse time t_R, the pressure amplitude of the shock wave pulse p_s, a typical length and the speed of sound within a kidney stone, we can estimate the size of bubbles that will collapse in the time lapse of the shock wave passage from the kidney stone and the surrounding medium. The Rayleigh collapse time is defined as the time required by a spherical gas bubble with initial radius R_0 to collapse in an incompressible and inviscid fluid with density ρ_l under a uniform pressure difference of Δp. For p_s equal to $35MPa$ surrounded by water in atmospheric pressure, the Rayleigh collapse time is:

$$t_R = 0.915R_0\sqrt{\frac{\rho_l}{\Delta p}} \Rightarrow t_R = 0.004897R_0 \tag{44}$$

The typical sizes of kidney stones treated with ESWL are in the range of $< 5mm$. Thus a length equal to $3.5mm$ and longitudinal speed of sound equal to $3471m/s$ are typical values for these stones. Thus the time required for the shock to propagate within the stone is $1.01\mu s$. Thus from Eq. 44 we can estimate that bubbles with an initial radius smaller than $80\mu m$ will have enough time, to collapse $t > 2.5t_c$, form the liquid jet and impact the surface of the solid materials. In the work of Wang [174] a parametric study was presented aiming to address the question of bubble sizes that collapse during a similar time lapse as the propagation of a shock wave through a kidney stone with a size equal to $1.5mm$. It was found that bubbles with a radius larger than $R_0 > 0.13mm$ do not collapse in the same time.

In the present study, we expand the investigation to smaller radii starting from $R_0 = 80\mu m$ and by halving the radius three times, we reach the end of the distribution with $R_0 = 10\mu m$. Additionally, three stand-off distances from the two solid materials were studied for the various bubble sizes. These distances correspond to detached bubbles, attached with acute and obtuse interface angles. The shock wave utilized in this study is identical to the one used in the previous parametric analysis, thus minimizing the unknown factors and enabling further comparisons. In total 24 cases are analyzed for this parametric study.

In Fig. 32a and 32b, the relation between the normalised collapse time and the initial bubble size for the two solid materials is presented. In both cases, linear relationships are found between the two, with smaller bubbles collapsing faster. In the case of the kidney stone, bubbles attached with an obtuse angle, collapse slower than detached or attached with an acute angle. In the case of the soft tissue, similar linear relations are found, with bubbles detached from the soft tissue collapsing slower, followed by the attached with an acute and finally by an obtuse interface angle.
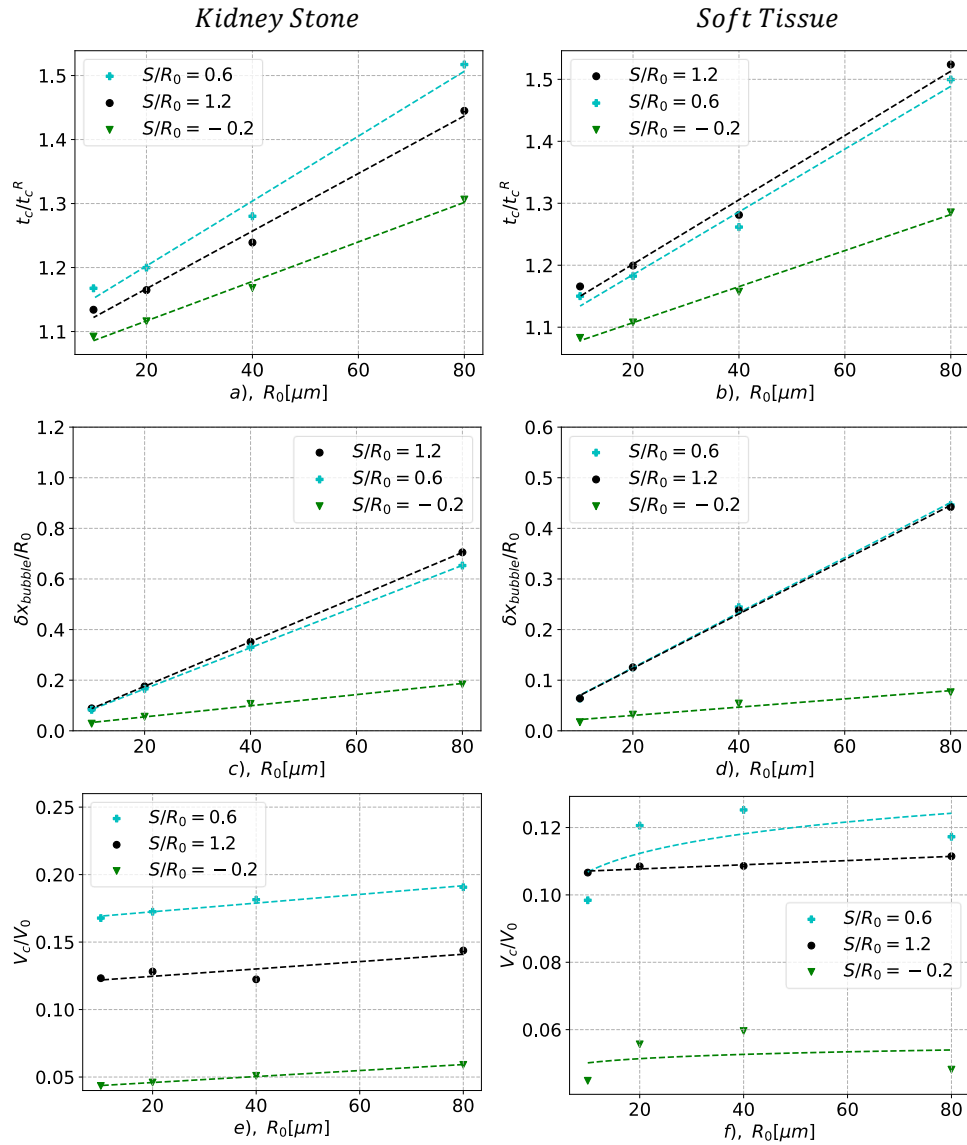
Figure 32: Effect of initial bubble size and attachment configuration on bubble dynamics. **(a):** Normalised collapse time with Rayleigh collapse time for kidney stones and **(b)** for soft tissue. **(c):** Normalised bubble's collapse position close to a kidney stone surface in relation to the initial bubble **(d)** close to soft tissue. **(e)** Normalised gas volume V_c of the bubble at the collapse time t_c close to a kidney stone and **(f)** close to soft tissue

In Fig. 32c and 32d, the collapse position of the bubble's centroid relative to the initial position versus the initial bubble size, is presented. In the case of the kidney stone, both detached and attached bubbles with an acute angle exhibit a similar, linear decrease in the collapse position relative to bubble size, meaning larger bubbles tend to collapse closer to the solid surface. For bubbles attached with an obtuse angle a similar behavior is found. For the bubbles collapsing close to the soft tissue boundary a similar dynamic is presented in Fig. 32d. The detached and attached bubbles with an acute angle are collapsing in the same positions with a difference of less than 2%. For the attached bubbles with an obtuse angle, the same dynamics are found, similar to the kidney stone's case. The translation of the bubble centroid is found to be greater, for bubbles close to the kidney stone, for all initial bubble sizes.

The relation of the minimum normalised gas bubble's volume at the time of the collapse t_c with the bubble size is shown in Fig. 32e and 32f. In the case of the kidney stone, linear decreasing relations are found for all attachment configurations, with smaller bubbles reaching lower gas volume during the collapse. The higher compression is found for bubbles with an obtuse interface angle, followed by detached and by those attached with an acute angle to the kidney stones' surface. In the case of soft tissue, a different collapse dynamic in relation to the minimum gas volume is observed. For detached bubbles, a constant minimum volume is reached for all bubble sizes. For attached bubbles with both obtuse and acute interface angles, a local maximum in the gas volume is found for bubbles with an initial size equal to $R_0 = 40\mu m$. Both smaller and larger bubbles tend to be compressed further in either case of attachment to the soft tissue.

In Fig. 33a and 33b the maximum deformation of the solid interface in relation to the initial bubble size and attachment is presented. It is found that the maximum deformation of the kidney stone is one order of magnitude less than the soft tissue. In the case of the former, we found that detached bubbles produce the maximum deformation followed by attached bubbles with an acute interface angle, and finally by the bubbles attached with an obtuse angle, for all bubble sizes. Inverse power law relations are apparent between the deformation and the bubble size, for all attachment configurations. In the case of soft tissue, similar inverse power law relationships are found. Specifically, the detached bubbles with an initial radius $10\mu m$ are found to induce the greatest deformation. For a larger initial radius, the attached bubbles with an acute interface angle are found to greater deform the soft tissue, followed by the detached and finally by the attached with an obtuse interface angle.

The relation of the maximum velocity of the solid interface in relation to the bubble size is shown in Figs. 33c and 33d. For the kidney stone cases, an inverse power law relation to

the bubble size is found for both detached and attached bubbles. Similar findings to the first parametric case are evident, with bubbles attached with an obtuse angle producing the higher jet velocities, followed by those with an acute angle, and the detached bubbles. In the case of the soft tissue, the same dynamics are apparent, with the smaller attached bubbles with an obtuse angle, producing the greatest jet velocities.

In Figs. 33e and 33f, the maximum normalised pressure on the solid boundary, as it is captured by the Lagrangian sensor is presented. An inverse power law relation is found for all bubble sizes and attachment configurations. In the case of the kidney stone, higher shock wave emissions are found for attached bubbles with an obtuse angle. For detached bubbles and attached with an acute angle similar shock wave emissions are observed. In the case of the soft tissue, similar inverse power law relationships are found, for all attachment configurations and bubble sizes. The primary distinction between the two materials lies in the differnce of shock wave emission for bubbles attached with an acute interface angle.

4.2.4   Effect of pulse's amplitude

We next investigate, the influence of the shock wave amplitude on the bubble collapse dynamics close to a soft tissue. The selection of the solid material is justified as the deformation and the penetration mechanics of the liquid jet are greatly influenced by the bubble's pressure loading. In the case of more rigid solids, the penetration from the liquid jet and the gas bubble as shown in the previous parametric studies is orders of magnitude smaller. In principle, there are various shock wave profiles used in shock wave lithotripsy [176, 41], however, the amplitude is a determinant factor in the bubble collapse dynamics, alongside potential tissue damage, from induced shear stresses [42]. Thus in this study, we limit the investigation to the shock-wave profile used in the previous 2 parametric studies with varying amplitude. The range of overpressure starts from $p_s = 20MPa$ and reaches $p_s = 180MPa$ with a $40MPa$ interval, for the three different attachment configurations close to soft tissue. The initial bubble size was kept constant and equal to $80\mu m$ to enable comparison with the previous studies. In total 18 cases were investigated.

In Fig. 34a, the effect of the amplitude of the pulse on the normalised collapse time is presented. For small shock wave amplitudes, i.e. $20MPa$ to $60MPa$, the normalised collapse time follows an inverse power law relation. Bubbles that are attached to the solid surface demonstrate an expedited collapse phase. For higher than $60MPa$ shock wave amplitudes, it is found that the normalised time of the collapse remains constant for both attached and
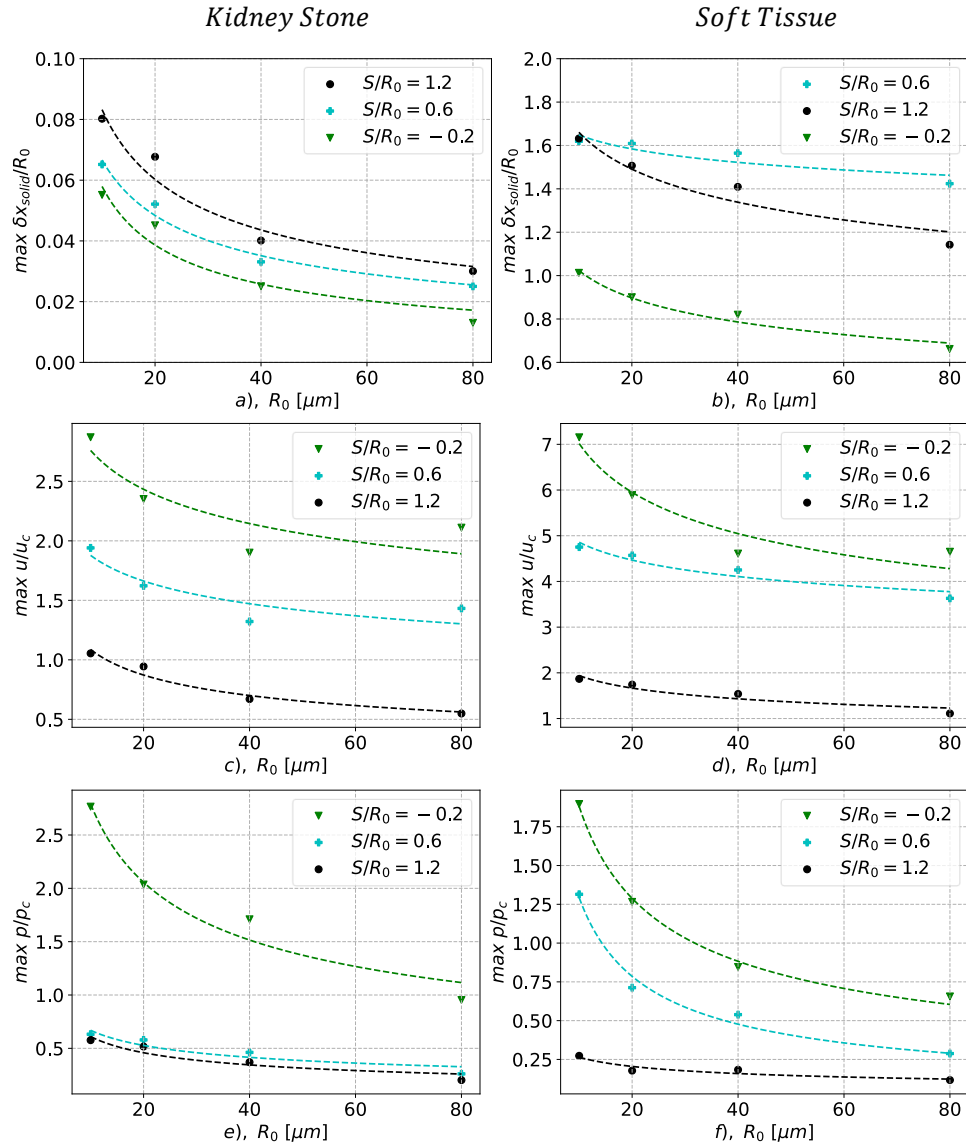
Figure 33: Effect of initial bubble size and attachment configuration on bubble dynamics. **(a):** Maximum deformation of the kidney stone's interface at the axis of symmetry $r/R_0 = 0$ and **(b)** of the soft tissue's interface. **(c):** Maximum velocity at the kidney stone's interface overtime at $r/R_0 = 0$ and **(d)** at the soft tissue's. **(f):** Maximum pressure on the kidney stone's interface due to the primary shock wave emission and **(e)** on the soft tissue's interface.

detached bubbles.

The collapse position of the bubble versus the shock wave's amplitude is presented in Fig. 34b. Power law increase relationships are observed for detached and attached bubbles with an acute interface angle. For shock wave amplitudes higher than $\approx 36MPa$ detached bubbles collapse closer to the soft tissue surface. For attached bubbles with an obtuse angle, a linear relationship is apparent in the same figure.

The relation of the minimum normalised gas bubble's volume at the time of the collapse t_c with the pulse's amplitude is shown in Fig. 34c. In general, it is found that higher shock wave amplitudes drive the bubbles into higher compression at the collapse stage, for all attachment configurations. This seems to hold true for amplitudes up to $100MPa$, in the case of detached bubbles, with higher amplitudes not resulting in higher compression of the gas bubble. In the case of the attached bubbles with an acute interface angle to the soft tissue, the amplitude for which the higher compression is reached is $60MPa$ with higher amplitudes reaching slighter lower ratios. This upper limit in the compression ratio is not found for bubbles attached with an obtuse angle to the solid surface, with an inverse power law relation apparent.

The maximum soft tissue deformation with respect to the initial undeformed state versus the pulse overpressure is presented in Fig. 34d. The influence of the shock wave amplitude in these relations is apparent, with stronger pulses driving the collapsing bubbles and the liquid jet further into the soft tissue. For lower shock wave amplitudes, up to $100MPa$, collapsing bubbles attached with an acute interface angle, result in the highest deformation of the soft tissue. For higher shock wave amplitudes than $100MPa$ detached bubbles in close proximity to the soft tissue penetrate the soft tissue further. Bubbles with an obtuse angle deform the soft tissue significantly less than the other two types of attachment.

In Fig. 34e, the relation between the pulse's overpressure and the maximum normalised jet velocity on the soft tissue's boundary is presented. It should be noted that the normalization of the maximum jet velocity is computed based on the amplitude of each shock wave. For detached bubbles, an exponentially decaying relation is found. Such is not the case for the attached bubbles with an acute angle to the soft tissue. In this case, the maximum normalised jet velocities are found for the weaker shock waves. In absolute values, however, this is not the case, as the non-normalised velocity exhibits an exponentially decaying relation. Finally, for attached bubbles with an obtuse angle, a linear-constant relation is found between the two variables, indicating a linear relation between the maximum jet velocity of the liquid jet and the square root of the shock wave amplitude (see normalization equation 42).

The last parameter shown in Fig. 34f, is the maximum normalised pressure on the solid boundary as it is captured at the soft tissue interface, located on the axis of symmetry $r/R_0 = 0$. It should be noted that the normalization parameter p_c is constant for all cases. For all shock-wave amplitudes, the obtuse attached bubbles emit the highest shock waves, followed by the attached with an acute and finally by the detached bubbles. A linear relationship is found for the first. For the other two inverse power law relations are apparent in the same figure.

4.3   Discussion

This section delves into the interpretation of the results highlighted in the previous Section 4.2. Fundamentally, several physical mechanisms govern the dynamics and mechanics of shock-induced bubble collapses. The effect of the most influential is discussed, elucidating their effect on the various key characteristics of the bubble collapses.

The acoustic impedance difference between the liquid in which the shock wave is propagating and the solid interface close to the collapsing bubble results in various effects on the collapse mechanics. In principle, the reflection of the shock wave on the solid surface is related to the ratio of the longitudinal acoustic impedance between the two materials. For $Z/Z_0 < 1$, where Z is the acoustic impedance of the solid material and Z_0 is that of the liquid the reflection will be a tensile wave, decelerating the collapse of the bubble. Conversely, for $Z/Z_0 > 1$, a compressive shock wave is reflected, intensifying the impact on the bubble interface and thus accelerating the collapse [25, 85]. In this study, the acoustic impedance ratios for kidney stones and soft tissue are $Z/Z_0 = 3.93$ and $Z/Z_0 = 1.09$, respectively, indicating that both materials reflect compressive shock waves. The reflected shock wave amplitude as measured in the numerical simulations is $p_r = 19.9 MPa$ for the kidney stone cases and $p_r = 3.1 MPa$ for the soft tissue cases, both for an incident shock wave amplitude equal to $35 MPa$.

The additional pressure loading of the bubble interface leads to faster collapse times as can be seen in Fig. 31a, for all stand-off distances of detached bubbles. The same relationship is found in Figs. 32a and 32b, for all detached bubble sizes. Additionally, this increased pressure loading results in: (a) elevated compression ratios for bubbles situated at $S/R_0 > 2.0$, as depicted in Fig. 31c, and (b) higher shock wave emissions, as evidenced in Fig. 31f. In the work of Philip et al. [127] it is noted that the collapse time is not in general linear dependent on the bubble diameter, as the tensile part of the lithotripter pulse will affect the pressure loading. While this is applicable for larger diameters; however, in our study, the selected range
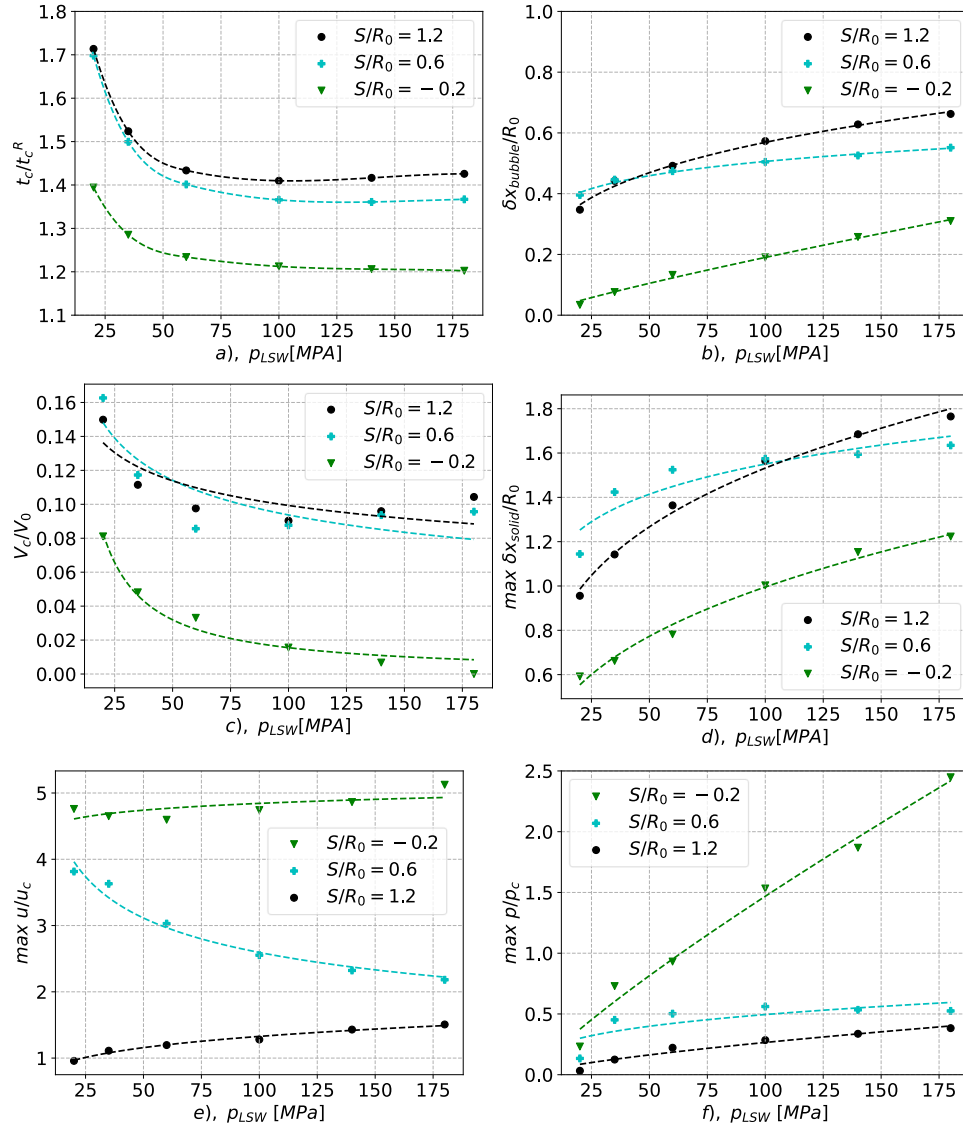
Figure 34: Effect of shock-wave amplitude on the bubble dynamics close to a soft tissue. **(a):** normalised collapse time with Rayleigh collapse time. **(b):** normalised bubble's collapse position in relation to the initial bubble center. **(c):** normalised gas volume V_c of the bubble at the initial collapse time t_c. **(d):** Maximum deformation of the solid interface at the axis of symmetry $r/R_0 = 0$. **(e):** Maximum velocity at the solid boundary interface overtime at $r/R_0 = 0$. **(f):** Maximum pressure on the solid interface due to the primary shock wave emission.

of bubble sizes is not affected by the negative tensile part of the pulse.

Apart from the reflection from the solid/fluid interface, the gas bubble interface also reflects the incident shock wave. When the bubble is placed sufficiently close to the solid surface a shielding effect is evident. The area of the solid surface close to the proximal face of the bubble is not impacted by the incident shock, as can be seen in Fig. 29b. Similar shielding phenomena have been identified in numerical studies of cavitation [104] and are corroborated by in vivo studies pertaining to medical interventions, including High-Intensity Focused Ultrasound (HIFU) and Extracorporeal Shock Wave Lithotripsy (ESWL) [128, 34].

The shielding effect's influence is evident when examining the relationship between collapse position and standoff distance, as shown in Fig. 31b. The shrinking motion of the bubble during the collapse, coupled with the shielding of the area in between the solid and the bubble creates a low-pressure area. This low-pressure area exacerbates the pressure differential during the collapse, driving the bubble to collapse closer to the solid surface. For soft tissues, however, the significantly weaker reflection amplitude—lower by an order of magnitude—leads to a more uniform pressure distribution in all cases, resulting in consistent collapse positions regardless of standoff distance for the detached bubbles.

The combined effect of the increased pressure loading and the shielding effect is discernible in Fig. 31a, where the shortest collapse time is found for bubbles with a stand-off distance equal to $S/R_0 = 2.5$. Bubbles closer to the solid surface, reduce the additional pressure loading from the reflection due to the shielding of the adjacent area of the solid surface. Additionally, the impact of pressure loading diminishes for bubbles situated at greater distances from the solid surface, owing to the increased travel path of the reflected wave. This dual influence also accounts for the reduced compression ratios observed in Fig. 31c for bubbles collapsing near the kidney stone. Conversely, for bubbles adjacent to soft tissue, such dynamics are not apparent, as the soft tissue's minimal compressive wave reflection exerts a negligible effect on the incident shock wave.

As previously mentioned the dynamics of bubble collapse for attached bubbles to solid surfaces vary depending on the angle of attachment, among other factors. Specifically, bubbles attached at acute interface angles induce a localized low-pressure zone around the interface during the collapse. This area is formed as an effect of the collapse the bubble which is rapidly shrinking with an interface velocity, having a component "which tends to detach the liquid from the wall" [86]. Consequently, this interfacial velocity creates a depressurised area around the interface which drives the collapse closer to the surface of the solid. The rigidity of the

solid also plays a pivotal role; stiffer materials like kidney stones maintain their shape, causing the bubble to slide on the interface. Conversely, as discussed in 3, soft tissue responds to this depressurisation by forming a wave-like structure during the bubble's collapse, which can be observed in Fig. 30.

The emergence of the wave-like structure and the depressurization of the liquid may affect various characteristics of the collapse mechanics. As evidenced in Fig. 31a, a significant increase in the collapse time is observed when comparing detached bubbles to those attached at an acute interface angle with kidney stone surfaces. This increase can be attributed to the depressurization of the liquid surrounding the bubble interface, which diminishes the pressure gradient essential for driving the collapse near the interface. The contrast in collapse times between kidney stones and soft tissues within the same figure further underscores the significance of this mechanism; the increment is less pronounced with soft tissues, which can adapt and conform to the bubble's contraction, thereby lessening the extent of liquid depressurization. This correlation persists across all bubble sizes, as presented by Fig. 32a.

Furthermore, this physical mechanism drives the collapse position closer to the solid wall, as demonstrated in Fig. 31b. The inherent stiffness of materials like kidney stones drives the bubbles to collapse closer to the solid interface. This relationship persists irrespective of bubble size, as evidenced by the data in Fig. 32c and d. Additionally, bubbles that are further attached to solid interfaces tend to collapse closer to their initial position due to (a) the constrained space and (b) the diminishing influence of depressurization with greater attachment angles. Specifically, as the attachment angle widens, the component of velocity normal to the interface diminishes linearly, thus the depressurization effect is less pronounced, which is illustrated in Fig. 31a.

As detailed in Section 4.2, and presented in Fig. 30b(iv) and 30b(v), a wave-like structure is forming during the collapse phase of attached bubbles. This structure gives rise to a circular crevice, which confines the bubble collapse. Consequently, the liquid jet is focused within the crevice and is oriented perpendicularly to the soft tissue interface. The effects of this mechanism are depicted in Fig. 31d, where the maximum deformation corresponds to bubbles with an acute angle of attachment. This effect attenuates with increasing attachment angles, consistent with the observations previously discussed. The phenomena extend across all bubble sizes and pulse amplitudes, as corroborated by Figs. 33b and 34d. Additionally, in Fig. 31e, the maximum jet velocity is found for bubbles with a stand-off distance equal to $S/R_0 = 0.3$. Notably, this entrapping of collapse also intensifies shock wave emissions for bubbles acutely attached to soft tissues compared to those near kidney stones, as illustrated in Fig. 31f.

Two principal characteristics of bubble collapse adjacent to either soft or rigid boundaries are the pressure rise during the collapse phase and the direction of the resultant liquid jet. Detached bubbles and attached bubbles with an acute interface angle exhibit an axial collapse mechanism as presented in section 4.2 and in Figs. 29a-b and 30a-b. Conversely, bubbles further attached to the solid boundary demonstrate a radial collapse mechanism, as depicted in Figs. 29c(i)-c(vii) and 30c(i)-c(vii). Similar findings have been reported in the literature [86, 89].

Commencing with Fig. 31b, the displacement of the bubble's centroid is found to be minimized for bubbles attached with an obtuse interface angle. This is directly attributed to the radial collapse mechanism. The same relation is apparent in Figs. 32c and 32d, for both solid materials and initial bubble sizes. Furthermore, Fig. 34b demonstrates that this relationship holds true across a range of shock wave amplitudes.

As illustrated in Fig. 29b(iii) and b(iv), during the collapse of attached bubbles with an acute angle and stand-off distance $1 > S/R_0 > 0$, a torus remains attached to the solid surface at the collapse time t_c. This is a consequence of the radial velocity being substantially lower than that of the axial velocity of the distal face of the bubble which is collapsing towards the solid surface. The resulting axial liquid jet strikes the solid and expands out radially, leading to substantial gas compression within the torus in subsequent stages. This phenomenon results in lower observed compression ratios for such attachments, as depicted in Fig. 31c and further corroborated by Fig. 32e. Notably, this effect is absent in soft tissue interactions, as indicated in Fig. 30b(iv), where the collapsing bubble induces a flow that deforms the attached tissue. This hypothesis is further substantiated by the data in Figs. 31c, 32f, and 34c.

In Figs. 31d, 33a-b, and 34d, the maximum deformation, is found to be reduced for bubbles attached with an obtuse angle to both solid materials. This diminution is ascribed to the radial collapse mechanism, where the liquid jet, initially developing along the bubble's circumference, undergoes a stark directional shift upon convergence at the axis center. It then bifurcates, moving simultaneously towards and away from the solid interface. Consequently, the deformation induced by this liquid jet is less pronounced when contrasted with that caused by detached bubbles or those attached at an acute angle, where the jet's perpendicular impact with the solid surface leads to greater deformation.

For detached bubbles, the extent of maximum deformation is governed primarily by two factors: (a) the material properties of the solid boundary, and (b) the proximity of the liquid jet to the solid surface, as elucidated in Fig. 31b and d. The high shear and elastic modulus

of the kidney stone minimises the maximum deformation induced by the shock impact and the liquid jet. In Fig. 31d and in more detail in Fig. 33a and b, we show that the maximum deformation of the kidney stone interface is one, and in some cases, two orders of magnitude less than the soft tissue's. Furthermore, the soft tissue elasticity influences the compression ratio of attached bubbles during the collapse. This is exemplified in Fig. 32f, where a localised peak in gas volume compression is identified for bubbles initially sized at $R_0 = 40\mu m$. Bubbles of both smaller and larger radii tend to be further compressed.

Moreover, the proximity of the collapse position for detached bubbles to the solid interface correlates with an increase in shock wave emissions and liquid jet velocities, as depicted in Figs. 31e and 31f. The inherent rigidity of the kidney stone, results in diminished liquid jet velocities on the solid's interface as seen in the same figures. For attached bubbles to the kidney stone surface, the radial collapse mechanism results in higher shock wave emissions from the water hammer and greater velocities, as indicated in Fig. 31e and f. This enhancement is additionally attributed to the collapse's proximity to the solid boundary and the limited space available for the expansion of the compressed liquid. Conversely, while the radial collapse mechanism near soft tissues similarly boosts shock wave emissions and liquid jet velocities, the entrapment of the collapse, for bubbles attached with an acute angle, yields even higher pressure and velocity.

The initial gas volume of the bubble is a critical factor influencing the collapse characteristics. Notably, the normalised collapse time—a ratio of the collapse time t_c to the Rayleigh collapse time t_R—exhibits a linear increment with the standoff distance for attached bubbles to a surface, as illustrated in Fig. 31a. A similar relationship is demonstrated between the normalised time and the initial bubble radius in Fig. 32a and 32b. This relationship can be explained as the shock wave advances at a constant speed while it impacts the bubble. Consequently, smaller bubbles experience a more even distribution of pressure across their surface, fostering a more spherical collapse. This results in a collapse time that more closely approximates the Rayleigh collapse time t_R, and a collapse position that is nearer to the bubble's original center, as evidenced in Fig. 32c and 32d.

Detached bubbles with a smaller initial radius placed at the same stand-off distance will be in closer proximity to the solid surface. As a result, the collapse position will be closer to the interface. Thus, the ensuing water hammer shock wave and the liquid jet are likely to produce higher pressures and velocities upon the solid interface, causing more pronounced deformation. These phenomena are depicted across Fig. 33a-f. Similar findings were reported in the work of Wang et al. [174]. Similarly, bubbles attached to the solid surface with smaller

initial radii exhibit analogous dynamics by concentrating the collapse's momentum and energy at the axis's center. This is the point at which the Lagrangian sensor records the jet velocity and pressure, confirming that the collapse's localized intensity engenders comparable effects, as illustrated in Figs. 33c-f.

The last parameter investigated is the pulse amplitude effect on the collapse dynamics for bubbles close or attached to a soft tissue. In general, higher pressure differences will result in faster and more violent collapses. The ratio of the shock-induced collapse time t_c to the theoretical spherical collapse time t_R was found to remain constant for pulse amplitudes exceeding $100 MPa$, as demonstrated in Fig. 34a. Notably, for each attachment configuration, a different limit in this ratio is reached. The unnormalised collapse time can be approximated by $t_c = a \cdot t_c^R$, with $a = 1.30$ for detached bubbles, $a = 1.27$ for bubbles attached at an acute angle, and $a = 1.13$ for those with an obtuse angle of attachment. Here, t_c^R is derived from the initial gas volume, representing the equivalent spherical bubble radius. Consequently, at higher shock wave amplitudes, the collapse time tends to approach that of a spherical bubble collapsing under uniform pressure. This trend is further attributed to the pulse waveform, where elevated shock wave profiles yield an expanded high-pressure region, resulting in a more uniform application of pressure

Fundamentally, stronger shock wave amplitudes drive the collapse of the bubble closer to the soft tissue, for both detached and attached bubbles as evidenced in Fig. 34b. This trend could have been anticipated, given that higher pressure differentials at the fluid-gas interface induce greater velocities toward the direction of the shock wave propagation, resulting in collapse positions closer to the soft tissue.

During the collapse of attached bubbles with an acute interface angle a radial collapse mechanism emerges, similar to the one presented for a bubble attached with an obtuse angle. This mechanism is significant for shock wave amplitudes below $35 MPa$. This radial collapse mechanism contributes to the bifurcation of the bubble into two toroidal segments, thereby leading to a pin-type collapse pattern. This mechanism also results in higher normalized liquid jet velocities as depicted in Fig. 34e. It should be noted that the normalization of the jet velocities, with the higher shock wave amplitudes, coupled with the needle-type component results in the apparent slower normalized jet velocities for higher shock wave profiles. Furthermore, the depressurization during the collapse might act as a stabilizing process for the jet formation and resulting jet velocity. Moreover, it was discerned that higher shock wave amplitudes of the lithotripter, affect significantly the shock wave emissions from attached bubbles with an obtuse angle, in contrast to the two other attachment configurations.

4.4   Conclusions

This numerical study presented in this chapter provides a comprehensive analysis of the shock-induced collapse dynamics of gas bubbles in proximity to solid interfaces. In total three parametric studies are demonstrated, i.e.: the effect of standoff distance, the effect of bubble size, and the effect of the lithotripter's pressure amplitude, for soft and rigid representative bio-materials. Our research has uncovered several crucial factors that dictate the collapse mechanics, which are of particular significance for applications in medical procedures like High-Intensity Focused Ultrasound (HIFU) and Extracorporeal Shock Wave Lithotripsy (ESWL).

Key findings from our parametric studies include:

- The acoustic impedance ratio Z/Z_0 between the liquid medium and solid interfaces is a critical factor in the collapse mechanics. The amplitude of the reflected compressive shock wave for ratios $Z/Z_0 > 1$ contributes to the acceleration of the bubble collapse. The collapse times are influenced by the additional pressure loading from the reflected shock wave and the shielding effect due to the bubble's proximity to the solid surface. These factors result in faster collapse times for detached bubbles at greater stand-off distances from the interface.

- The collapse dynamics vary significantly with the bubble's attachment angle to the solid surface. Bubbles attached to the solid interface, collapse faster and in closer proximity to the solid. They reach higher compression rations, induce higher jet velocities, and emit higher shock wave emissions. Bubbles attached with an acute interface angle, penetrate further the soft tissue in the same time frame, than detached or attached bubbles with an acute angle.

- The mechanical properties of the solid material significantly influence the dynamics of bubble collapse. Bubbles attached to rigid materials such as kidney stones collapse closer to the interface and do not deform significantly the interface, while softer materials like tissues exhibit different collapse behaviors due to their capacity to deform and follow the motion of the collapsing bubble.

- The initial gas volume within the bubble dictates the collapse characteristics, with smaller bubbles collapsing more spherically and closely mirroring the theoretical Rayleigh collapse time t_R. Smaller initial radii place bubbles in closer proximity to the solid surface thus resulting in higher shock wave emissions and liquid jet velocities.

- Higher shock wave amplitudes lead to a collapse time that is closer to a spherical bubble under uniform pressure. Lower shock wave amplitudes of the lithotripter pulse introduce a radial collapse mechanism to attached bubbles with an acute interface angle, leading to higher liquid jet velocities.

In summary, the results of this chapter have delineated the intricate interplay between bubble size, standoff distance, solid material properties, and shock wave amplitude on bubble collapse dynamics. These results can further our understanding of the intricate interplay of the fluid-solid interaction of collapsing bubbles and have important implications for enhancing the efficacy and safety of medical procedures that utilize cavitation phenomena. It's important to note that the results presented are only applicable under the specific conditions that were studied and further investigations are required to fully elucidate the 3-dimensional collapse mechanics close to soft materials and complex geometries, and the interaction of bubble clouds with soft and rigid bio-materials.

5   Numerical investigation of needle-free injection

In this chapter, the results of a numerical investigation on the mechanics of needle-free jet injectors (NFJIs) are presented. In particular, the focus will be on the interaction between a high-velocity liquid jet and materials with properties close to the oned of human skin. The previous chapter's 6-equation pressure disequilibrium Diffuse Interface Model (DIM) is utilised and modified to incorporate Fluid-Structure Interactions (FSI), allowing for precise modeling of the complex interplay between the injected fluid and the tissue. The model is validated through two-dimensional axisymmetric simulations of a needle-free device, utilising available experimental and numerical data. To this end, a study is conducted into the influence of initial conditions on the liquid jet velocities. We further elucidate the underlying dynamics of laser-induced bubble growth and jet formation. Employing, four types of skin-like materials, the jet impact and penetration mechanics of the solid, including stress development on the skin are analyzed. Our findings reveal the significance of material properties on jet penetration and dispersion, offering insights into enhanced drug delivery methods. The outcomes not only advances our understanding of the physical processes governing needle-free injection systems but also contributes to the development of more effective numerical tools for NFJIs.

5.1   Background

The innovative technology of needle-free jet injectors (NFJIs) represents a significant stride forward in medical therapeutics, primarily due to its multifaceted advantages in addressing key healthcare challenges. NFJIs drastically reduce the risk of cross-contamination, a vital factor in curbing the spread of blood-borne pathogens [75]. The elimination of needle disposal requirements with NFJIs significantly reduces medical waste and the environmental impact associated with traditional syringes [76]. It is estimated that 11.5 to 66 million people in the United States experience needle phobia which affects vaccination campaigns such as during the COVID-19 pandemic [102]. These systems particularly address needle phobia by eliminating the fear associated with traditional needle-based injections, thereby enhancing patient compliance and comfort [12]. Additionally, NFJIs eliminate needlestick injuries, a critical improvement in healthcare worker safety [71]. The rapidity of drug delivery is another notable advantage, as NFJIs enable swift administration of medications, contributing to more effective treatment outcomes [110]. This technology also opens the door to self-administration, providing patients with a convenient and less intimidating method of medication delivery [78]. Remarkably, NFJIs have been shown to improve immune responses to vaccines, offering a

promising avenue for enhanced efficacy in immunization programs [93]. Beyond fluids, NFJIs extend their use to the delivery of solid medications, broadening their applicability across various therapeutic domains [141]. Collectively, these benefits underscore the transformative potential of needle-free injection technology in revolutionizing drug delivery and patient care.

In general, NFJIs can be categorized based on the propulsion mechanism that injects the liquid into the human skin. The first category utilized a piston to propel the liquid inside the skin. The energy source that drives the piston can be either mechanical or electrical. Compressed springs or compressed gas are the most typical used among commercial needle-free injections [150] These mechanical NFJIs are noted for their simplicity, reliability, and cost-effectiveness, making them especially useful in settings with limited resources or where electrical power is scarce. However, they tend to offer less precise control over drug delivery, leading to potential variability in medication dispersion and depth. The electrical-based NFJIs employ actuators, which utilize the Lorentz force or the piezoelectric effect for piston actuation. These electrical NFJIs demonstrate enhanced precision in controlling penetration depth, medication dispersion, and minimizing splashback effects [156]. However, similar to their gas and spring-based counterparts, these injectors are primarily limited to delivering larger volumes (in excess of 100 mL) into deeper tissue strata. Jet injectors can be further categorized into multi-use nozzle jet injectors (MUNJIs) and disposable cartridge jet injectors (DCJIs). The World Health Organization has prohibited the use of MUNJIs for human applications, primarily due to the risk of cross-contamination with the hepatitis B virus [141] arising from the injector nozzle. This contamination risk is predominantly linked to the splash-back phenomenon associated with the liquid jet.

The second type of injector utilises optical energy from pulsed or continuous wave lasers to create a high-pressure vapor bubble, which in turn rapidly expands and propels the liquid out of the injector. This laser-induced method offers significant control over the jet velocity and penetration depth, enabling precise and targeted drug delivery. Enhanced control over injection depth has the potential to positively influence the pharmacokinetics of diverse therapeutic agents. For instance, when vaccines are administered into the epidermis, the dosage required can be reduced by five to ten times, thanks to the high concentration of specialized immune cells present in that skin layer [87, 98]. The absence of traditional mechanical or electrical components not only reduces the risk of mechanical failure but also streamlines the design of the device. Furthermore, ensuring consistent performance and preventing tissue damage demands precise control and calibration of the laser parameters, necessitating sophisticated operational protocols. Thus, as traditional NFJIs, have extensively been investigated in this paper, we simulate NFJIs where the formation of the jet results from the expansion of a bubble

induced by a laser.

The dynamics of jet formation in different types of NFJIs have been extensively studied in the past decades [87, 141, 156]. In most modern injectors, the jets are turbulent, characterized by Reynolds numbers in the tens of thousands. A turbulent jet features two distinct regions: the initial region, where the fluid maintains its exit velocity, and the main region, where the velocity diminishes as a result of jet expansion. Typical jet velocities reach speeds of $> 100 m/s$ to deliver drugs across the skin and into the subcutaneous or intramuscular region [13]. The collapse of a conical gas bubble at the end of a liquid-filled tube was investigated in the pioneering work of Leighton et. al [94] for NFJIs. In the context of laser-based micro injectors, it was shown in the work of Tagawa et. al [158] that jet velocities up to $850 m/s$ were achieved, for a small quantity of liquid in an open-filled capillary. Sierra et al. [56] studied the dynamics of the laser-induced bubbles and found average speeds of 10 to $25 m/s$ for the bubble wall for a number of different laser parameters, thus indicating that the bubble dynamics might be a limiting factor in the maximum speed of the jet. Furthermore, backflow might occur during skin penetration if the rate at which the hole is formed is slower than the volumetric flow rate of the jet liquid entering the skin [151]. This backflow from the hole impedes the momentum of the jet entering the hole and thus reduces its capacity to penetrate further into the skin.

Several studies have tried to elucidate the dynamics of the liquid-jet impact on skin or other skin-mimicking material. The effectiveness of drug delivery is significantly impacted by the mechanical characteristics of the skin. Factors such as Young's modulus, the critical stress threshold for failure, fracture toughness, hardness, and hydraulic conductivity are crucial in influencing the depth and success of jet penetration. Initial studies examined the penetration depth as a function of the skin's Young's modulus [110]. Baxter et al. [13] experimentally validated a theoretical model for penetration depth as a function of jet and skin properties. Later, Shergold et al. [154] examined the penetration of a soft solid by a liquid jet. They showed that the stagnation pressure of the fluid necessary for skin penetration diminishes as the diameter of the liquid jet increases. This observation aligns with the dynamics of slow-speed penetration of a soft solid by a sharp-tipped instrument and thus the Shergold–Fleck sharp-tipped punch penetration model provides accurate estimates for the pressure needed to penetrate a soft solid with a high-speed liquid jet. Chen et. al [26] derived a mathematical model to predict the penetration depth and the radius of the sphere at the injection depth. This study was based on a model for the penetration of a soft solid by a flat-bottomed cylindrical punch. Even though, the predicted results for penetration depth and dispersion radius exhibit a correlation that aligns with the experimental findings, discrepancies between the two exist.

Mohizin et. al [114] utilized high-speed imaging data to reveal that the fracture toughness of the medium affects the penetration mechanism of the injected microjet. Meanwhile, the viscoelastic and poroelastic properties of the medium dictate the ultimate injection profiles achieved. Even though several studies have tried to address the precise mechanism by which a jet interacts with skin, it is still not fully understood [168]. It is uncertain whether the jet erodes the skin or induces a crack to facilitate penetration. The present study was designed to elucidate the jet-skin interaction. Understanding the injected fluid–tissue interactions is critical for the development of efficient and safe NFJIs.

In addition to theoretical and experimental research, numerous numerical studies have also been conducted on this subject. Peters et. al [123] utilized a boundary integral model to simulate the formation of the liquid jet. In this work, a good agreement with experimental data is shown, and a simple analytical model able to predict jet velocity is presented. Kyriazis et. al [88] examined the jet formation leveraging a two-phase solver. Yet again the jet was laser-induced through the expansion of a vapor bubble. Good agreement with experimental data was shown, followed by parametric studies on the meniscus shape. Orimi et. al [118] presented a hybrid analytical/numerical model to simulate nanosecond laser-induced micro-jets with application in micro-drop printing. Rane et. al [138] investigated the role of fluid rheology and cartridge geometry in jet velocities, pressure drop, and boundary layer thickness, in mechanical injectors. They report that there might be optimal geometries for creating jets to target specific tissue depths. Mohizin et. al [112] further studied air-powered injectors of various geometrical characteristics. The findings of this study highlight a trade-off between the density and velocity of the microjet on the skin surface, which varies with the nozzle diameter. Finally, the work of Liu et. al [99] addresses the heat transfer from the liquid jet on the skin. A negligible effect between the two was found. Most prior research on needle-free jet injection systems has focused on the fluid dynamics of the propelled microjet, without taking into account the impact of the medium being injected on the penetration and dispersion of the microjet.

In this chapter, we aim to elucidate the liquid-jet interaction with skin-like materials in NFJIs. In the current simulations, and in the work of Kyriazis et al. [88] the minimum Weber number has been determined to be approximately We = 80, leading to the decision to disregard surface tension effects. Furthermore, the plasma phase from the laser pulse and the vapor generation are not taken into account as the validity of such a model would be hard to establish and are out of the scope of the present study. Two micro-jetting devices were examined. The first serves as a validation with other numerical and experimental data. The temporal evolution of cavity shape, penetration depth of liquid jet, and the stress field

developed is later investigated for the second microjetting device. In total 4 solid materials
are examined, with 3 corresponding to skin-like materials and a soft tissue one.

5.2 Results and Discussion

In this section, several numerical simulations of needle-free injections are presented, for 2
different microjetting devices and various initial conditions. The first micro-jetting device
presented here is utilised to provide comparisons with experimental and numerical studies.
The second micro-jetting injector has similar dimensions to the ones presented in the work
of Schoppink et. al [150]. Overall, results from 4 simulations are presented, elucidating the
jet-solid interaction for three different skin-like materials, and a soft tissue-like solid.

5.2.1 Micro jetting devices

The first micro-jetting device was initially presented in [60] and later used as a benchmark
in the numerical simulations of [88]. The configuration of the geometry is depicted in figure
35. As the laser and liquid vaporization is out of the scope of this study, we initially placed
a high-pressure gas bubble on the bottom left of the domain, surrounded by the liquid-to-
be-injected, in this case, water. The meniscus interface between the air and the liquid is
placed at a distance $S = 1.0mm$, and it has a hemispherical geometry. textcolorblackIn
contrast to the previous chapters, where the simulations were inviscid, here the fluids are
considered viscous. The parameters of the EoS and the viscosity for the gas are the following:
$\gamma = 1.4$, $\pi_\infty = 0.0\ GPa$ and $\mu_g = 1.515e - 5Pas$, while for the liquid (water) are: $\gamma = 4.4$,
$\pi_\infty = 0.6\ GPa\ \mu_g = 0.001Pas$. The high-pressure gas bubble is set at $37MPa$ [88], and the
rest of the domain is at atmospheric pressure and zero velocity.

A grid independence study was carried out to study the effect of the mesh on the jet velocity.
It was found that meshes consisting of ≈ 90.000 elements, result in satisfactory resolution of
the jet and the jet velocity. Similar findings were found in [88]. Thus in this study, we
employ an initial ancestral mesh containing ≈ 150.000 elements, with the 90.000 being in the
area of the injector. Due to the symmetrical nature of the geometry only an unstructured
hybrid wedge-type mesh of 2° degrees is employed. On the cut planes symmetry boundaries
conditions are applied. Additionally, 3 levels of refinement were used on the interfaces between
the fluid and the gas. Furthermore significant pressure gradients i.e. $\epsilon = 0.4$ (see eq. 34) were
tracked with 3 levels of refinement. The time step in the simulations was computed so that

Case #n	$p_{bb}[Pa]$	$\rho[m^3/kg]$	$R_{bb}[mm]$	$u_{jet}[m/s]$	Re
1	37	200	0.05	49.67	1173
2	37	100	0.05	48.56	1146
3	37	100	0.025	14.93	352
4	37	100	0.1	106.50	2515
5	20	54.05	0.05	33.42	789
6	50	135.13	0.05	52.48	1239
7	70	189.18	0.05	71.55	1689
8	100	270.27	0.05	87.69	2071

Table 3: Influence of bubble's initial conditions on liquid jet velocity.

CFL would not exceed 0.1 thus, ensuring numerical stability.

The assumption of symmetry greatly reduces the computational cost and enables a higher resolution on the fluid-gas interface dynamics, which otherwise would elude. Symmetry boundary conditions are assumed at the limiting planes while the outermost boundaries are modeled by outflow conditions. No-slip boundary conditions are applied on the wetted surface of the micro-jetting injector.
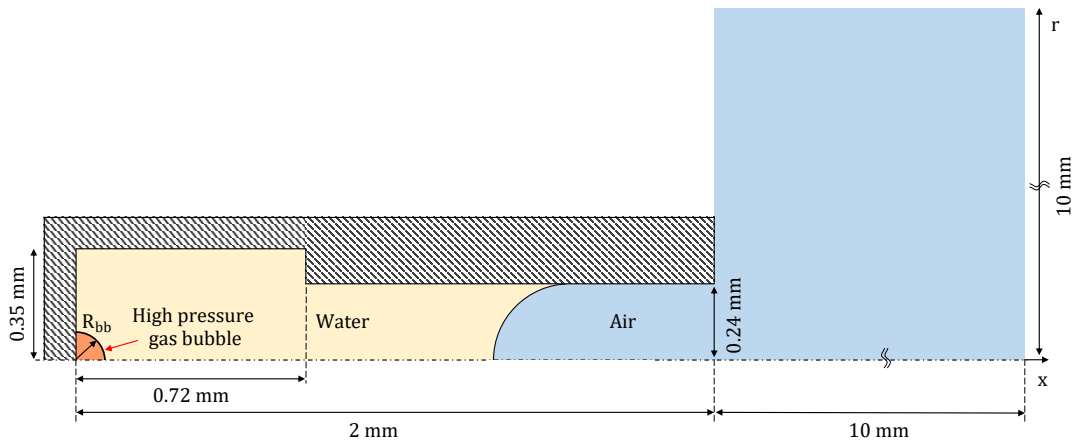
Figure 35: Configuration of the needle-free injector. On the right the high-pressure gas bubble, the liquid-gas interface with black. The axis of symmetry is denoted by the dashed line.

In Fig. 36, the pressure and velocity magnitude are depicted for 6 time steps, along the (x-z) and (x-y) planes respectively. The high-pressure bubble sets in motion the liquid around it as it expands radially. A shock wave is emitted which is reflected a number of times from the surrounding walls. The superposition of the reflections leads to even higher pressure regions as shown in Fig. 36. Eventually, the shock wave impacts the gas-liquid interface, initially at the center of the axis, as presented in Fig. 36 In later time steps the whole hemispherical interface is impacted by the high-pressure liquid, forming the axisymmetric microjet. The formation of the liquid jet starts at $t = 0.063\mu s$. As the interface collapses and the liquid

jet gains momentum, a long neck is created as seen in Fig. 36. The geometry of the nozzle further intensifies the focusing of the input energy and the acceleration of the flow.

As the liquid gets ejected from the needle-free injector, secondary regions of cavitation appear. The most prominent area is around the stenosis, which gives rise to higher liquid velocities, and lower pressures, and thus the gas phase expands. Following the initial appearance of this cavitation region, the gas content gets accented by the mean flow reaching downstream, as seen in Fig. 36h. The second area of cavitation is around the axis of symmetry. As the liquid jet is primarily developed around the axis of symmetry, the liquid between the bubble and the gas-liquid interface is accelerated. This rapid acceleration leads to lower pressures and gas pockets appear. These gas pockets around the axis of symmetry collapse and rebound, as the liquid is ejected outwards. Furthermore, high velocities are found at the exit of the tube, as the liquid displaces the air, as presented in Fig. 36e-h.

Inherently there has to be an assumption of the initial conditions of the high-pressure gas bubble, as the laser-liquid vaporization can not be simulated by the present model and is out of the scope of the present study. Following the work of Kyriazis et. al [88], we can equate the laser energy with the dynamic energy of the gas bubble. The dynamic gas bubble is equal to $E_{dyn} = \Delta pV$, where the pressure difference corresponds to the gas-liquid pressures and V is the volume of the bubble. A correcting parameter n was introduced by the same authors to account for the absorbed laser energy. In Table 3 the initial conditions and results are presented for a number of test cases. The initial conditions that need to be addressed are the pressure, density, and radius of the gas bubble. The Reynolds number is computed based on the jet velocity, the viscosity of the fluid and the radius of the liquid jet.

The velocity of the liquid jet is measured by the displacement of the gas-liquid interface at 4 distinct phases. At $s/L = -0.28, s/L = 0, s/L = 0.25, s/L = 0.45$, where s is the location of the jet in relation to the exit of the nozzle, and L the length of the injector. Additionally, the liquid jet velocity is further computed between these time steps by integrating and averaging the values of the elements in a cylinder around the interface. The difference between the two was less than 1% for all test cases. Case 1 and Case 2, are designed to address the influence of the initial density of the high-pressure gas bubble. A negligible difference in the jet speed was found between the two. In Case 2, Case 3, and 4 the effect of the initial volume of the gas bubble was investigated. As expected, larger high-pressure bubbles lead to higher jet velocities. Finally, the relation between pressure and density was examined in Cases 5 - 8. In Fig. 37 the liquid jet formation is presented for Cases 6-8. A linear relation was found, similar to the work of Kyriazis et. al [88]. Thus we can conclude that by adjusting the initial

(a) $t = 0.0\ \mu s$

(b) $t = 0.04\ \mu s$

(c) $t = 0.06\ \mu s$

(d) $t = 0.1\ \mu s$

(e) $t = 7.5\ \mu s$

(f) $t = 15\ \mu s$

(g) $t = 20\ \mu s$

(h) $t = 30\ \mu s$

Pressure [MPa]

Velocity Magnitude [m/s]

0.001 5.0 10.0 15.0 20.0 25.0 30.0 35.0 37.0

0   5   10   15   20   25   30   35   40   45   50
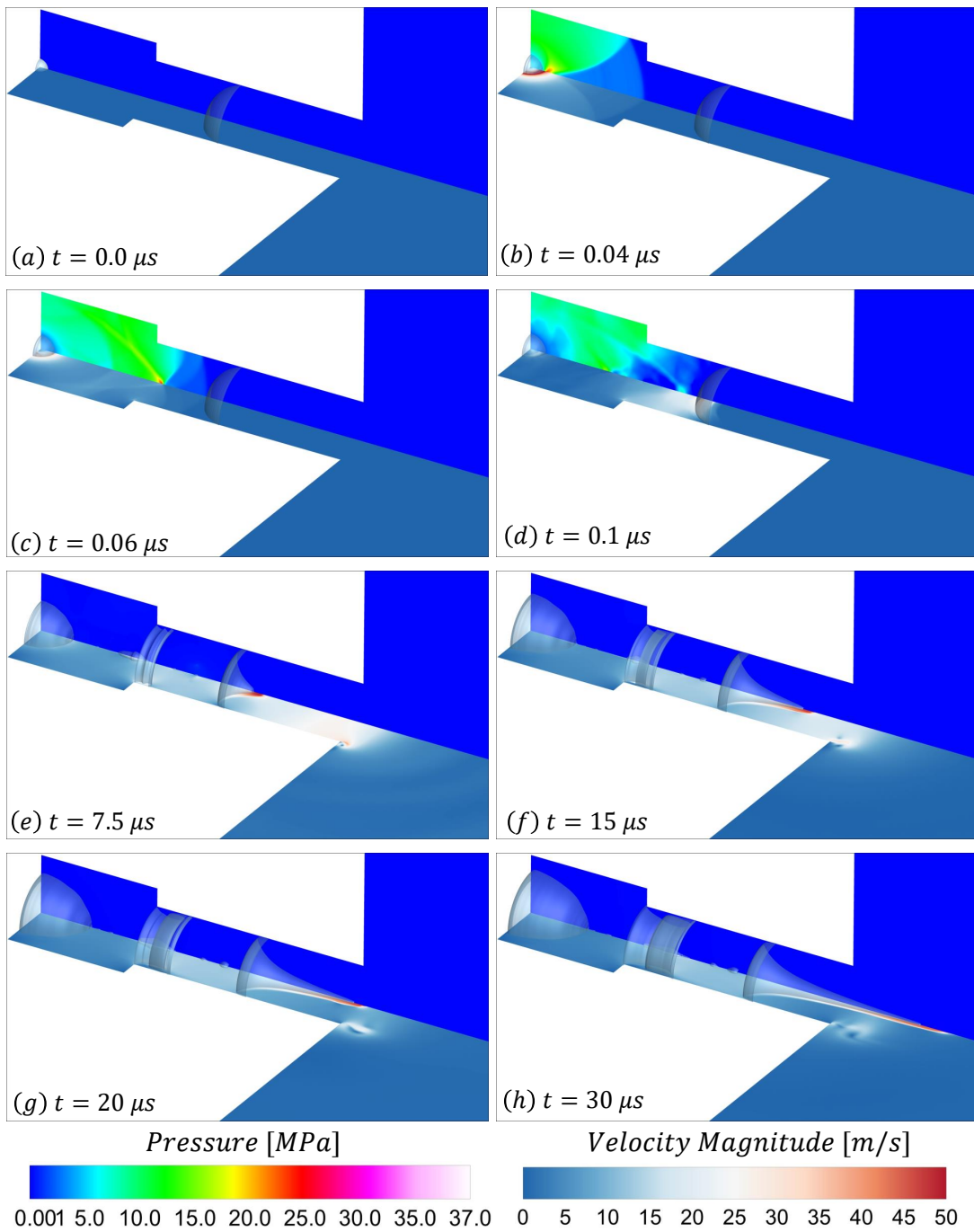
Figure 36: Needle-free injector simulation. Case 2. The pressure field on the x–y plane and velocity magnitude field on the x–z plane are shown. Isosurfaces of the gas phase for gas volume fraction $\alpha_{gas} = 0.5$

97

conditions of the problem we can closely match the liquid-jet velocities of experimental studies, such as those of Hayasaka et al. [60].

5.2.2   Liquid-jet - solid interaction

In this section, the liquid jet impact on the skin-like materials is presented. To this end, the micro-jetting device is introduced in figure 38. This device is similar to those used in [150]. The micro-injector has a length of $2mm$ and similar to the previous cases the high-pressure gas bubble is introduced into the domain tangentially to the wall. The meniscus interface between the air and the liquid is placed at a distance $S = 1mm$, and it has a hemispherical geometry. The solid interface is placed close to the exit of the injector, in an effort to minimize the computational cost of the simulations. Furthermore, the area around the injector (and opposite from the solid interface) was modeled, so as to capture any back-splash from the liquid-jet skin interaction.

The initial computational mesh has ≈ 200.000 elements to cover the whole of the domain. The same AMR strategy is followed with 3 levels of refinement used on the interfaces and significant pressure gradients. The total number of elements exceeds 1 million during the final time steps of the simulation. Symmetry boundary conditions are implemented at the limiting planes, and the outermost boundaries are treated with outflow conditions. On the wetted surface of the micro-jetting injector, no-slip boundary conditions are enforced.

The high-pressure gas bubble is set at $50MPa$, with an initial radius of $R_{bubble} = 0.05mm$. and the rest of the domain is at atmospheric pressure and zero velocity. These initial conditions lead to liquid jet velocities of $85m/s$, which is common for these types of injectors. The parameters of the EoS were given in the previous section for both water and gas. In general, the mechanical properties of skin vary depending on the measurement type, location on the body, age, and sex among other factors. Reported skin stiffness values range from $2kPa$ – $1GPa$ [111]. Furthermore, the intricate structure of layers of the skin poses a serious issue in numerical modeling. The mechanical properties of the sub-layer of the tissue, namely the epidermis, dermis, and hypodermis vary greatly [36]. In addition, the interface conditions between the layers further complicate the modeling aspect of the skin. Thus in the present study, we employ a bulk modeling of the skin as one solid material with varying mechanical properties. In total 3 types of skin-like material were used. Additionally, a soft-tissue material, with properties closely resembling gelatin is also considered to aid in future comparisons with numerical and experimental data and elucidate the differences in the material response between
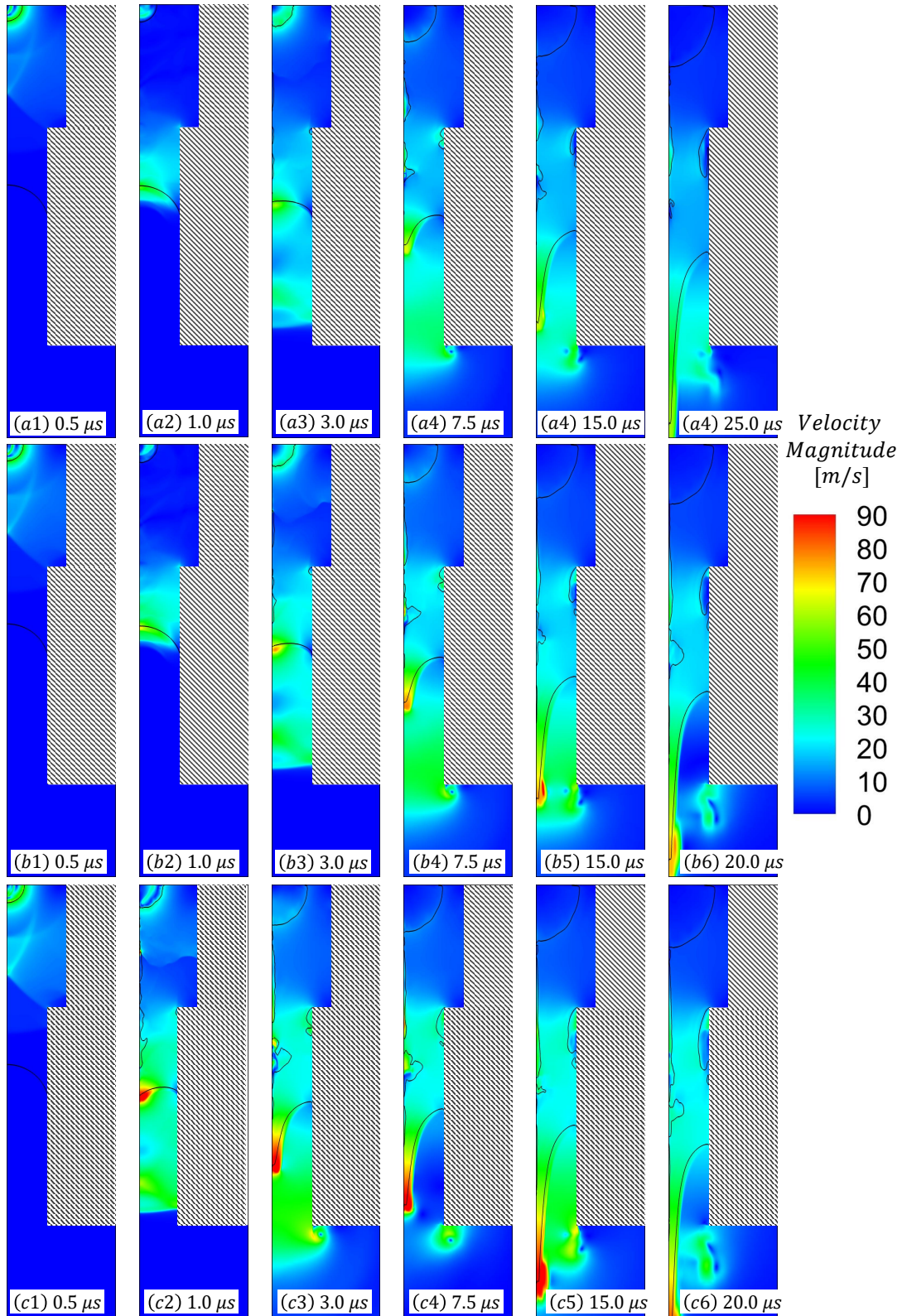
Figure 37: Needle-free injector simulations. Velocity magnitude contours are shown for Cases 6,7 and 8. Isosurfaces of the gas phase with black for vapor volume fraction $\alpha_{gas} = 0.5$
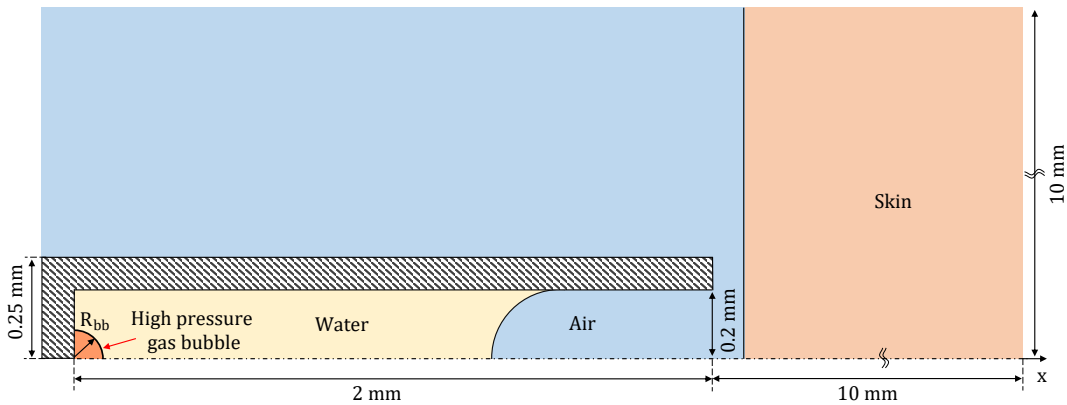
Figure 38: Configuration of the needle-free injector. On the right the high-pressure gas bubble, the liquid-gas interface with black. On the right, the skin-mimicking materials. The axis of symmetry is denoted by the dashed line.

Material	$\rho[m^3/kg]$	π_∞ GPa	γ	mu	$c(m/s)$
Skin type A	1109	0.697	4.2	6.5e3	1624
Skin type B	1109	0.697	4.2	6.4e4	1625
Skin type C	1109	0.697	4.2	3.5e4	1625
Gelatin	1060	0.59	4.3	1e3	1547

Table 4: Material properties of the skin-like materials and gelatin used in the numerical simulations.

soft and stiff solids. In Table 5.2.2 the parameters of the equation of state and the mechanical properties are presented.

In Fig. 39 the pressure and velocity magnitude contours are depicted in the x-z and x-y planes respectively. The liquid jet is presented as the iso-surface of the liquid volume fraction $a_{liquid} = 0.5$ The solid material tested in this Figure is gelatin. Parts of the computational domain are not depicted in the figure to avoid visual clutter and to highlight the liquid-jet-solid interaction. In particular, two regions of the domain are not visible; the area around the injector (see Fig. 39) and the region for $r > 0.5mm$.

Similarly to the previous cases, the rapid growth of the high-pressure gas bubble sets in motion the liquid jet. In Fig. 39a the initial shock wave has been reflected by the upper wall of the micro-injector, which will later impact the expanding bubble. Higher pressure regions are formed from the superposition of the reflected shock waves as seen in Fig. 39c. Following the impact of the shock wave on the hemispherical interface, the liquid jet is formed at $t = 0.078ms$. The rapid acceleration of the liquid jet leads to the creation of cavitation pockets around the axis of symmetry and between the expanding bubble and the collapsing hemispherical gas-liquid interface. The dynamic appearance of these gas pockets is evident in

Fig 39e-h.

The impact of the liquid jet on the gelatin surface is depicted in Fig. 39f-h. In the work of Edwards et. al [39] the critical jet velocity for skin penetration is estimated at $10m/s$. In the present test case, the liquid velocity is approximately $85m/s$, and thus the jet is strong enough to penetrate the gelatin and skin-mimicking materials A-C. Indeed in Fig. 39f the initial impact and crevise are depicted. As the liquid jet is decelerated from the elasticity of the gelatin, the tip of the jet expands radially. In later time-steps the liquid jet has further penetrated the gelatin, creating the characteristic neck, around the initial gas-solid interface, with a radially expanding inner area. The liquid trapped in this region expands and fills the cavity. This mechanism is also reported in experimental studies of needle-free injectors. Furthermore, the liquid jet induces high gas velocities around the exit of micro-injector as seen in Fig. Fig. 39f-h.

In Fig. 40 contours of the stress development during the liquid-jet-skin interaction for the three types of skin materials are presented. Similar to the previous figures x-z and x-y planes are used. The liquid jet is depicted through the iso-surface of the liquid phase. The principal stresses that lie on the x-y plane are computed as:

$$\sigma_{1,2} = (\tau_{xx} + \tau_{yy})/2.0 + \sqrt{\tau_{xy}^2 + (\tau_{xx} + \tau_{yy})^2/4} \qquad (45)$$

where τ_{ij} are the components of the stress tensor. The last principal stress is defined as $\sigma_3 = \tau_{zz}$. Thus we can define the maximum tensile stress as $S_{tens} = max(\sigma_1, \sigma_3)$ and the maximum compressive stress as $S_{comp} = -min(\sigma_2, \sigma_3)$. Finally, the maximum shear stress is:

$$T_{max} = (max(\sigma_i) - min(\sigma_i))/2 \qquad (46)$$

Thus, T_{max} is depicted on the vertical x-y plane and the maximum compressible stress S_{comp} is depicted on the horizontal (x-z) plane. Comparing the shear stresses at $t = 15\mu s$, in Fig 40a1,b1, and c1, it is evident that skin types B and C exhibit a high-stress concentration at the tip of the liquid jet and around the created crevice. Furthermore, the softer skin type A has been penetrated further and no neck around the entrance of the crevice has formed. The maximum compressive stress has a similar behavior, with skin type A exhibiting only a narrow area of high stress, whereas in the other two the region expands around the entire liquid-solid interface. At $t = 20\mu s$ the neck formation is apparent in the skin type A, as seen

(a) $t = 0.01\,\mu s$

(b) $t = 0.03\,\mu s$

(c) $t = 0.06\,\mu s$

(d) $t = 0.08\,\mu s$

(e) $t = 10\,\mu s$

(f) $t = 15\,\mu s$

(g) $t = 30\,\mu s$

(h) $t = 40\,\mu s$

Pressure [MPa]

Velocity Magnitude [m/s]
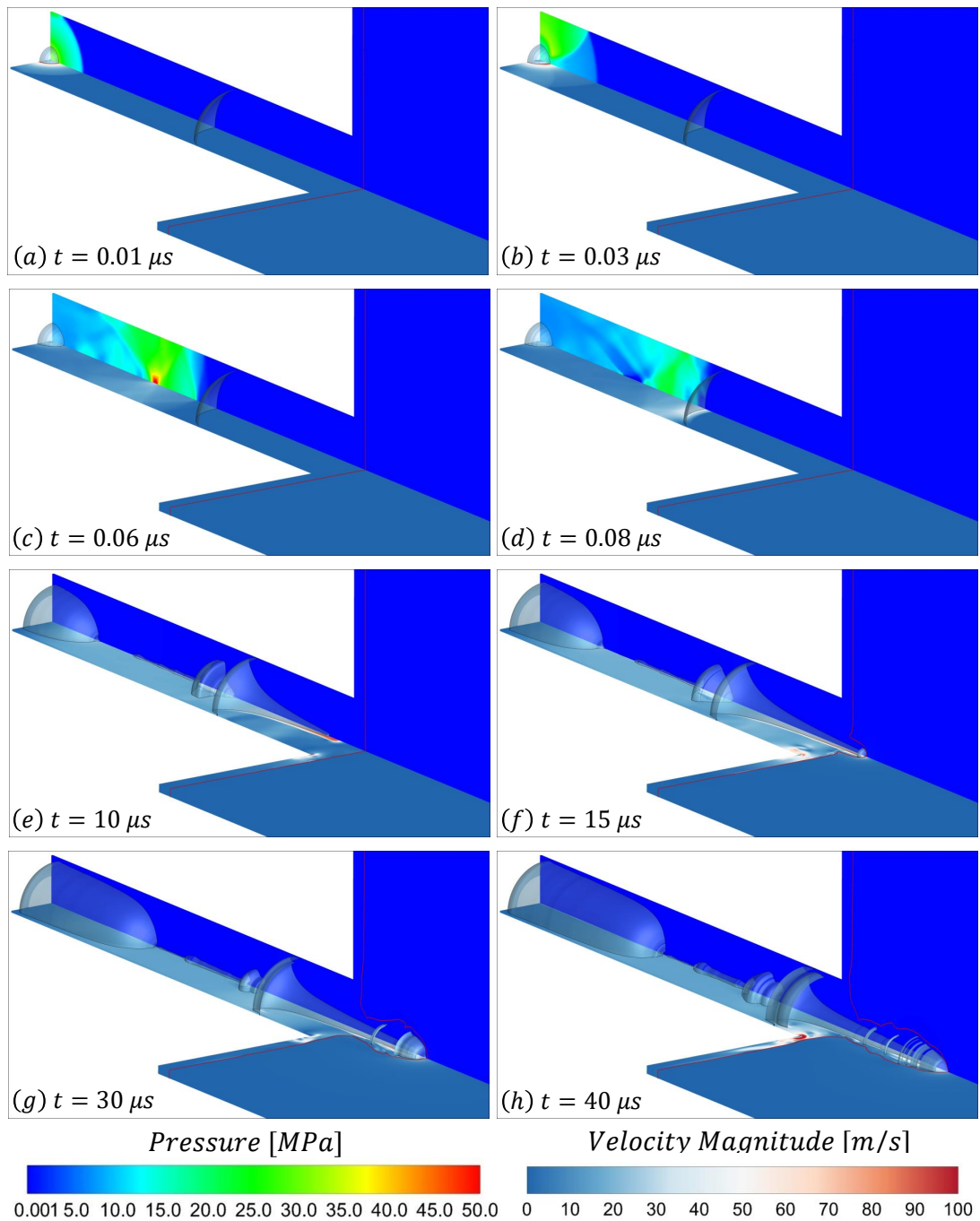
Figure 39: Needle-free injector simulation. The pressure field on the x–y plane and velocity magnitude field on the x–z plane are shown. Isosurfaces of the gas phase for gas volume fraction $\alpha_{gas} = 0.5$

102

Material	Penetration Depth [mm]	Crevice Radius [mm]
Gelatin	0.632	0.112
Skin type A	0.566	0.090
Skin type B	0.171	0.176
Skin type C	0.120	0.171

Table 5: Numerical results of the penetration depth and the crevice radius created by the impact of the liquid jet to the skin-like material and gelatin.

in Fig. 40a2. High shear forces are still highly localized around the tip of the jet. A small backflow of liquid is present, without however escaping outside of the crevice. Skin types B and C present high shear forces in a greater area around the tip of the liquid jet.

A notable difference, in the liquid jet characteristics, emerges between skin type A and skin types B and C. In the case of the former, the liquid jet remains confined around the axis of symmetry as seen in Fig. 40. For the two other skin types, due to the stiffer nature of these materials, the liquid jet expands radially, in a shorter penetration depth. It seems from these 4 solid materials that for softer skins the liquid jet will reach further inwards. Thus the cavity will be later formed and filled with the injected liquid. For stiffer solids, the penetration depth is shortened and the formation of the cavity is closer to the initial interface. This mechanism is seen in Fig. 40a5,b5, and c5. Furthermore, backflow of liquid is present in all skin types. For the stiffer skin types, the backflow is more prominent.

The penetration depth is an important metric in NFJIs. As depicted in Fig. 39 and Fig. 40, various penetration depths are achieved for the different solid materials. Furthermore, differences in the radius of the created spherical cavity are found among the cases. Thus the depth and radius of all the materials are summarized in Table 5.2.2. These values are measured at $t = 40\mu s$.

As expected the liquid jet penetrates the gelatin and skin type A further, as those have the lowest shear modulus. Finally comparing the stiffer skins B and C, we found a similar structure in the penetration mechanics and stress development.

5.3   Conclusions

In this work, we have performed a series of simulations of needle-free devices under various conditions. A unified Eulerian numerical framework introduced in 2 has been utilized for capturing the rapid growth of the laser-induced bubble, the secondary cavitation regions inside the liquid phase, and the fluid-structured interaction between the liquid-jet and the skin.

Skin Type A | Skin Type B | Skin Type C

$(a1)\ t = 15\ \mu s$ $(b1)\ t = 15\ \mu s$ $(c1)\ t = 15\ \mu s$

$(a2)\ t = 20\ \mu s$ $(b2)\ t = 20\ \mu s$ $(c2)\ t = 20\ \mu s$

$(a3)\ t = 25\ \mu s$ $(b3)\ t = 25\ \mu s$ $(c3)\ t = 25\ \mu s$

$(a4)\ t = 30\ \mu s$ $(b4)\ t = 30\ \mu s$ $(c4)\ t = 30\ \mu s$

$(a5)\ t = 35\ \mu s$ $(b5)\ t = 35\ \mu s$ $(c5)\ t = 35\ \mu s$

$T_{max}[MPa]$ $S_{comp}[MPa]$

0.001 0.05 0.10 0.15 0.20 0.25 0.30   0.001 0.10 0.20 0.30 0.40 0.50
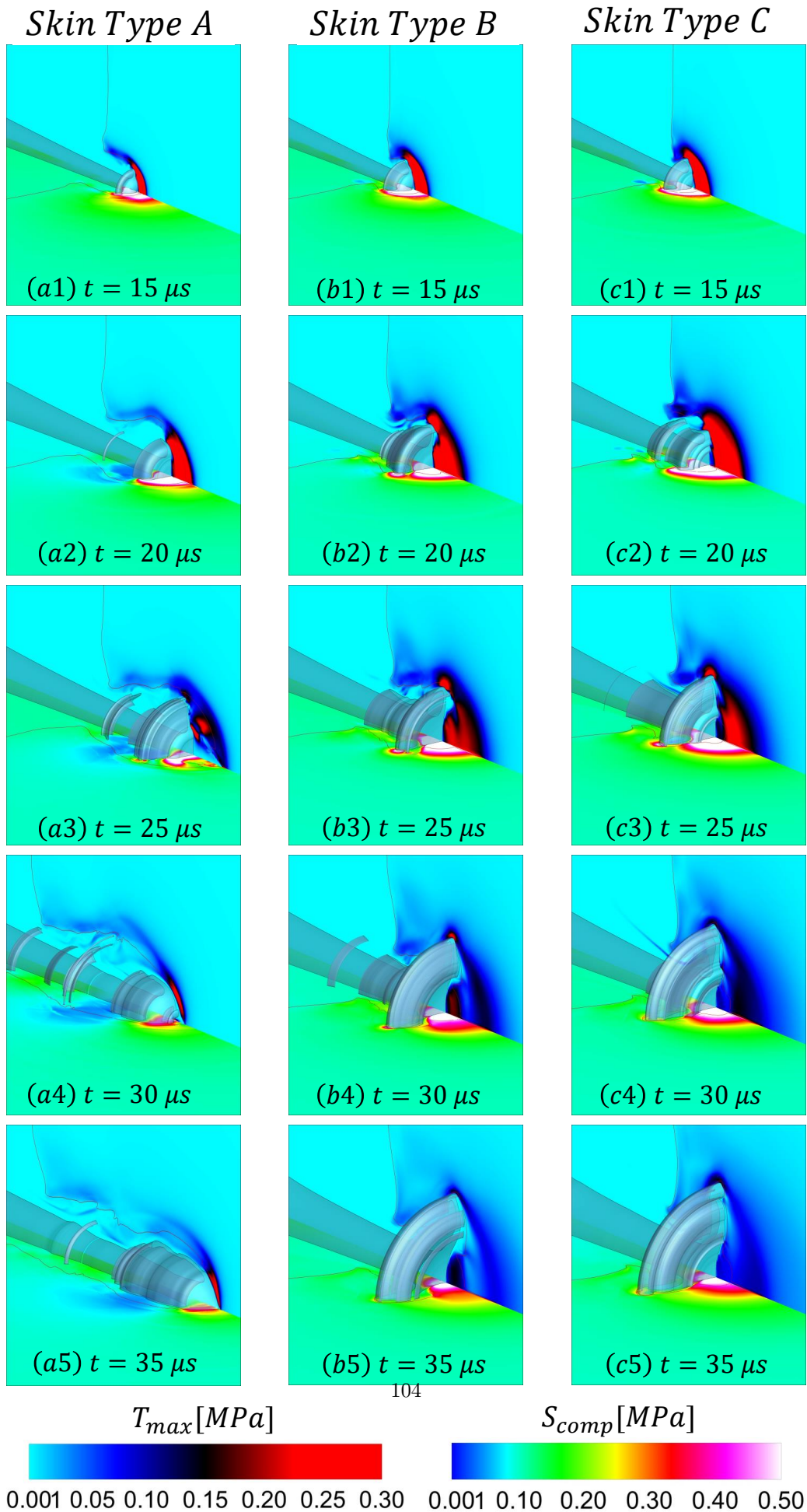
Figure 40: Needle-free injector simulation. The pressure field on the x–y plane and veloc-

In this study, the Diffuse Interface Model is expanded by the addition of viscosity. The validity of the results was assessed by comparing the liquid-jet velocity to other numerical and experimental work. To this end, various initial conditions were tested and the liquid jet velocity was measured. A close agreement was found between the presented numerical results and the experimental data. Furthermore, the liquid-jet skin interaction was investigated for 4 different solid materials. A similar structure to the pore formation between the numerical simulation and experimental data was observed [113]. A long neck leading to a cavity filled with liquid to be injected. Higher stress concentration was found for stiffer skin types, with shorter penetration depths and smaller cavities. Backflow of liquid was present in all cases. These results are an initial investigation into the development of a numerical tool able to predict penetration depth and cavity formation for various skin types. This can further our understanding of the intricate interplay between the liquid-jet formation and skin interaction and lead to more effective drug delivery systems.

6   Conclusions and recommendations for future work

6.1   Summary and Conclusions

In the present thesis, a novel numerical framework has successfully been developed for the study of bubble-tissue interactions. The 6-equation diffuse interface model [44] was implemented for general 3-dimensional unstructured grids, coupled with its extension for isotropic elastic solids. This model was incorporated into an Adaptive Mesh Refinement (AMR) framework for unstructured grids utilizing a dynamically evolving Oct-tree graph. This approach enables the on-the-fly refinement of the grid to self-similar cells at an arbitrary level of resolution. This novel approach not only addresses the challenge of simulating multiscale interactions but also optimizes computational efficiency by focusing on regions of critical interest. The presented framework was validated against theoretical, experimental, and numerical results from the literature.

The developed numerical framework was first utilised to study the shock-induced bubble dynamics close to soft and rigid bio-materials, namely soft tissues and kidney stones. This study unveiled a new mechanism of tension-driven tissue damage involving both attached and detached gas bubbles during shock wave lithotripsy. This understanding of how tissue penetration and tension-driven injuries occur offers significant insights into the processes behind hemorrhage and tissue damage in shock wave lithotripsy and may help in providing guidelines on the procedures involving the use of ultrasound.

Furthermore, a comprehensive parametric study on the effects of various parameters on bubble collapse near bio-materials was conducted. By examining the influence of stand-off distance, initial bubble size, and the characteristics of the lithotripter's pulse, this study advances our knowledge of bubble dynamics. The findings from this parametric study contribute to a deeper understanding of the behavior and effects of shock-induced bubble collapse, offering valuable guidelines for the safe and effective application of cavitation in medical treatments.

Lastly, simulations of needle-free jet injectors were conducted to elucidate the interactions between the liquid jet and the skin. Validation cases were presented, and the process of liquid-jet formation was detailed. Subsequently, various skin-like materials were analysed. To the best of the author's knowledge the computational approach presented in this thesis and its applications to the simulation of cavitation induce jetting and liquid-jet interaction has not been previously reported in the literature.

6.2   Recommendations for future work

The developed numerical framework can be leveraged to study a vast array of other challenging multiphase phenomena in both bubble tissue interactions and engineering applications. Bubble clouds close to kidney stones could be investigated to examine the shock waves and bubble-bubble interaction in a more realistic scenario. The inertial collapse inside blood vessels and small capillaries can be investigated to examine the potential for hemorrhage. Ultrasound-induced stable cavitation of gas bubbles can be investigated to elucidate the mechanical effect of oscillation on membranes and tissues. Furthermore, drug delivery through the inertial collapse of encapsulated bubbles can shed light on both the dynamics of drug delivery and the role of the outer layer in the collapse dynamics. In engineering applications, an example of application of the presented framework may be the detailed investigation of internal combustion fluid injectors to study the formation of cavitation and other various flow characteristics.

From the numerical aspect, several improvements can be made to expand the use of the developed framework. In total 5 different physical models are currently implemented, the classical Euler equations, the Navier-Stokes, the 5-equation model, a two-fluid model with barotropic EoS, and the 6-equation model with the extension with fluid-structure interactions. The *DIM* model can further be extended to account for surface tension, mass/heat transfer, and plasticity. High-order reconstruction schemes such as *WENO* and interface reconstruction schemes like (Tangent of Hyperbola for INterface Capturing) *THINC* are planned for their future use to further preserve material interface and flow structures. Additionally, the numerical framework's computational efficiency and scalability, memory management, and overall data architecture warrant further exploration. A GPU implementation of ForestFV, a finite volume formulation with explicit time stepping, is a prime candidate for future development as it would results in massive parallel throughput and thus enabling the massively parallel simulations encompassing up to hundreds of millions cells. Such simulations could fundamentally transform the scope of problems addressed and broaden the application of the numerical framework.

7 Dissemination

Peer-Reviewed Journal Publications (newest first):

- E. Koukas, A. Papoutsakis, M. Gavaises, *Numerical investigation of shock-induced bubble collapse dynamics and fluid-solid interactions during shock-wave lithotripsy*, Ultrasonic sonochemistry, 10.1016/ j.ultsonch.2023.106393

- E. Koukas, A. Papoutsakis, M. Gavaises, *A parametric study on the effects of shock-induced bubble collapse dynamics on bio-materials during shock wave lithotripsy*, Ultrasonic sonochemistry, currently under review.

- E. Koukas, A. Papoutsakis, M. Gavaises, *Numerical investigation on bubble-induced jetting and fluid-solid interactions during needle-free injections*, currently under completion.

Conference Proceedings (newest first):

- E. Koukas, A. Papoutsakis, M. Gavaises, *Numerical investigation on cavitation-induced tissue injury during therapeutic ultrasound.* 7th IICR 15-16, June 2023

- E. Koukas, A. Papoutsakis, M. Gavaises, *Numerical investigation on cavitation-induced tissue injury during therapeutic ultrasound.* 76th APS 19-21, November 2023.

Appendix A

Details of numerical implementation

Starting from equation (14) the flux vector F and non-conservative terms H can be written in the following form:

$$\frac{\partial U_i}{\partial t} + \frac{\partial F_{ij}}{\partial x_j} + H_{ikl}\frac{\partial u_l}{\partial x_k} = 0, \quad i = 1,...,3 \cdot N_{mat} + 12$$

$$\frac{\partial U_i}{\partial t} + \frac{\partial F_{i1}}{\partial x} + \frac{\partial F_{i2}}{\partial y} + \frac{\partial F_{i3}}{\partial z} + H_{i1l}\frac{\partial u_l}{\partial x} + H_{i2l}\frac{\partial u_l}{\partial y} + H_{i3l}\frac{\partial u_l}{\partial z} = 0$$

$$(47)$$

where F_{i1}, F_{i2}, F_{i3} and $H_{i1l}, H_{i2l}, H_{i3l}$ are components of the F and H vectors for the flux and the non-conservative terms respectively. The complete set of the state vector U, the flux vector F, and the H non-conservative terms are presented below in a matrix form.

$$
U =
\begin{bmatrix}
\alpha_1 \rho_1 \\
\alpha_2 \rho_2 \\
\rho u_1 \\
\rho u_2 \\
\rho u_3 \\
\rho E \\
\alpha_1 \\
\alpha_1 \rho_1 e_1 \\
\alpha_2 \rho_2 e_2 \\
A_1 \\
A_2 \\
A_3 \\
B_1 \\
B_2 \\
B_3 \\
C_1 \\
C_2 \\
C_3
\end{bmatrix},
$$

$$(48)$$

$$
F_{1,2,3} =
\begin{bmatrix}
\alpha_1 \rho_1 u_1 \\
\alpha_2 \rho_2 u_1 \\
\rho u_1^2 + S_{11} \\
\rho u_1 u_2 + S_{12} \\
\rho u_1 u_3 + S_{13} \\
\rho E u_1 + S_{1i} u_i \\
\alpha_1 u_1 \\
\alpha_1 \rho_1 e_1 u_1 \\
\alpha_2 \rho_2 e_2 u_1 \\
A_1 u_1 \\
A_2 u_1 \\
A_3 u_1 \\
B_1 u_1 \\
B_2 u_1 \\
B_3 u_1 \\
C_1 u_1 \\
C_2 u_1 \\
C_3 u_1
\end{bmatrix},
\begin{bmatrix}
\alpha_1 \rho_1 u_2 \\
\alpha_2 \rho_2 u_2 \\
\rho u_2 u_1 + S_{21} \\
\rho u_2^2 + S_{22} \\
\rho u_2 u_3 + S_{23} \\
\rho E u_2 + S_{2i} u_i \\
\alpha_1 u_2 \\
\alpha_1 \rho_1 e_1 u_2 \\
\alpha_2 \rho_2 e_2 u_2 \\
A_1 u_2 \\
A_2 u_2 \\
A_3 u_2 \\
B_1 u_2 \\
B_2 u_2 \\
B_3 u_2 \\
C_1 u_2 \\
C_2 u_2 \\
C_3 u_2
\end{bmatrix},
\begin{bmatrix}
\alpha_1 \rho_1 u_3 \\
\alpha_2 \rho_2 u_3 \\
\rho u_3 u_1 + S_{31} \\
\rho u_3 u_2 + S32 \\
\rho u_3^2 + \sigma_{33} \\
\rho E u_3 + S_{3i} u_i \\
\alpha_1 u_3 \\
\alpha_1 \rho_1 e_1 u_3 \\
\alpha_2 \rho_2 e_2 u_3 \\
A_1 u_3 \\
A_2 u_3 \\
A_3 u_3 \\
B_1 u_3 \\
B_2 u_3 \\
B_3 u_3 \\
C_1 u_3 \\
C_2 u_3 \\
C_3 u_3
\end{bmatrix}
$$

110

$$H_1 = \begin{bmatrix} 0 & 0 & 0 \\ 0 & 0 & 0 \\ 0 & 0 & 0 \\ 0 & 0 & 0 \\ 0 & 0 & 0 \\ 0 & 0 & 0 \\ -\alpha_1 & 0 & 0 \\ \alpha_1\sigma_{11} & \alpha_1\sigma_{12} & \alpha_1\sigma_{13} \\ \alpha_2\sigma_{11} & \alpha_2\sigma_{12} & \alpha_2\sigma_{13} \\ 0 & -B1 & -C1 \\ 0 & -B2 & -C2 \\ 0 & -B3 & -C3 \\ B1 & 0 & 0 \\ B2 & 0 & 0 \\ B3 & 0 & 0 \\ C1 & 0 & 0 \\ C2 & 0 & 0 \\ C3 & 0 & 0 \end{bmatrix}, H_2 = \begin{bmatrix} 0 & 0 & 0 \\ 0 & 0 & 0 \\ 0 & 0 & 0 \\ 0 & 0 & 0 \\ 0 & 0 & 0 \\ 0 & 0 & 0 \\ 0 & -\alpha_1 & 0 \\ \alpha_1\sigma_{21} & \alpha_1\sigma_{22} & \alpha_1\sigma_{23} \\ \alpha_2\sigma_{21} & \alpha_2\sigma_{22} & \alpha_2\sigma_{23} \\ 0 & A1 & 0 \\ 0 & A2 & 0 \\ 0 & A3 & 0 \\ -A1 & 0 & -C1 \\ -A2 & 0 & -C2 \\ -A3 & 0 & -C3 \\ 0 & C1 & 0 \\ 0 & C2 & 0 \\ 0 & C3 & 0 \end{bmatrix}, H_3 = \begin{bmatrix} 0 & 0 & 0 \\ 0 & 0 & 0 \\ 0 & 0 & 0 \\ 0 & 0 & 0 \\ 0 & 0 & 0 \\ 0 & 0 & 0 \\ 0 & 0 & -\alpha_1 \\ \alpha_1\sigma_{31} & \alpha_1\sigma_{32} & \alpha_1\sigma_{33} \\ \alpha_2\sigma_{31} & \alpha_2\sigma_{32} & \alpha_2\sigma_{33} \\ 0 & 0 & A1 \\ 0 & 0 & A2 \\ 0 & 0 & A3 \\ 0 & 0 & B1 \\ 0 & 0 & B2 \\ 0 & 0 & B3 \\ -A1 & -B1 & 0 \\ -A2 & -B2 & 0 \\ -A3 & -B3 & 0 \end{bmatrix}$$

$$\tag{49}$$

Appendix B

Details of code implementation

This section details the numerical implementation and algorithm used to solve compressible multi-phase flows in ForestFV. The code is developed in the C programming language and employs the Message Passing Interface (MPI) for parallelization. ForestFV is specifically designed to explicitly solve hyperbolic systems of equations with additional source terms, utilizing the finite volume method.

Main key features of ForestFV:

- Support for structures and unstructured grids.

- Adaptive mesh refinement, with on the fly-splitting and merging of cells.

- Preserves the mesh quality metrics, up to any level of refinement.

- Second order reconstruction schemes.

- The following numerical models have been implemented:

  – Euler / Navier-stokes solver with the HLLC Riemann solver.

  – Single and multiphase barotropic models [89].

  – The 5-equation model of Kapilla [149].

  – The 6-equation model of Saurel et al. [148].

  – The extension to elastic solids of Favrie et al. [44].

ForestFV is designed for user-friendly operation, requiring only a single input file to define all parameters for a simulation. The domain initialization can be accomplished in three distinct ways: via the input file, using an STL file to define material volumes, or directly through the code by specifying initialization within the *initdomain.c* function. Currently, only the neutral format of *GAMBIT* is supported; however, many open-source and proprietary programs can generate these files. Boundary conditions can be specified either during mesh generation or overridden through a user-defined function.

ForestFV supports exporting data in both ASCII (.dat) and binary (.plt) formats for *Tecplot*, utilizing parallel I/O with *MPI* and the *TecIO-MPI* library. Additionally, field data can be post-processed with *Paraview*. The framework allows for the generation of restart files without limitation on the number of processors used for the simulation. There are two options for restart files: a single restart file, optimal for small cases, or a restart directory that creates a number of files equal to the number of processors used. These restart directories can be further processed by the ForestFVExport utility for creating field data, enhancing the efficiency of large simulations by offloading the creation of field data from the main code.

The main data structure of ForestFV is based on linked list of structs and the use of global variables. A struct is a collection of variables of various types, which are grouped and can be accessed by a single pointer.

The main structs used in ForestFV are the following:

- RUN: Contains all the information for the simulation.

- FOREST: Main struct with topology of the mesh and buffer elements (TREE & BRANCH).

- TREE: Contains information of the ancestral mesh.

- BRANCH: Contains the connectivity information, pointers to the CELL and to the LEAF and sub-Branches.

- LEAF: Contains the state vector the reconstructed variables on the faces and the gradients.

- CELL: Contains geometric information about the cell. (Area,vectors,volume,nodes,faces)

- SOL: Struct that facilitates the solution of the Riemann problems. It contains either the left (L) or the right (R) state.

The ForestFV can be summarized in the following pseudo-algorithm:

1. Input Read: input and mesh files

2. Mesh partitioning: Creation of local linked lists in each partition.

3. Memory allocation for state vectors (leafs) and utilities.

4. Computation of mesh properties: Volume, area, vectors.

5. Initialization of domain.

6. Geometric adaptation of domain: H-type refinement of interfaces before the start of the simulation.

7. — Non-blocking send of state vector S for buffer cells. (A)

8. –TIME LOOP–

    (a) Runge-Kutta steps: Runge-Kutta initialization

        i. Reconstruction/gradient for inner cells of each partition.

        ii. — Non-blocking receive of state vector. (A)/(B)

        iii. Reconstruction/gradient for outer cells of each partition.

        iv. — Non-blocking send of face values SF for buffer cells. (I)

        v. RHS computation for inner cells of each partition Eq. 15.

        vi. — Non-blocking receive of face values SF. (I)

        vii. RHS computation for outer cells of each partition Eq. 15.

        viii. Runge-Kutta step.

        ix. Relaxation procedure.

        x. — Non-blocking send of state vector S for buffer cells. (B)

(b) Export field.

(c) Adaptive mesh refinement.

    i. Criterion computation.

    ii. Criterion smoothing for (1:2) connectivity.

    iii. Refinement

    iv. Restructure topology for optimal load-balance.

    v. Mesh properties calculation.

    vi. — Blocking communication of state vector S for buffer cells.

9. De-allocate memory.

10. End of simulation.

References

[1] "A quantitative comparison of phase-averaged models for bubbly, cavitating flows". In: *International Journal of Multiphase Flow* 115 (2019), pp. 137–143. ISSN: 03019322. DOI: 10.1016/j.ijmultiphaseflow.2019.03.028. URL: https://doi.org/10.1016/j.ijmultiphaseflow.2019.03.028.

[2] Rémi Abgrall and Smadar Karni. "Computations of Compressible Multifluids". In: *Journal of Computational Physics* 169 (2 May 2001), pp. 594–623. ISSN: 00219991. DOI: 10.1006/jcph.2000.6685.

[3] Upendra Adhikari, Ardeshir Goliaei, and Max L Berkowitz. "Nanobubbles, cavitation, shock waves and traumatic brain injury". In: *Physical Chemistry Chemical Physics* 18.48 (2016), pp. 32638–32652.

[4] Alexander A. Aganin and Ildar N. Mustafin. "Cavitation bubble collapse and rebound in water: Influence of phase transitions". In: *International Journal of Multiphase Flow* 157 (2022), p. 104256. ISSN: 0301-9322. DOI: https://doi.org/10.1016/j.ijmultiphaseflow.2022.104256. URL: https://www.sciencedirect.com/science/article/pii/S0301932222002294.

[5] Kenneth B Bader and Christy K Holland. "Gauging the likelihood of stable cavitation from ultrasound contrast agents". In: *Physics in Medicine & Biology* 58.1 (2012), p. 127.

[6] Kenneth B. Bader, Eli Vlaisavljevich, and Adam D. Maxwell. "For Whom the Bubble Grows: Physical Principles of Bubble Nucleation and Dynamics in Histotripsy Ultrasound Therapy". In: *Ultrasound in Medicine and Biology* 45.5 (2019), pp. 1056–1080. ISSN: 1879291X. DOI: 10.1016/j.ultrasmedbio.2018.10.035.

[7] Melvin R Baer and Jace W Nunziato. "A two-phase mixture theory for the deflagration-to-detonation transition (DDT) in reactive granular materials". In: *International journal of multiphase flow* 12.6 (1986), pp. 861–889.

[8] Michael R Bailey et al. "Cavitation detection during shock-wave lithotripsy". In: *Ultrasound in medicine & biology* 31.9 (2005), pp. 1245–1256.

[9] Michael R Bailey et al. "Cavitation in shock wave lithotripsy". In: *Journal of the Acoustical Society of America* 114.4 (2003), pp. 2417–2417.

[10] Michael R Bailey et al. "Comparison of electrohydraulic lithotripters with rigid and pressure-release ellipsoidal reflectors. I. Acoustic fields". In: (1998). URL: http://acousticalsociety.org/content/terms..

[11]   Christopher W Barney et al. "Cavitation in soft matter". In: *Proceedings of the National Academy of Sciences* 117.17 (2020), pp. 9157–9165.

[12]   Daniel Barolet and Antranik Benohanian. "Current trends in needle-free jet injection: an update". In: *Clinical, cosmetic and investigational dermatology* (2018), pp. 231–238.

[13]   Joy Baxter and Samir Mitragotri. "Jet-induced skin puncture and its impact on needle-free jet injections: Experimental studies and a predictive model". In: *Journal of Controlled Release* 106 (3 Sept. 2005), pp. 361–373. ISSN: 01683659. DOI: 10.1016/j.jconrel.2005.05.023.

[14]   Nikolaos Bempedelis and Yiannis Ventikos. "A simplified approach for simulations of multidimensional compressible multicomponent flows: The grid-aligned ghost fluid method". In: *Journal of Computational Physics* 405 (Mar. 2020). ISSN: 10902716. DOI: 10.1016/j.jcp.2019.109129.

[15]   Saeed Bidi et al. "Numerical study of real gas effects during bubble collapse using a disequilibrium multiphase model". In: *Ultrasonics Sonochemistry* 90 (2022), p. 106175. ISSN: 1350-4177. DOI: https://doi.org/10.1016/j.ultsonch.2022.106175. URL: https://www.sciencedirect.com/science/article/pii/S1350417722002711.

[16]   A. Biesheuvel and L. Van Wijngaarden. "Two-phase flow equations for a dilute dispersion of gas bubbles in liquid". In: *Journal of Fluid Mechanics* 148 (1984), pp. 301–318. DOI: 10.1017/S0022112084002366.

[17]   Andreas Blana et al. "First Analysis of the Long-Term Results with Transrectal HIFU in Patients with Localised Prostate Cancer". In: *European Urology* 53.6 (2008), pp. 1194–1203. ISSN: 0302-2838. DOI: https://doi.org/10.1016/j.eururo.2007.10.062. URL: https://www.sciencedirect.com/science/article/pii/S0302283807013814.

[18]   Ayache Bouakaz, Aya Zeghimi, and Alexander A Doinikov. "Sonoporation: Concept and mechanisms". In: *Therapeutic Ultrasound* (2016), pp. 175–189.

[19]   Ayache Bouakaz, Aya Zeghimi, and Alexander A. Doinikov. "Sonoporation: Concept and mechanisms". In: *Advances in Experimental Medicine and Biology* 880 (Jan. 2016), pp. 175–189. ISSN: 22148019. DOI: 10.1007/978-3-319-22536-4_10.

[20]   N. K. Bourne and J. E. Field. "Shock-induced collapse of single cavities in liquids". In: *Journal of Fluid Mechanics* 244 (1992), pp. 225–240. ISSN: 14697645. DOI: 10.1017/S0022112092003045.

[21]   L. M. Brekhovskikh and O. A. Godin. "Acoustics of Layered Media I: Plane and Quasi-PlaneWaves vol. 5". In: *Springer Science & Business Media* (2012).

[22] Christopher Earls Brennen. "Cavitation in medicine". In: *Interface Focus* 5 (5 Oct. 2015), pp. 1–12. ISSN: 20428901. DOI: 10.1098/rsfs.2015.0022.

[23] Federico Bruno et al. "An experience-based review of HIFU in functional interventional neuroradiology: transcranial MRgFUS thalamotomy for treatment of tremor". In: *La radiologia medica* 125 (Apr. 2020), pp. 1–10. DOI: 10.1007/s11547-020-01186-y.

[24] Spencer H Bryngelson et al. "MFC: An open-source high-order multi-component, multiphase, and multi-scale compressible flow solver". In: *Computer Physics Communications* 266 (2021), p. 107396. DOI: 10.17632/8y55zscjd3.1. URL: http://dx.doi.org/10.17632/8y55zscjd3.1.

[25] S. Cao et al. "Shock-induced bubble collapse near solid materials: Effect of acoustic impedance". In: *Journal of Fluid Mechanics* 907 (2020). ISSN: 14697645. DOI: 10.1017/jfm.2020.810.

[26] Alvin I. Chen et al. "Multilayered tissue mimicking skin and vessel phantoms with tunable mechanical, optical, and acoustic properties". In: *Medical Physics* 43 (6 June 2016), pp. 3117–3131. ISSN: 24734209. DOI: 10.1118/1.4951729.

[27] Hong Chen et al. "Blood vessel rupture by cavitation". In: *Urological research* 38 (2010), pp. 321–326.

[28] Alexandre Chiapolino, Richard Saurel, and Boniface Nkonga. "Sharpening diffuse interfaces with compressible fluids on unstructured meshes". In: *Journal of Computational Physics* 340 (July 2017), pp. 389–417. ISSN: 10902716. DOI: 10.1016/j.jcp.2017.03.042.

[29] Charles C Church. "A theoretical study of cavitation generated by an extracorporeal shock wave lithotripter". In: *The Journal of the Acoustical Society of America* 86.1 (1989), pp. 215–227.

[30] "Cinematographic observation of the collapse and rebound of a laser-produced cavitation bubble near a wall". In: *Journal of Fluid Mechanics* 479 (Mar. 2003), pp. 327–348. ISSN: 00221120. DOI: 10.1017/S0022112002003695.

[31] Robin O. Cleveland and Oleg A. Sapozhnikov. "Modeling elastic wave propagation in kidney stones with application to shock wave lithotripsy". In: *The Journal of the Acoustical Society of America* 118 (4 Oct. 2005), pp. 2667–2676. ISSN: 0001-4966. DOI: 10.1121/1.2032187.

[32] Kerry W. Commander and Andrea Prosperetti. "Linear pressure waves in bubbly liquids: Comparison between theory and experiments". In: *The Journal of the Acoustical Society of America* 85.2 (1989), pp. 732–746. DOI: `10.1121/1.397599`. eprint: `https://doi.org/10.1121/1.397599`. URL: `https://doi.org/10.1121/1.397599`.

[33] Vedran Coralic and Tim Colonius. "Shock-induced collapse of a bubble inside a deformable vessel". In: *European Journal of Mechanics, B/Fluids* 40 (July 2013), pp. 64–74. ISSN: 09977546. DOI: `10.1016/j.euromechflu.2013.01.003`.

[34] Dr ¿C. C. Coussios et al. "Role of acoustic cavitation in the delivery and monitoring of cancer treatment by high-intensity focused ultrasound (HIFU)". In: *International Journal of Hyperthermia* 23.2 (2007), pp. 105–120. DOI: `10.1080/02656730701194131`.

[35] Gary C. Curhan. "Epidemiology of Stone Disease". In: *Urologic Clinics of North America* 34 (3 Aug. 2007), pp. 287–293. ISSN: 00940143. DOI: `10.1016/j.ucl.2007.04.003`.

[36] A. K. Dabrowska et al. "Materials used to simulate physical properties of human skin". In: *Skin Research and Technology* 22 (1 Feb. 2016), pp. 3–14. ISSN: 16000846. DOI: `10.1111/srt.12235`.

[37] Benjamin Dollet, Philippe Marmottant, and Valeria Garbin. "Bubble dynamics in soft and biological matter". In: *Annual Review of Fluid Mechanics* 51.September 2018 (2019), pp. 331–355. ISSN: 00664189. DOI: `10.1146/annurev-fluid-010518-040352`.

[38] Matevž Dular, Bernd Stoffel, and Brane Širok. "Development of a cavitation erosion model". In: *Wear* 261 (5-6 Sept. 2006), pp. 642–655. ISSN: 00431648. DOI: `10.1016/j.wear.2006.01.020`.

[39] Christopher Edwards and Ronald Marks. "Evaluation of biomechanical properties of human skin". In: *Clinics in dermatology* 13.4 (1995), pp. 375–380.

[40] Stanislav Y. Emelianov et al. "Nonlinear dynamics of a gas bubble in an incompressible elastic medium". In: *The Journal of the Acoustical Society of America* 115.2 (2004), pp. 581–588. DOI: `10.1121/1.1621858`.

[41] Actas Urológicas Españolas et al. "Analysis of the safety profile of treatment with a large number of shock waves per session in extracorporeal lithotripsy". In: *Actas Urol Esp* 39 (5 2015), pp. 291–295. URL: `www.elsevier.es/actasuro`.

[42] Andrew P Evan et al. "Shock wave lithotripsy-induced renal injury". In: *American journal of kidney diseases* 17.4 (1991), pp. 445–450.

[43] Caleb H. Farny*, R. Glynn Holt, and Ronald A. Roy. "The Correlation Between Bubble-Enhanced HIFU Heating and Cavitation Power". In: *IEEE Transactions on Biomedical Engineering* 57.1 (2010), pp. 175–184. DOI: `10.1109/TBME.2009.2028133`.

[44]   N. Favrie, S. L. Gavrilyuk, and R. Saurel. "Solid-fluid diffuse interface model in cases of extreme deformations". In: *Journal of Computational Physics* 228 (16 Sept. 2009), pp. 6037–6077. ISSN: 10902716. DOI: 10.1016/j.jcp.2009.05.015.

[45]   K. Firouzi et al. "A first-order k -space model for elastic wave propagation in heterogeneous media". In: *The Journal of the Acoustical Society of America* 132 (3 2012), pp. 1271–1283. ISSN: 0001-4966. DOI: 10.1121/1.4730897.

[46]   N Fischer et al. "Cavitation effects: possible cause of tissue injury during extracorporeal shock wave lithotripsy". In: *Journal of Endourology* 2.2 (1988), pp. 215–220.

[47]   Jean-Pierre Franc. "The Rayleigh-Plesset equation: a simple and powerful tool to understand various aspects of cavitation". In: *Fluid dynamics of cavitation and cavitating turbopumps*. Springer, 2007, pp. 1–41.

[48]   J. B. Freund, R. K. Shukla, and A. P. Evan. "Shock-induced bubble jetting into a viscous fluid with application to tissue injury in shock-wave lithotripsy". In: *The Journal of the Acoustical Society of America* 126 (5 Nov. 2009), pp. 2746–2756. ISSN: 0001-4966. DOI: 10.1121/1.3224830.

[49]   Jonathan B. Freund, Tim Colonius, and Andrew P. Evan. "A Cumulative Shear Mechanism for Tissue Damage Initiation in Shock-Wave Lithotripsy". In: *Ultrasound in Medicine and Biology* 33.9 (2007), pp. 1495–1503. ISSN: 03015629. DOI: 10.1016/j.ultrasmedbio.2007.03.001.

[50]   D. Fuster and T. Colonius. "Modelling bubble clusters in compressible liquids". In: *Journal of Fluid Mechanics* 688 (2011), pp. 352–389. ISSN: 00221120. DOI: 10.1017/jfm.2011.380.

[51]   Morteza Ghorbani et al. "Review on Lithotripsy and Cavitation in Urinary Stone Therapy". In: *IEEE Reviews in Biomedical Engineering* 9.c (2016), pp. 264–283. ISSN: 19411189. DOI: 10.1109/RBME.2016.2573381.

[52]   Forrest R Gilmore. "The growth or collapse of a spherical bubble in a viscous compressible liquid". In: (1952).

[53]   Jacques Goeller et al. "Investigation of cavitation as a possible damage mechanism in blast-induced traumatic brain injury". In: *Journal of neurotrauma* 29.10 (2012), pp. 1970–1981.

[54]   Jacques Goeller et al. "Investigation of cavitation as a possible damage mechanism in blast-induced traumatic brain injury". In: *Journal of Neurotrauma* 29 (10 July 2012), pp. 1970–1981. ISSN: 08977151. DOI: 10.1089/neu.2011.2224.

[55] Eric Goncalves da Silva and Philippe Parnaudeau. "Numerical study of pressure loads generated by a shock-induced bubble collapse". In: *Physics of fluids* 33.11 (2021), p. 113318.

[56] Nancy Elizabeth González-Sierra et al. "Bubble dynamics and speed of jets for needle-free injections produced by thermocavitation". In: *Journal of Biomedical Optics* 28 (07 July 2023). ISSN: 15602281. DOI: 10.1117/1.jbo.28.7.075004.

[57] J. F. Haas. "Interaction of Weak Shock Waves With Cylindrical And Spherical Gas Inhomogeneities". In: *Journal of Fluid Mechanics* 181 (1987), pp. 41–76. ISSN: 14697645. DOI: 10.1017/S0022112087002003.

[58] Fuad Hasan et al. "Cavitation Induced Damage in Soft Biomaterials". In: *Multiscale Science and Engineering* 3 (1 Mar. 2021), pp. 67–87. ISSN: 2524-4515. DOI: 10.1007/s42493-021-00060-x.

[59] N. A. Hawker and Y. Ventikos. "Interaction of a strong shockwave with a gas bubble in a liquid medium: A numerical study". In: *Journal of Fluid Mechanics* 701 (June 2012), pp. 59–97. ISSN: 14697645. DOI: 10.1017/jfm.2012.132.

[60] Keisuke Hayasaka, Akihito Kiyama, and Yoshiyuki Tagawa. "Effects of pressure impulse and peak pressure of a shockwave on microjet velocity in a microchannel". In: *Microfluidics and Nanofluidics* 21 (11 Nov. 2017). ISSN: 16134990. DOI: 10.1007/s10404-017-2004-6.

[61] FJ Heymann. "High-speed impact between a liquid drop and a solid surface". In: *Journal of Applied Physics* 40.13 (1969), pp. 5113–5122.

[62] Niklas Hidman et al. "A multiscale methodology for small-scale bubble dynamics in turbulence". In: *International Journal of Multiphase Flow* 150 (2022), p. 103976.

[63] "High-speed photography of surface geometry effects in liquid/solid impact". In: *Journal of Applied Physics* 63 (4 1988), pp. 1015–1021. ISSN: 00218979. DOI: 10.1063/1.340000.

[64] Danny Howard and Bradford Sturtevant. "In vitro study of the mechanical effects of shock-wave lithotripsy". In: *Ultrasound i n Med. & Biol* 23 (7 1997), p. 1107.

[65] Abel Po Hao Huang et al. "Cavitation-induced traumatic cerebral contusion and intracerebral hemorrhage in the rat brain by using an off-the-shelf clinical shockwave device". In: *Scientific Reports* 9 (1 Dec. 2019). ISSN: 20452322. DOI: 10.1038/s41598-019-52117-5.

[66] Teiichiro Ikeda et al. "Cloud cavitation control for lithotripsy using high intensity focused ultrasound". In: *Ultrasound in Medicine and Biology* 32 (9 Sept. 2006), pp. 1383–1397. ISSN: 03015629. DOI: `10.1016/j.ultrasmedbio.2006.05.010`.

[67] J. E. Field J. P. Dear and A. J. Walton. "Gas compression and jet formation in cavities collapsed by a shock wave". In: *Nature* 332 (1998), pp. 505–508. DOI: `10.1038/332505a0`.

[68] Eric Johnsen and Tim Colonius. "Numerical simulations of non-spherical bubble collapse". In: *Journal of Fluid Mechanics* 629 (2009), pp. 231–262. ISSN: 14697645. DOI: `10.1017/S0022112009006351`.

[69] Eric Johnsen and Tim Colonius. "Shock-induced collapse of a gas bubble in shockwave lithotripsy". In: *The Journal of the Acoustical Society of America* 124 (4 Oct. 2008), pp. 2011–2020. ISSN: 0001-4966. DOI: `10.1121/1.2973229`.

[70] J W J Kaiser, S Adami, and N A Adams. *Three-dimensional direct numerical simulation of shock-induced bubble collapse near gelatin.*

[71] Tejaswi R Kale and Munira Momin. "Needle free injection technology-An overview". In: *Innovations in pharmacy* 5.1 (2014).

[72] A. Karimi and J. L. Martin. "Cavitation erosion of materials". In: *International Metals Reviews* 31.1 (1986), pp. 1–26. DOI: `10.1179/imtr.1986.31.1.1`.

[73] George Karypis and Vipin Kumar. *MeTis: Unstructured Graph Partitioning and Sparse Matrix Ordering System, Version 4.0.* `http://www.cs.umn.edu/~metis`. University of Minnesota, Minneapolis, MN, 2009.

[74] Joseph B. Keller and Michael Miksis. "Bubble oscillations of large amplitude". In: *The Journal of the Acoustical Society of America* 68 (1980), pp. 628–633.

[75] M A F Kendall. *The delivery of particulate vaccines and drugs to human skin with a practical, hand-held shock tube-based system.* 2002.

[76] Mark Kendall. "Engineering of needle-free physical methods to target epidermal cells for DNA vaccination". In: *Vaccine* 24 (21 May 2006), pp. 4651–4656. ISSN: 0264410X. DOI: `10.1016/j.vaccine.2005.08.066`.

[77] Chunghwan Kim et al. "Mechanically induced cavitation in biological systems". In: *Life* 11 (6 June 2021). ISSN: 20751729. DOI: `10.3390/life11060546`.

[78] CR Kim, MS Fønhus, and B Ganatra. "Self-administration of injectable contraceptives: a systematic review". In: *BJOG: An International Journal of Obstetrics & Gynaecology* 124.2 (2017), pp. 200–208.

[79] Evert Klaseboer et al. "Interaction of lithotripter shockwaves with single inertial cavitation bubbles". In: *Journal of fluid mechanics* 593 (2007), pp. 33–56.

[80] Kazumichi Kobayashi, Tetsuya Kodama, and Hiroyuki Takahira. "Shock wave-bubble interaction near soft and rigid boundaries during lithotripsy: Numerical analysis by the improved ghost fluid method". In: *Physics in Medicine and Biology* 56 (19 2011), pp. 6421–6440. ISSN: 00319155. DOI: 10.1088/0031-9155/56/19/016.

[81] T. Kodama and Y. Tomita. "Cavitation bubble behavior and bubble-shock wave interaction near a gelatin surface as a study of in vivo bubble dynamics". In: *Applied Physics B: Lasers and Optics* 70 (1 Jan. 2000), pp. 139–149. ISSN: 0946-2171. DOI: 10.1007/s003400050022.

[82] Tetsuya Kodama and Kazuyoshi Takayama. "Dynamic behavior of bubbles during extracorporeal shock-wave lithotripsy". In: *Ultrasound in Medicine and Biology* 24 (5 1998), pp. 723–738. ISSN: 03015629. DOI: 10.1016/S0301-5629(98)00022-2.

[83] Tetsuya Kodama and Kazuyoshi Takayama. "Dynamic behavior of bubbles during extracorporeal shock-wave lithotripsy". In: *Ultrasound in medicine & biology* 24.5 (1998), pp. 723–738.

[84] Klazina Kooiman et al. "Ultrasound-Responsive Cavitation Nuclei for Therapy and Drug Delivery". In: *Ultrasound in Medicine and Biology* 46 (6 June 2020), pp. 1296–1325. ISSN: 1879291X. DOI: 10.1016/j.ultrasmedbio.2020.01.002.

[85] Evangelos Koukas, Andreas Papoutsakis, and Manolis Gavaises. "Numerical investigation of shock-induced bubble collapse dynamics and fluid–solid interactions during shock-wave lithotripsy". In: *Ultrasonics Sonochemistry* 95 (2023), p. 106393. ISSN: 1350-4177. DOI: https://doi.org/10.1016/j.ultsonch.2023.106393. URL: https://www.sciencedirect.com/science/article/pii/S1350417723001050.

[86] Phoevos Koukouvinis et al. "Compressible simulations of bubble dynamics with central-upwind schemes". In: *International Journal of Computational Fluid Dynamics* 30 (2 Feb. 2016), pp. 129–140. ISSN: 10290257. DOI: 10.1080/10618562.2016.1166216.

[87] Jan Krizek, Paul Delrot, and Christophe Moser. "Repetitive regime of highly focused liquid microjets for needle-free injection". In: *Scientific Reports* 10.1 (2020), p. 5067.

[88] Nikolaos Kyriazis, Phoevos Koukouvinis, and Manolis Gavaises. *Modelling cavitation during drop impact on solid surfaces*. Oct. 2018. DOI: 10.1016/j.cis.2018.08.004.

[89] Nikolaos Kyriazis, Phoevos Koukouvinis, and Manolis Gavaises. "Numerical investigation of bubble dynamics using tabulated data". In: *International Journal of Multiphase Flow* 93 (2017), pp. 158–177. ISSN: 03019322. DOI: 10.1016/j.ijmultiphaseflow.2017.04.004.

[90] E. Lauer et al. "Numerical modelling and investigation of symmetric and asymmetric cavitation bubble dynamics". In: *Computers and Fluids* 69 (Oct. 2012), pp. 1–19. ISSN: 00457930. DOI: 10.1016/j.compfluid.2012.07.020.

[91] Werner Lauterborn and Claus-Dieter Ohl. "Cavitation bubble dynamics". In: *Ultrasonics sonochemistry* 4.2 (1997), pp. 65–75.

[92] Olivier Le Métayer, J Massoni, and R Saurel. "Dynamic relaxation processes in compressible multiphase flows. Application to evaporation phenomena". In: *Esaim: Proceedings*. Vol. 40. EDP Sciences. 2013, pp. 103–123.

[93] Carmen Ledesma-Feliciano et al. "Improved DNA vaccine delivery with needle-free injection systems". In: *Vaccines* 11.2 (2023), p. 280.

[94] TG Leighton, BT Cox, and AD Phelps. "The Rayleigh-like collapse of a conical bubble". In: *The Journal of the Acoustical Society of America* 107.1 (2000), pp. 130–142.

[95] Ine Lentacker et al. "Understanding ultrasound induced sonoporation: definitions and underlying mechanisms". In: *Advanced drug delivery reviews* 72 (2014), pp. 49–64.

[96] Mucong Li et al. "Simultaneous photoacoustic imaging and cavitation mapping in shockwave lithotripsy". In: *IEEE transactions on medical imaging* 39.2 (2019), pp. 468–477.

[97] Shuaiqi Li et al. "Research progress and clinical evaluation of histotripsy: a narrative review". In: *Annals of Translational Medicine* 11.6 (2023).

[98] Emma Linders. "YpsoMate Refill: Concept design of a reusable self-injection device for the circular economy." In: (2023).

[99] Y. Liu and M. A.F. Kendall. "Numerical simulation of heat transfer from a transonic jet impinging on skin for needle-free powdered drug and vaccine delivery". In: *Proceedings of the Institution of Mechanical Engineers, Part C: Journal of Mechanical Engineering Science* 218 (11 2004), pp. 1373–1384. ISSN: 09544062. DOI: 10.1177/095440620421801108.

[100] Yanyang Liu and Jing Luo. "Experimental study on damage mechanism of blood vessel by cavitation bubbles". In: *Ultrasonics Sonochemistry* 99 (2023), p. 106562. ISSN: 1350-4177. DOI: https://doi.org/10.1016/j.ultsonch.2023.106562. URL: https://www.sciencedirect.com/science/article/pii/S1350417723002742.

[101] Achim M Loske et al. *Tandem shock wave cavitation enhancement for extracorporeal lithotripsy INSTITUTE OF PHYSICS PUBLISHING PHYSICS IN MEDICINE Tandem shock wave cavitation enhancement for extracorporeal lithotripsy.* 2002. URL: http://iopscience.iop.org/0031-9155/47/22/303.

[102] Ashley S Love and Robert J Love. "Considering needle phobia among adult patients during mass COVID-19 vaccinations". In: *Journal of primary care & community health* 12 (2021), p. 21501327211007393.

[103] Kazuki Maeda and Tim Colonius. "Bubble cloud dynamics in an ultrasound field". In: *Journal of Fluid Mechanics* 862 (2019), pp. 1105–1134. ISSN: 14697645. DOI: 10.1017/jfm.2018.968. arXiv: 1805.00129.

[104] Kazuki Maeda and Tim Colonius. "Simulation, experiments, and modeling of cloud cavitation". PhD thesis. 2018. DOI: 10.1017/jfm.2018.968. arXiv: 1805.00129.

[105] Ezekiel Maloney and Joo Hwang. "Emerging HIFU applications in cancer therapy". In: *International Journal of Hyperthermia* 31 (Nov. 2014), pp. 1–8. DOI: 10.3109/02656736.2014.969789.

[106] Lauren Mancia et al. "Single – bubble dynamics in histotripsy and high – amplitude ultrasound : Modeling and validation Physics in Medicine & Biology Single – bubble dynamics in histotripsy and high – amplitude ultrasound : Modeling and validation". In: (2020).

[107] "Material Response III: Elastic Solids". In: *Fundamentals of Shock Wave Propagation in Solids.* Berlin, Heidelberg: Springer Berlin Heidelberg, 2008, pp. 121–134.

[108] Ziskin MC et al. "Contrast agents for diagnostic ultrasound". In: *Invest Radiol* 5.6 (1972), pp. 500–505.

[109] Nicole L. Miller and James E. Lingeman. "Management of kidney stones". In: *British Medical Journal* 334 (7591 Mar. 2007), pp. 468–472. ISSN: 09598146. DOI: 10.1136/bmj.39113.480185.80.

[110] Samir Mitragotri. "Current status and future prospects of needle-free liquid jet injectors". In: *Nature reviews Drug discovery* 5.7 (2006), pp. 543–548.

[111] Yuta Miyazaki et al. "Dynamic mechanical interaction between injection liquid and human tissue simulant induced by needle-free injection of a highly focused microjet". In: *Scientific Reports* 11 (1 Dec. 2021). ISSN: 20452322. DOI: 10.1038/s41598-021-94018-6.

[112] Abdul Mohizin and Jung Kyung Kim. "Effect of geometrical parameters on the fluid dynamics of air-powered needle-free jet injectors". In: *Computers in Biology and Medicine* 118 (Mar. 2020). ISSN: 18790534. DOI: 10.1016/j.compbiomed.2020.103642.

[113] Abdul Mohizin, Donghee Lee, and Jung Kyung Kim. "Impact of the mechanical properties of penetrated media on the injection characteristics of needle-free jet injection". In: *Experimental Thermal and Fluid Science* 126 (Aug. 2021). ISSN: 08941777. DOI: 10.1016/j.expthermflusci.2021.110396.

[114] Abdul Mohizin et al. "Computational fluid dynamics of impinging microjet for a needle-free skin scar treatment system". In: *Computers in Biology and Medicine* 101 (Oct. 2018), pp. 61–69. ISSN: 18790534. DOI: 10.1016/j.compbiomed.2018.08.005.

[115] Y Tomita A N and D A Shima. "Mechanisms of impulsive pressure generation and damage pit formation by bubble collapse". In: *J. Fluid Mech* 169 (1986), pp. 535–564.

[116] A Nakagawa et al. "Primary blast-induced traumatic brain injury: lessons from lithotripsy". In: *Shock Waves* 27 (2017), pp. 863–878.

[117] S. Ndanou, N. Favrie, and S. Gavrilyuk. "Multi-solid and multi-fluid diffuse interface model: Applications to dynamic fracture and fragmentation". In: *Journal of Computational Physics* 295 (Aug. 2015), pp. 523–555. ISSN: 10902716. DOI: 10.1016/j.jcp.2015.04.024.

[118] Hamid Ebrahimi Orimi, Sivakumar Narayanswamy, and Christos Boutopoulos. "Hybrid analytical/numerical modeling of nanosecond laser-induced micro-jets generated by liquid confining devices". In: *Journal of Fluids and Structures* 98 (Oct. 2020). ISSN: 10958622. DOI: 10.1016/j.jfluidstructs.2020.103079.

[119] Shucheng Pan et al. "Phenomenology of bubble-collapse-driven penetration of biomaterial-surrogate liquid-liquid interfaces". In: *Phys. Rev. Fluids* 3 (11 Nov. 2018), p. 114005. DOI: 10.1103/PhysRevFluids.3.114005. URL: https://link.aps.org/doi/10.1103/PhysRevFluids.3.114005.

[120] Andreas Papoutsakis, Phoevos Koukouvinis, and Manolis Gavaises. "Solution of cavitating compressible flows using Discontinuous Galerkin discretisation". In: *Journal of Computational Physics* 410 (June 2020). ISSN: 10902716. DOI: 10.1016/j.jcp.2020.109377.

[121] Andreas Papoutsakis et al. "An efficient Adaptive Mesh Refinement (AMR) algorithm for the Discontinuous Galerkin method: Applications for the computation of compressible two-phase flows". In: *Journal of Computational Physics* 363 (June 2018), pp. 399–427. ISSN: 10902716. DOI: 10.1016/j.jcp.2018.02.048.

[122] Marica Pelanti and Keh Ming Shyue. "A mixture-energy-consistent six-equation two-phase numerical model for fluids with interfaces, cavitation and evaporation waves". In: *Journal of Computational Physics* 259 (2014), pp. 331–357. ISSN: 10902716. DOI: 10.1016/j.jcp.2013.12.003. URL: http://dx.doi.org/10.1016/j.jcp.2013.12.003.

[123] Ivo R. Peters et al. "Highly focused supersonic microjets: Numerical simulations". In: *Journal of Fluid Mechanics* 719 (2013), pp. 587–605. ISSN: 14697645. DOI: 10.1017/jfm.2013.26.

[124] B Petit et al. "Sonothrombolysis: the contribution of stable and inertial cavitation to clot lysis". In: *Ultrasound in medicine & biology* 41.5 (2015), pp. 1402–1410.

[125] Thanh-Hoang Phan et al. "Influence of phase-change on the collapse and rebound stages of a single spark-generated cavitation bubble". In: *International Journal of Heat and Mass Transfer* 184 (2022), p. 122270. ISSN: 0017-9310. DOI: https://doi.org/10.1016/j.ijheatmasstransfer.2021.122270. URL: https://www.sciencedirect.com/science/article/pii/S0017931021013697.

[126] A Philipp et al. "Interaction of lithotripter-generated shock waves with air bubbles". In: *The Journal of the Acoustical Society of America* 93.5 (1993), pp. 2496–2509.

[127] A Philipp et al. "Interaction of lithotripter-generated shock waves with air bubbles". In: *The Journal of the Acoustical Society of America* 93.5 (1993), pp. 2496–2509.

[128] Yuri Pishchalnikov et al. "Acoustic Shielding by Cavitation Bubbles in Shock Wave Lithotripsy (SWL)". In: *AIP Conference Proceedings* 838 (May 2006). DOI: 10.1063/1.2210369.

[129] Yuriy A Pishchalnikov et al. "Cavitation bubble cluster activity in the breakage of kidney stones by lithotripter shockwaves". In: *Journal of endourology* 17.7 (2003), pp. 435–446.

[130] Milton S Plesset. "The dynamics of cavitation bubbles". In: (1949).

[131] Milton S Plesset and Richard B Chapman. "Collapse of an initially spherical vapour cavity in the neighbourhood of a solid boundary". In: *J. Fluid Mech* 47 (2 1971), pp. 283–290.

[132] MS Plesset. "On the stability of fluid flows with spherical symmetry". In: *Journal of Applied Physics* 25.1 (1954), pp. 96–98.

[133] Laura Poissonnier et al. "Control of Prostate Cancer by Transrectal HIFU in 227 Patients". In: *European Urology* 51.2 (2007), pp. 381–387. ISSN: 0302-2838. DOI: https://doi.org/10.1016/j.eururo.2006.04.012. URL: https://www.sciencedirect.com/science/article/pii/S0302283806005173.

[134] Andrea Prosperetti. "The thermal behaviour of oscillating gas bubbles". In: *Journal of Fluid Mechanics* 222 (1991), pp. 587–616. DOI: 10.1017/S0022112091001234.

[135] Jin yuan Qian et al. *A comprehensive review of cavitation in valves: mechanical heart valves and control valves*. June 2019. DOI: 10.1007/s42242-019-00040-z.

[136] Jin-yuan Qian et al. "A comprehensive review of cavitation in valves: mechanical heart valves and control valves". In: *Bio-Design and Manufacturing* 2 (2019), pp. 119–136.

[137] Carla Maria Irene Quarato et al. "A Review on Biological Effects of Ultrasounds: Key Messages for Clinicians". In: *Diagnostics* 13.5 (2023), p. 855.

[138] Yatish S. Rane and Jeremy O. Marston. "Computational study of fluid flow in tapered orifices for needle-free injectors". In: *Journal of Controlled Release* 319 (Mar. 2020), pp. 382–396. ISSN: 18734995. DOI: 10.1016/j.jconrel.2020.01.013.

[139] U. Rasthofer et al. "Computational study of the collapse of a cloud with 12 500 gas bubbles in a liquid". In: *Physical Review Fluids* 4.6 (2019). ISSN: 2469990X. DOI: 10.1103/PhysRevFluids.4.063602. arXiv: 1804.11079.

[140] U. Rasthofer et al. "Large Scale Simulation of Cloud Cavitation Collapse". In: *Procedia Computer Science* 108 (2017), pp. 1763–1772. ISSN: 18770509. DOI: 10.1016/j.procs.2017.05.158. URL: http://dx.doi.org/10.1016/j.procs.2017.05.158.

[141] Ansh Dev Ravi et al. "Needle free injection technology: A complete insight". In: *International journal of pharmaceutical investigation* 5.4 (2015), p. 192.

[142] Lord Rayleigh, O.M., and F.R.S. "On the pressure developed in a liquid during the collapse of a spherical cavity". In: *The London, Edinburgh, and Dublin Philosophical Magazine and Journal of Science* 34.200 (1917), pp. 94–98.

[143] Diego Rossinelli et al. "11 PFLOP/s simulations of cloud cavitation collapse". In: *SC '13: Proceedings of the International Conference on High Performance Computing, Networking, Storage and Analysis*. 2013, pp. 1–13. DOI: 10.1145/2503210.2504565.

[144] Hemant J. Sagar and Ould el Moctar. "Dynamics of a cavitation bubble near a solid surface and the induced damage". In: *Journal of Fluids and Structures* 92 (2020), p. 102799. ISSN: 0889-9746. DOI: https://doi.org/10.1016/j.jfluidstructs.2019.102799. URL: https://www.sciencedirect.com/science/article/pii/S0889974619304724.

[145]   GN Sankin et al. "Shock wave interaction with laser-generated single bubbles". In: *Physical review letters* 95.3 (2005), p. 034501.

[146]   Oleg A. Sapozhnikov et al. "A mechanistic analysis of stone fracture in lithotripsy". In: *The Journal of the Acoustical Society of America* 121 (2 Feb. 2007), pp. 1190–1202. ISSN: 0001-4966. DOI: 10.1121/1.2404894.

[147]   Oleg A. Sapozhnikov et al. "Effect of overpressure and pulse repetition frequency on cavitation in shock wave lithotripsy". In: *The Journal of the Acoustical Society of America* 112 (3 Sept. 2002), pp. 1183–1195. ISSN: 0001-4966. DOI: 10.1121/1.1500754.

[148]   Richard Saurel, Fabien Petitpas, and Ray A. Berry. "Simple and efficient relaxation methods for interfaces separating compressible fluids, cavitating flows and shocks in multiphase mixtures". In: *Journal of Computational Physics* 228 (5 Mar. 2009), pp. 1678–1712. ISSN: 10902716. DOI: 10.1016/j.jcp.2008.11.002.

[149]   Kevin Schmidmayer, Spencer H. Bryngelson, and Tim Colonius. "An assessment of multicomponent flow models and interface capturing schemes for spherical bubble dynamics". In: *Journal of Computational Physics* 402 (Feb. 2020). ISSN: 10902716. DOI: 10.1016/j.jcp.2019.109080.

[150]   Jelle J. Schoppink et al. "Cavitation-induced microjets tuned by channels with alternating wettability patterns". In: (Jan. 2023). DOI: 10.1063/5.0143223. URL: http://arxiv.org/abs/2301.10084%20http://dx.doi.org/10.1063/5.0143223.

[151]   Joy Schramm-Baxter and Samir Mitragotri. "Needle-free jet injections: dependence of jet penetration and dispersion in the skin on jet power". In: *Journal of Controlled Release* 97.3 (2004), pp. 527–535.

[152]   Jung Hee Seo, Sanjiva K. Lele, and Gretar Tryggvason. "Investigation and modeling of bubble-bubble interaction effect in homogeneous bubbly flows". In: *Physics of Fluids* 22.6 (2010), p. 063302. DOI: 10.1063/1.3432503. eprint: https://doi.org/10.1063/1.3432503. URL: https://doi.org/10.1063/1.3432503.

[153]   Ahmad Shanei and Ameneh Sazgarnia. "An overview of therapeutic applications of ultrasound based on synergetic effects with gold nanoparticles and laser excitation". In: *Iranian Journal of Basic Medical Sciences* 22 (8 Aug. 2019), pp. 848–855. ISSN: 20083874. DOI: 10.22038/ijbms.2019.29584.7142.

[154]   Oliver A. Shergold, Norman A. Fleck, and Toby S. King. "The penetration of a soft solid by a liquid jet, with application to the administration of a needle-free injection". In: *Journal of Biomechanics* 39 (14 2006), pp. 2593–2602. ISSN: 00219290. DOI: 10.1016/j.jbiomech.2005.08.028.

[155] "Shock-Wave-Induced Jetting of Micron-Size Bubbles". In: *Physical Review Letters* 90 (21 2003), p. 4. ISSN: 10797114. DOI: 10.1103/PhysRevLett.90.214502.

[156] Jeanne C Stachowiak et al. "Dynamic control of needle-free jet injection". In: *Journal of Controlled Release* 135.2 (2009), pp. 104–112.

[157] EP Stride and CC Coussios. "Cavitation and contrast: the use of bubbles in ultrasound imaging and therapy". In: *Proceedings of the Institution of Mechanical Engineers, Part H: Journal of Engineering in Medicine* 224.2 (2010), pp. 171–191.

[158] Yoshiyuki Tagawa et al. "Highly focused supersonic microjets". In: *Physical Review X* 2 (3 2012). ISSN: 21603308. DOI: 10.1103/PhysRevX.2.031002.

[159] Ashagrachew Tewabe et al. "Targeted drug delivery—from magic bullet to nanomedicine: principles, challenges, and future perspectives". In: *Journal of Multidisciplinary Healthcare* (2021), pp. 1711–1724.

[160] Eleuterio Toro. "Riemann Solvers and Numerical Methods for Fluid Dynamics: A Practical Introduction". In: Jan. 2009. DOI: 10.1007/b79761.

[161] Eleuterio F Toro. *Riemann solvers and numerical methods for fluid dynamics: a practical introduction.* Springer Science & Business Media, 2013.

[162] Bradley E. Treeby and B. T. Cox. "A computationally efficient elastic wave model for media with power-law absorption". In: *IEEE International Ultrasonics Symposium, IUS* (1 2013), pp. 1037–1040. ISSN: 19485719. DOI: 10.1109/ULTSYM.2013.0266.

[163] Bradley E. Treeby et al. "Modelling elastic wave propagation using the k-Wave MATLAB Toolbox". In: *IEEE International Ultrasonics Symposium, IUS* (Oct. 2014), pp. 146–149. ISSN: 19485727. DOI: 10.1109/ULTSYM.2014.0037.

[164] Theresa Trummler, Steffen J. Schmidt, and Nikolaus A. Adams. "Effect of stand-off distance and spatial resolution on the pressure impact of near-wall vapor bubble collapses". In: *International Journal of Multiphase Flow* 141 (Aug. 2021). ISSN: 03019322. DOI: 10.1016/j.ijmultiphaseflow.2021.103618.

[165] G. Tryggvason et al. "A Front-Tracking Method for the Computations of Multiphase Flow". In: *Journal of Computational Physics* 169 (2 May 2001), pp. 708–759. ISSN: 00219991. DOI: 10.1006/jcph.2001.6726.

[166] C. K. Turangan et al. "Numerical studies of cavitation erosion on an elastic-plastic material caused by shock-induced bubble collapse". In: *Proceedings of the Royal Society A: Mathematical, Physical and Engineering Sciences* 473 (2205 2017). ISSN: 14712946. DOI: 10.1098/rspa.2017.0315.

[167]   Salih Ozen Unverdi and Grétar Tryggvason. "A front-tracking method for viscous, incompressible, multi-fluid flows". In: *Journal of computational physics* 100.1 (1992), pp. 25–37.

[168]   Diana L. van der Ven et al. "Microfluidic jet impact: Spreading, splashing, soft substrate deformation and injection". In: *Journal of Colloid and Interface Science* 636 (2023), pp. 549–558. ISSN: 0021-9797. DOI: https://doi.org/10.1016/j.jcis.2023.01.024. URL: https://www.sciencedirect.com/science/article/pii/S0021979723000309.

[169]   Eli Vlaisavljevich et al. "Effects of tissue stiffness, ultrasound frequency, and pressure on histotripsy-induced cavitation bubble behavior". In: *Physics in Medicine and Biology* 60.6 (2015), pp. 2271–2292. ISSN: 13616560. DOI: 10.1088/0031-9155/60/6/2271.

[170]   Eli Vlaisavljevich et al. "Visualizing the Histotripsy Process: Bubble Cloud–Cancer Cell Interactions in a Tissue-Mimicking Environment". In: *Ultrasound in Medicine & Biology* 42.10 (2016), pp. 2466–2477. ISSN: 0301-5629. DOI: https://doi.org/10.1016/j.ultrasmedbio.2016.05.018. URL: https://www.sciencedirect.com/science/article/pii/S0301562916300990.

[171]   A Vogel, Werner Lauterborn, and R Timm. "Optical and acoustic investigations of the dynamics of laser-produced cavitation bubbles near a solid boundary". In: *Journal of Fluid Mechanics* 206 (1989), pp. 299–338.

[172]   Olga Vriz et al. "Cavitation phenomenon in mechanical prosthetic valves: not only microbubbles". In: *Echocardiography* 37.6 (2020), pp. 876–882.

[173]   C. W. Wang, T. G. Liu, and B. C. Khoo. "A real ghost fluid method for the simulation of multimedium compressible flow". In: *SIAM Journal on Scientific Computing* 28 (1 2006), pp. 278–302. ISSN: 10648275. DOI: 10.1137/030601363.

[174]   Kevin G. Wang. "Multiphase fluid-solid coupled analysis of shock-bubble-stone interaction in shockwave lithotripsy". In: *International Journal for Numerical Methods in Biomedical Engineering* 33 (10 2017). Added to mind map. ISSN: 20407947. DOI: 10.1002/cnm.2855.

[175]   Qianxi Wang. "Multi-oscillations of a bubble in a compressible liquid near a rigid boundary". In: *Journal of Fluid Mechanics* 745 (Apr. 2014), pp. 509–536. ISSN: 14697645. DOI: 10.1017/jfm.2014.105.

[176]   Kerstin Weinberg and Michael Ortiz. "Kidney damage in extracorporeal shock wave lithotripsy: A numerical approach for different shock profiles". In: *Biomechanics and*

Modeling in Mechanobiology 8.4 (2009), pp. 285–299. ISSN: 16177959. DOI: `10.1007/s10237-008-0135-0`.

[177] Lynn R Willis et al. "Relationship between kidney size, renal injury, and renal impairment induced by shock wave lithotripsy". In: *Journal of the American Society of Nephrology* 10.8 (1999), pp. 1753–1762.

[178] Hao Wu et al. "Experimental investigation on the effects of the standoff distance and the initial radius on the dynamics of a single bubble near a rigid wall in an ultrasonic field". In: *Ultrasonics Sonochemistry* 68 (2020), p. 105197. ISSN: 1350-4177. DOI: `https://doi.org/10.1016/j.ultsonch.2020.105197`. URL: `https://www.sciencedirect.com/science/article/pii/S1350417719315482`.

[179] Xufeng Xi and Pei Zhong. "Dynamic photoelastic study of the transient stress field in solids during shock wave lithotripsy". In: *The Journal of the Acoustical Society of America* 109 (3 Mar. 2001), pp. 1226–1239. ISSN: 0001-4966. DOI: `10.1121/1.1349183`.

[180] Gaoming Xiang et al. "Variations of stress field and stone fracture produced at different lateral locations in a shockwave lithotripter field". In: *The Journal of the Acoustical Society of America* 150.2 (2021), pp. 1013–1029.

[181] A Zhang et al. "A unified theory for bubble dynamics". In: *Physics of Fluids* 35.3 (2023).

[182] Ju Zhang. "Effect of stand-off distance on "counterjet" and high impact pressure by a numerical study of laser-induced cavitation bubble near a wall". In: *International Journal of Multiphase Flow* 142 (2021), p. 103706. ISSN: 0301-9322. DOI: `https://doi.org/10.1016/j.ijmultiphaseflow.2021.103706`. URL: `https://www.sciencedirect.com/science/article/pii/S0301932221001543`.

[183] Ying Zhang et al. "Nanosecond shock wave-induced surface acoustic waves and dynamic fracture at fluid-solid boundaries". In: *Physical review research* 1.3 (2019), p. 033068.

[184] Yuning Zhang et al. *Fundamentals of cavitation and bubble dynamics with engineering applications.* 2017.

[185] P Zhong and CJ Chuong. "Propagation of shock waves in elastic solids caused by cavitation microjet impact. I: Theoretical formulation". In: *The Journal of the Acoustical Society of America* 94.1 (1993), pp. 19–28.

[186] Pei Zhong, Yufeng Zhou, and Songlin Zhu. "Dynamics of bubble oscillation in constrained media and mechanisms of vessel rupture in SWL". In: *Ultrasound in medicine & biology* 27.1 (2001), pp. 119–134.

[187] Pei Zhong, Yufeng Zhou, and Songlin Zhu. "Dynamics of bubble oscillation in constrained media and mechanisms of vessel rupture in SWL." In: *Ultrasound in medicine & biology* 27 (2001), pp. 119–134.

[188] Pei Zhong et al. "Shock wave-inertial microbubble interaction: Methodology, physical characterization, and bioeffect study". In: *The Journal of the Acoustical Society of America* 105 (1999), pp. 1997–2009. DOI: 10.1121/1.426733. URL: http://acousticalsociety.org/content/terms..

[189] Yufeng Zhou and Pei Zhong. "Suppression of large intraluminal bubble expansion in shock wave lithotripsy without compromising stone comminution: Refinement of reflector geometry". In: *The Journal of the Acoustical Society of America* 113 (1 Jan. 2003), pp. 586–597. ISSN: 0001-4966. DOI: 10.1121/1.1528174.

[190] Songlin Zhu et al. "The role of stress waves and cavitation in stone comminution in shock wave lithotripsy". In: *Ultrasound in medicine & biology* 28.5 (2002), pp. 661–671.

[191] E. Zilonova, M. Solovchuk, and T. W.H. Sheu. "Bubble dynamics in viscoelastic soft tissue in high-intensity focal ultrasound thermal therapy". In: *Ultrasonics Sonochemistry* 40.35 (2018), pp. 900–911. ISSN: 18732828. DOI: 10.1016/j.ultsonch.2017.08.017. URL: http://dx.doi.org/10.1016/j.ultsonch.2017.08.017.

[192] E. M. Zilonova, M. Solovchuk, and T. W.H. Sheu. "Simulation of cavitation enhanced temperature elevation in a soft tissue during high-intensity focused ultrasound thermal therapy". In: *Ultrasonics Sonochemistry* 53.35 (2019), pp. 11–24. ISSN: 18732828. DOI: 10.1016/j.ultsonch.2018.12.006. URL: https://doi.org/10.1016/j.ultsonch.2018.12.006.